TECHNISCHE
UNIVERSITÄT
WIEN

Vienna | Austria

Diplomarbeit

Realisation of Quantum Transport Measurements with UCNs within the qBounce Project

ausgeführt am

Atominstitut

der Technischen Universität Wien

unter der Anleitung von

Univ. Prof. Dr. Hartmut ABELE und
Dr. Tobias JENKE

durch

Gregor Wautischer

Dianagasse 3/1; 1030 Wien

Wien, den 15. September 2015

Master Thesis

Realisation of Quantum Transport Measurements with UCNs within the qBounce Project

carried out at the

Institute of Atomic and Subatomic Physics
Vienna University of Technology

under guidance of

Univ. Prof. Dr. Hartmut ABELE and
Dr. Tobias JENKE

by

Gregor Wautischer

Dianagasse 3/1; 1030 Vienna

Vienna, September 15, 2015

Abstract

In the course of this master thesis, quantum transport measurements of ultra-cold neutrons (UCNs) traversing an absorbing reflecting mirror system (ARMS) were realised. An ARMS consists of a flat neutron mirror and a second neutron mirror with a mechanically roughened surface (a scatterer). The scatterer is mounted at a distance h above the flat mirror, with its rough surface facing downwards. Within the Earth's gravitational field, UCNs form gravitationally bound states above a flat surface where total reflection occurs. The quantum transport properties of an ARMS are therefore defined by the interaction of these states with the surface disorder and this interaction depends on the characteristics of the surface disorder as well as on the neutron mirrors' material properties.

To probe the quantum transport properties of such a system, the transmission through the system was measured in dependence of its slit height h, using different coating materials with different Fermi potentials.

To prepare a well-defined phase space for the quantum transport measurements, a second ARMS driven in the classical regime with a slit height of around 200 µm was used as vectorial velocity filter. The phase space preparation was theoretically investigated by three-dimensional classical Monte Carlo simulations and experimentally by performing spatially resolved track detector measurements.

The experimental setup was redesigned with respect to a preceding experiment performed in 2011. The new design allowed for a more efficient experimental performance by introducing the ability to change the distance between the bottom and the top mirrors without having to break the vacuum. This decreased the preparation time for every measurement tremendously. Furthermore, within this thesis, a detailed analysis of measurements performed on the rough surfaces of the differently coated scatterers is presented, to enable a better interpretation of the experimental results and to improve future simulations.

Zusammenfassung

Im Rahmen dieser Diplomarbeit wurden quantenphysikalische Transportphänomene ultrakalter Neutronen (UCN) welche ein absorbierendes reflektierendes Spiegelsystem (ARMS) durchqueren, untersucht. Ein ARMS besteht aus einem Neutronenspiegel mit glatter Oberfläche und einem zweiten Neutronenspiegel mit mechanisch aufgerauter Oberfläche (einem Streuer). Der Streuer befindet sich im Abstand h über dem glatten Neutronenspiegel mit seiner rauen Oberfläche nach unten gerichtet. Da UCN im Gravitationsfeld der Erde über einer glatten, total reflektierenden Oberfläche gebundene quantenmechanische Zustände ausbilden, sind die Transporteigenschaften eines ARMS im quantenmechanischen Bereich von der Wechselwirkung dieser Zustände mit der Oberflächenrauheit bestimmt. Die Transporteigenschaften eines solchen Systems wurden untersucht indem die Transmission durch das System in Abhängigkeit seiner Schlitzhöhe h gemessen wurde. Zusätzlich wurden verschieden beschichtete Spiegel und Streuer verwendet. Die unterschiedlichen Beschichtungen stellen für UCN unterschiedliche Fermi-Potentiale dar und verändern daher die Transporteigenschaften des Systems. Um einen gut definierten Phasenraum am Eintritt in das ARMS zu gewährleisten wurde ein weites ARMS als vektorieller Geschwindigkeitsfilter verwendet. Der vektorielle Geschwindigkeitsfilter wurde mit einer Schlitzhöhe von etwa 200 µm und daher im klassischen Bereich eingestellt. Die Phasenraumpräparation wurde theoretisch mittels dreidimensionaler, klassischer Monte-Carlo-Simulationen und experimentell durch ortsauflösende Spurdetektormessungen überprüft. Das Design des Experimentsetups wurde, im Vergleich zu vorhergehenden Messungen durchgeführt 2011, überarbeitet. Im Detail wurde die Möglichkeit die Schlitzhöhe ohne Öffnen der Vakuumkammer einzustellen eingeführt. Dies verkürzte die Vorbereitungszeit der einzelnen Messungen enorm und erlaubte daher die Durchführung einer größeren Anzahl an Messungen im selben Zeitraum.

Des Weiteren sind in dieser Arbeit Auswertungen von Messergebnissen der Oberflächenrauheiten der verwendeten Streuer präsentiert. Sie sollen zur Genauigkeit zukünftiger Simulationen beitragen und in die Auswertung und Interpretation der Quantentransportmessungen einfließen.

Contents

1 Introduction

The ongoing miniaturization of electronic devices and circuits has reached the nano scale. Electronic transport phenomena in nanowires and nanotubes have therefore received growing attention. One particular case are surface disordered wires and waveguides. Transport through these systems shows interesting behavior, especially when different propagating modes are allowed to traverse the system simultaneously. For the different channels, transmission can depend on different length scales characteristic for each mode. This can lead to the presence of modes experiencing transport without any scattering (ballistic transport), modes experiencing a series of random scattering events (diffusive transport) and modes where quantum mechanical interference becomes relevant (localized transport), at the same time. The simultaneous presence of different transport regimes results in an inadequate description of such systems by conventional techniques and is a current topic of research [Dop+14].

A surface disordered waveguide is used in ultra-cold neutron (UCN) physics by the qBounce collaboration[1]. It consists of a flat neutron mirror with a second neutron mirror, having a mechanically roughened surface facing downwards (a scatterer), at height h above the first one. Within this thesis, this system is called absorbing reflecting mirror system (ARMS). The usage of an ARMS in UCN physics goes back to a proposal by Luschikov and Frank [LF78], who proposed a system to seperate neutrons in the first energy eigenstate above a flat surface. Luschikov and Frank considered a beam of UCNs transversing a flat surface. UCNs are defined by their property of total reflection from a surface under any angle of incident [GP79]. Total reflexion occurs if the neutron's energy E is smaller than the Fermi potential V of the material. In the Earth's gravitational field UCNs with $E < V$, therefore form bound quantum states above a flat surface. In Luschikov and Frank's proposal, a neutron absorber is mounted at height h above the surface creating the ARMS. While propagating through the system, neutrons in different gravitational states (modes) have different interaction probabilities with the absorber and therefore different removal probabilities, due to their different spatial extension (see figure 1.1).

In 2002, the system proposed by Luschikov and Frank, for the first time, was experimentally realised by Nesvizhevsky, Abele et al. [Nes+02]. Nesvizhevsky et al. realised the ARMS using a Ti-Zr-Gd coated scatterer above a flat neutron mirror. The coating was thought to be responsible for removing the higher gravitational states through absorption due to its high absorption cross section. Nesvizhevsky et al. performed transmission measurements in dependence of the ARMS's slit height h. The measurements showed a count rate indistinguishable from the detector background for small slit heights and a sharp increase as soon as the slit reached a height of around 15 μm. This result clearly deviated from the classical expectation $T(h) \sim h^{3/2}$
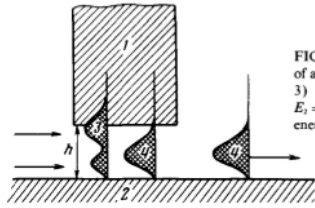

FIG. 2. "Flow" of UCN over a horizontal surface in the case of a gravitational potential. 1) absorber, 2) reflecting surface, 3) density of UCN with vetical-motion energy $E_2 = 2.45 \times 10^{-12}$ eV. 4) Density of UCN with vertical-motion energy $E_1 = 1.4 \times 10^{-12}$. Height of slit $h \approx 20 \ \mu m$.

Figure 1.1: Original figure and caption of the first proposed mirror-absorber system by Luschikov and Frank; source: [LF78], p. 560, fig. 2.

(see subsection 2.3) and proved the existence of quantum mechanically bound states of UCNs within the Earth's gravitational field. In [Nes+05] Nesvizhevsky et al. repeated the experiment using an uncoated scatterer. It was shown that the coating did not increase the system's state selection efficiency and the filtering process inside the ARMS is, therefore, thought to be caused by the interaction of the traversing neutrons with the rough surface, and hence, scattering (see also [Wes+07]). Furthermore, in 2005 Nesvizhevsky et al. were able to verify the existence of a second stepwise increase intransmission, corresponding to the second gravitational state. The state dependent transmission probability of an ARMS lead to its usage today by the qBounce collaboration as a state selector [Jen+11]. However, the detailed characteristics of the selection process are still unknown. It is thought that the overlap of the wave function with the surface disorder plays an important role [Nes+00; Nes+03; Nes+05]. A qualitative model based on the overlap has been developed in [Wes+07] and is also discussed in subsection 2.3. The removal process is furthermore thought to depend on the detailed characteristics of the surface disorder as well as the surface material's properties (Fermi potential).

This thesis was realised in cooperation with the research group for "nonlinear dynamics and complex scattering" of the Institute for Theoretical Physic at the Vienna University of Technology[2]. The group of Prof. Stefan Rotter investigated transport through surface disordered waveguides in the past and further developed techniques to adequately describe it [Dop+14]. Of special importance for this thesis is the work of Feist et al. regarding the transport of electrons through nanowires with one-sided surface disorder in the presence of a perpendicular magnetic field [Fei+06][Fei+09]. This system is similar to the ARMS used in UCN physics, where now electrons forming bound quantum states in the
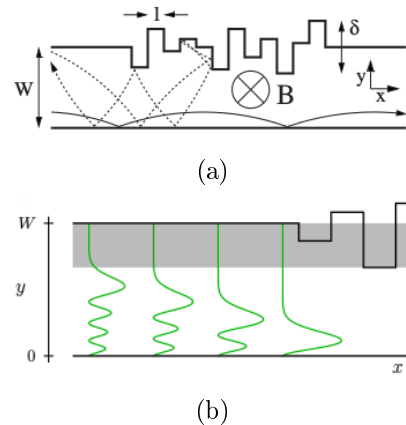

Figure 1.2: (a) Nanowire with one-sided surface disorder as investigated by Feist et al. The solid line represents regular motion and the dashed line represents irregular (scattering) motion; source: [Fei+09], p. 1, fig. 1.
(b) Formation of bound quantum states of electrons in the perpendicular magnetic field; source: [Fei+09], p. 3, fig. 3.

magnetic field similar to the states formed by UCNs within the Earth's gravitational field, traverse the waveguide. Classically, the perpendicular magnetic field forces electrons to traverse the wire on circular arcs. Electrons with a large enough velocity will have a radius large enough to touch the surface disorder and scatter off it (see figure 1.2a). This interaction with the surface roughness, according to Feist et al., leads to the coexistence of regular and irregular (scattering) motion inside the system. The underlying phase space is therefore mixed regular chaotic with the regular and chaotic region classically completely separated. Quantum mechanically, the electrons form bound states in the magnetic field (see figure 1.2b). The interaction with the surface roughness is now governed by the wave function's properties, leading to a finite interaction probability for every state. The regular and chaotic part of the phase space therefore become connected by dynamic tunneling. This in turn leads to a mode dependent decrease in transmission with wire length (see figure 1.3) and therefore a stepwise decrease in overall transmission with increasing wire length. Since changing the system's length with constant roughness parameters is experimentally impossible, the transmission measurements by Nesvizhevsky et al., as well as the measurements presented here, are performed in dependence of the wave guide's slit height. Changing the slit height changes the interaction potential of the wave functions with the surface roughness mode dependent and therefore a stepwise increase in transmission with increasing slit height is expected, similar to the results obtained by Nesvizhevsky et al. Furthermore, from an experimental point of view, neutrons, carrying no electric charge and only a tiny polarization are better suited to investigate such systems since scattering dynamics and quantum chaos phenomena can be studied in absence of the long-range Coulomb interaction.
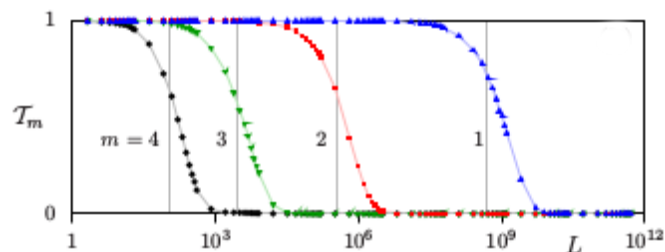

Figure 1.3: Mode (m) dependent transmission T_m for the first 4 modes; source: [Fei+09], p. 4, fig. 4. (see also [Wes02; Wes+07])

In 2011, a first attempt to investigate the removal process in more detail was made. An experimental setup consisting of two ARMSs in serial arrangement was designed. The first ARMS was used to select defined states and the transport measurements were performed in the second ARMS in dependence of its slit height. The transport measurements were successfully realised and the data were passed on to the theory group of S. Rotter.

In this thesis the characteristics of the removal process and therefore the quantum transport properties of a waveguide with one-sided surface disorder were further investigated experimentally. The setup was redesigned with respect to the first experimental realisation in 2011 to avoid limitations discovered then (see subsection 3.1.1), leaving the basic design as described above unchanged. To obtain more information about the initial conditions for the transport

measurements, the initial phase space prepared by the first ARMS (from here on called selector) was studied theoretically by using classical three dimensional Monte Carlo simulations (see subsection 2.2 and [Chi+14]) and experimentally by performing spatially resolved track detector measurements to record the neutrons' distribution at its end (see section 4.2). Transmission measurements in dependence of the slit height were then performed in the second ARMS (the measurement part) in the same way as in 2011, including the use of differently coated mirrors and scatterers to change the surface interaction potential. Furthermore, the scatterers' roughness was investigated in detail using measurement performed with stylus instrument and scanning electron microscopy (SEM) (see section 3.2) to enable a more precise evaluation of the obtained transmission data. The experiment itself was performed at the instrument PF2 [Pf2] at the Institute Laue-Langevin[3] (ILL), where the worlds highest flux of ultra-cold neutrons is available, offering ideal conditions for this experiment.

This thesis is structured as follows: in the next chapter the measurement principle is presented and theoretical background is given. The formation of quantum states in the Earth's gravitational field is reviewed shortly, scattering dynamics inside an ARMS are discussed, results of the Monte Carlo simulations for the scatterer are presented and theoretical expectations for the quantum transport measurements are given. In chapter 3 the experimental setup, its design and important parts are introduced. The investigation of the surface roughness is presented and the evaluation and estimation of systematic effects is described. Finally, in chapter 4, the measurement results are shown. The evaluation of the track detector measurements is presented, as also published in [Chi+14] where further interpretation is given. The transmission measurements are shown as well, but no detailed evaluation is presented since it is not part of this thesis but will be conducted by the theory group of S. Rotter. The thesis ends with a conclusion and prospect for future enhancements (chapter 5).

---

[3]Institut Laue-Langevin, 71 avenue des Martyrs, 38000 Grenoble, France

2 Measurement Principle and Theoretical Background

In this chapter, the measurement principle of the realised experiment is presented. First the experimental setup is introduced schematically and theoretical background, as well as theoretical expectations are given in the following.

A schematic view of the experimental setup used is shown in figure 2.1. The setup consists of three main parts:

- The Collimator;

- The Selector;

- The Measurement Part;
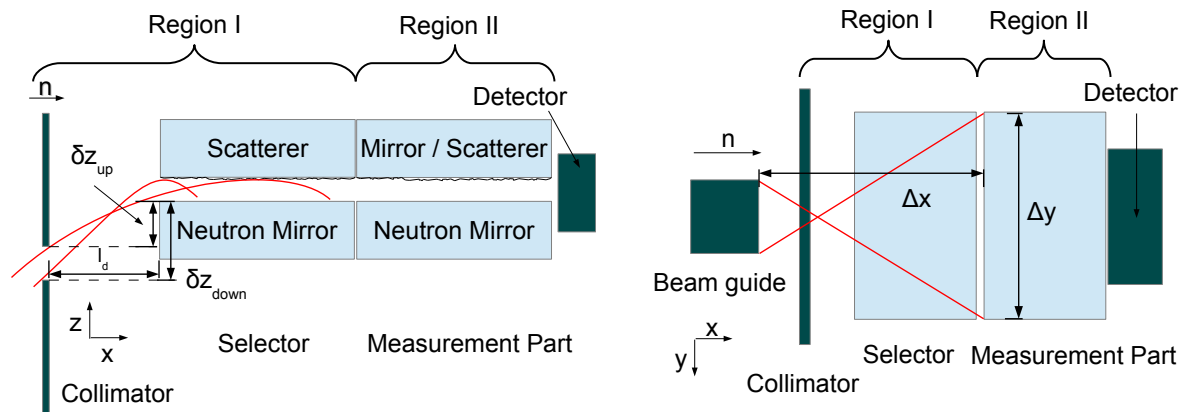
(a) Schematic side view of the experimental setup; not drawn to scale.

(b) Schematic top view of the experimental setup; trajectories for neutrons with the maximal possible velocity in y direction are depicted in red; not drawn to scale.

Figure 2.1: Schematic view of the experimental setup. Neutrons enter from the left.

The three parts constitute the two regions of the experimental setup. Region I consists of the collimator and the selector and is also called vectorial velocity filter. Here, the initial phase space for the transport measurements is prepared. In Region II, represented by the measurement part, the actual transport measurements are performed.

In the following, after a short introduction into the formation of quantum states of UCNs within the Earth's gravitational field, each region is discussed in detail.

2.1 Quantum States in the Earth's Gravitational Field

The property of total reflection leads ultra-cold neutrons to form bound quantum states upon a flat surface [Wes+07]. The interaction of UCNs with a flat surface is determined by the height of the potential barrier the material constitutes for the UCNs. Assuming an infinitely high potential barrier, together with the gravitational potential a triangular potential well above the flat surfaces is created:

$$V(z) = \begin{cases} mgz, & z > 0, \\ \infty, & z \leq 0, \end{cases} \tag{2.1}$$

The gravitationally bound quantum states can be obtained by solving the one-dimensional Schrödinger equation for the gravitational potential $V(z)$ from above:

$$\left(-\frac{\hbar^2}{2m}\frac{\partial^2}{\partial z^2} + mgz \right)\psi(z) = E\psi(z) \tag{2.2}$$

where g represents the Earth's gravitational acceleration and m is the neutron's mass. The boundary conditions, for a flat surface - the neutron mirror - at $z = 0$ are:

$$\psi(0) = 0; \quad \psi(\infty) = 0 \tag{2.3}$$

The Schrödinger equation with this triangular potential is solved by the Airy-Ai-Function

$$\psi_n(\xi) = \begin{cases} A_n Ai(\xi - \xi_n), & \xi > 0 \\ 0, & \xi \leq 0 \end{cases} \quad \text{with} \quad \xi = \frac{z}{R} \tag{2.4}$$

where ξ_n is the nth zero of the Airy function $(Ai(-\xi_n) = 0)$ and R is a scaling factor defined as:

$$R = \left(\frac{\hbar^2}{2m^2g} \right)^{1/3} \tag{2.5}$$

The factors A_n ensure normalisation of the wave functions.

The discrete energy spectrum is introduced by the boundary condition $\psi(z = 0) = 0$ and the requirement of derivability of the solution at $\xi = 0$ leading to $Ai(-\xi_n) = 0$ [Kra06]. The energy eigenvalues are then given by:

$$E_n = mgR\xi_n \tag{2.6}$$

The ξ_n can be obtained by numerical computation or are given to leading order in the WKB approximation [Wes+07]:

$$\xi_n = \left(\frac{3}{2}\left(n - \frac{1}{4} \right) \right)^{3/2} \tag{2.7}$$

The energy eigenvalues (E_n) obtained from numerical computation and the corresponding wavelengths (λ_n) can be seen in table 2.1. The wave functions $\psi_n(z)$ of the corresponding eigenstates are shown in figure 2.2.

n	E_n [peV]	λ_n [µm]
1	1.407	24.12
2	2.459	18.24
3	3.321	15.70
4	4.083	14.16

Table 2.1: Energies E_n and corresponding wavelengths λ_n for the first four gravitational states, obtained by numerical computation.
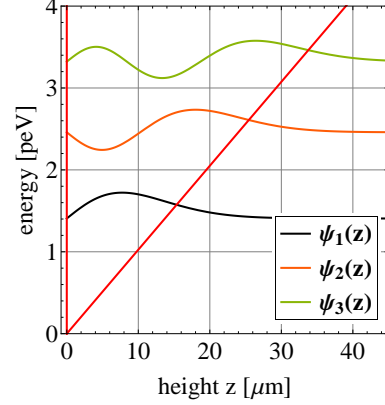

Figure 2.2: First three gravitational states (ψ_n); the red line represents the gravitational potential.

For the presented measurements, a second surface is introduced at height h above the first one. This changes the spectrum as well as the states' spatial distribution, since the second surface constitutes a second boundary condition $\psi(z = h) = 0$. A potential well overlying the triangular gravitational potential is therefore formed:

$$V(z) = \begin{cases} \infty, & z \geq h, \\ mgz, & h > z > 0, \\ \infty, & z \leq 0, \end{cases} \tag{2.8}$$

and the eigenstates are now given by a mixture of AiryAi and AiryBi functions:

$$\psi_{n,confined}(\xi) = A_n Ai(\xi - \epsilon_n(h)) + B_n Bi(\xi - \epsilon_n(h)) \tag{2.9}$$

Here $\epsilon_n(h)$ are the energy eigenvalues depending on the slit height h. In figure 2.3 the difference between the unconfined (free) and the confined eigenstates for a height of $h = 30$ µm is illustrated. The upper surface effectively squeezes the wave functions. The energy eigenvalues for the confined states, obtained by numerical computation, are stated in table 2.2.

2.2 Region I - Phase Space Preparation

The initial phase space for the transport measurements is prepared in region I of the experimental setup. The preparation is achieved by an interplay between the collimator and the selector.

The collimator consists of two neutron absorbing plates creating a slit. Neutrons enter the experimental setup from a beam guide in front of the collimator and can only reach the the selector through the slit created by the collimator's two plates (see figure 2.1a).

7

n	ϵ_n [peV]	λ_n [µm]
1	1.407	24.11
2	2.495	18.11
3	3.656	14.96
4	5.222	12.52

Table 2.2: Energy eigenvalues ϵ_n and corresponding wavelengths λ_n for the first four gravitational states confined by a second upper surface at $h = 30$ µm, obtained by numerical computation.
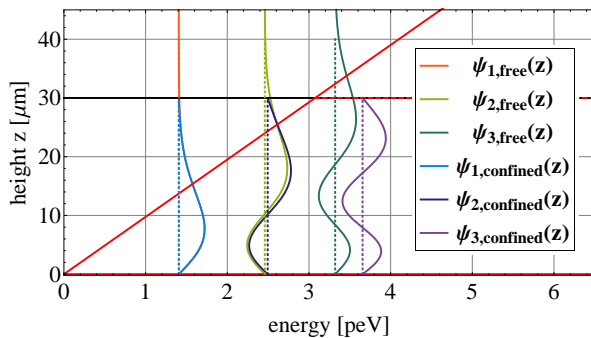
Figure 2.3: First three gravitational states ($\psi_{n,free}$) for the unconfined and the system confined from the top at $h = 30$ µm ($\psi_{n,confined}$); the permanent red line represents the free gravitational potential; the dashed red line depicts the potential well created by the upper surface (indicated by the thick black line).

The selector is located at a distance l_d from the collimator and consists of two neutron mirrors. One flat neutron mirror at the bottom and another neutron mirror with a mechanically roughened surface facing downwards (a scatterer) at height h above it. It therefore is an absorbing reflecting mirror system (ARMS). The two mirrors form a potential well, described by a Fermi potential $V - iW$ characteristic for a given surface material. The real part V of the Fermi potential constitutes the critical energy $E_{cr} = V$ and determines the critical velocity v_{cr}. Neutrons with a kinetic energy normal to the surface ($E_\perp$) larger than the critical energy ($E_\perp > E_{cr}$) can penetrate the surface and leave the system. However, UCNs with $E_\perp < E_{cr}$ can also be removed because of absorption due to the interaction with nuclei of surface atoms. This absorption is included as the imaginary part W of the Fermi potential depending on the absorption scattering cross section σ_l. For a neutron hitting the surface, the imaginary part of the Fermi potential therefore leads to a reflexion probability of $R = 1 - \mu(E_\perp)$, where $\mu(E_\perp)$ is proportional to the loss factor W/V and the neutrons energy perpendicular to the surface [GP79; Chi+14].

The neutron mirrors used for the ARMS in region I in the experiment are made of borosilicate glass. For borosilicate the real part of the Fermi potential (V) is around 100 neV [Wes02]. This, compared to the UCNs' energy, relatively high potential ensures that several thousand gravitational states can be confined inside the selector. The slit height of the selector was chosen ≈ 200 µm. The large slit height in combination with the high number of allowed states leads to a very dense phase space. Since furthermore, the scatterer's roughness is in the micrometer range, much larger than the UCNs' typical de Broglie wavelength $\lambda \lesssim 100$ nm, the scattering dynamics inside the selector can be described classically.

A classical, point-like neutron will travel through the selector on a skipping trajectory with a hopping height depending on its vertical Energy $E_\perp$. On a skipping trajectory with a max-

imum height smaller than the slit height h, a neutron will traverse the selector ballistically without interacting with the rough surface. In contrast, neutrons with a hopping height larger than h will scatter off the rough surface elastically but non-specular. The scattering leads to a momentum transfer between different momentum components and changes the neutrons direction of flight. Such neutrons will therefore be continuing on a chaotic, so-called scattering trajectory, experiencing a much higher number of wall collisions compared to neutrons on skipping trajectories and their motion will, therefore, be diffusive rather than ballistic. Since every collision has a given probability for absorption, the overall probability of a neutron on a scattering trajectory to traverse the filter is highly reduced. Furthermore, the momentum transfer can lead to a situation where the neutron's kinetic energy perpendicular to the surface will be larger than the Fermi potential energy V of the surface and the neutron will leave the system as well. A UCN on a scattering trajectory, therefore has a much higher probability of absorption than a neutron on a skipping trajectory. This establishes the filtering properties of the selector. Assuming total absorption of neutrons on scattering trajectories, only neutrons with $v_z < \sqrt{2gh}$ (i.e. on a skipping trajectory) are allowed to traverse. For neutrons at the collimator this means that they will only traverse the filter if their vertical velocity component (v_{z_0}) is in range of $\sqrt{2g\delta_z} \leq v_{z_0} \leq \sqrt{2g\delta_z + h}$, where δ_z denotes the distance between the selector's lower mirror and the neutron's position at the collimator. Since neutrons at the collimator have to traverse the horizontal distance between the collimator and the selector (l_d) in the same time as they have to travel the vertical distance δ_z, there velocity component in longitudinal (x-) direction is restricted as well (see [Chi+14] for a detailed derivation). For the maximal and minimal longitudinal velocity component (v_x) of neutrons at the end of the filter one obtains:

$$v_{x_{max}} = \frac{gl_d}{\sqrt{2g(\delta_{z_{up}} + h)} - \sqrt{2gh}} \quad \text{and} \quad v_{x_{min}} = \frac{gl_d}{\sqrt{2g(\delta_{z_{down}} + h)} + \sqrt{2gh}}. \tag{2.10}$$

Here, $\delta_{z_{up}}$ and $\delta_{z_{down}}$ are the vertical distances and l_d is the horizontal distance between the upper or lower collimating plate and the selector's lower mirror; g represents the Earth's gravitational acceleration. Furthermore, the third velocity component (v_y) is also restricted by the setup's geometry. In detail, the velocity in y direction has to be small enough, so the neutron is still entering the measurement part of the setup (see figure 2.1b). It holds:

$$v_{y_{max}} = \frac{\Delta y}{\Delta x} v_{x_{max}} \tag{2.11}$$

where Δx denotes the distance between the beam guide and the measurement part in the neutrons direction of flight and Δy denotes the distance of one side of the beam guide to the opposing side of the measurement part. The maximum value for every velocity component of neutrons traversing region I is therefore completely detemined by the setup's geometrical parameters suggesting the usage of the name vectorial velocity filter for region I of the experimental setup.

The assumption of total absorption of neutrons on scattering trajectories does not hold and also a small number of UCNs on scattering trajectories will always traverse the selector. The resulting phase space at the vectorial velocity filter's end will therefore be a mixed regular-

chaotic phase space composed of an regular island representing the skipping trajectories and of an irregular part of chaotic scattering trajectories (the chaotic sea). An illustrative example of the projection of the Poincaré surface of section onto the (v_z, z) plane of the phase space at the end of the vectorial velocity filter with a selector's slit height h is shown in figure 2.4. The shape of the regular island of the phase space (shown in blue) is determined by the restrictions imposed on the velocity components by the filter's geometry. The chaotic sea is represented by the red points. The two parts are, in the classical view, completely separated from each other. To investigate the phase space and evaluate the amount of neutrons on scattering trajectories traversing the filter, classical three dimensional Monte Carlo simulations were performed and are presented in the following.
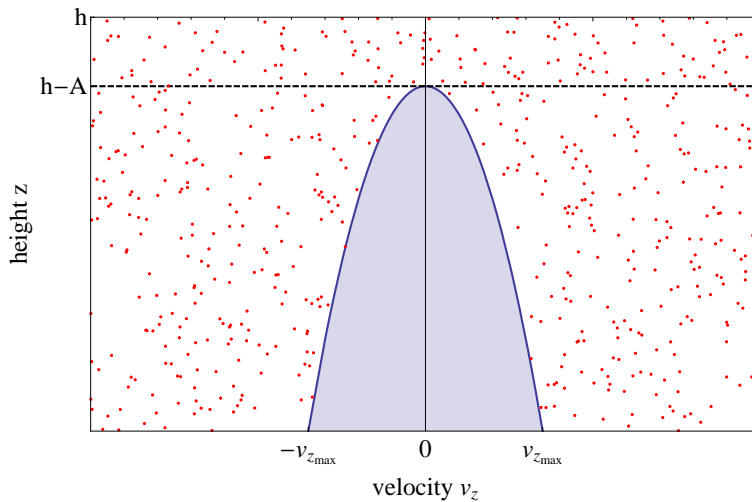

Figure 2.4: Illustrative example of the Poincaré surface of section onto the (v_z, z) plane of the phase space at the end of the selector with a slit height h. The regular island covering the skipping trajectories is shown in blue. The red dots represent the chaotic scattering trajectories. Scattering of neutrons off the rough surface occurs in the area $h - A$ to h.

Theoretical Expectations for the Phase Space Preparation

The initial phase space for the transport measurements, in dependence of the setup's geometrical parameters has been investigated using classical three-dimensional Monte Carlo simulations. In [Chi+14] detailed information about the simulations and their results are available. Here only the filtering characteristics and dependencies published in [Chi+14] are summarised. Additionally, simulations to estimate the influence of the shift of the scatterer versus the lower mirror of the selector, introduced due to reasons regarding the control of the experimental setup (see subsection 3.1.1), are presented.

A schematic illustration of the setup used for the simulations can be seen in figure 2.5. The simulation were performed for a setup with standard geometrical parameters of slit height 250 µm, length and width 10 cm, roughness amplitude $R_a = 3$ µm and a correlation length of 2 µm. The detailed discussion of the distribution of UCNs exiting the beam guide, used as

initial conditions can be found in [Chi+14]. For the forward velocity component, data from previously conducted time-of-flight measurements were used. The system was simulated for a selector consisting of borosilicate glass as used within the experiment, with a critical velocity of $v_{cr} = 4.3$ m/s and a loss factor of V/W $= 0.0015$. To investigate the filtering properties of the selector, the geometrical parameters of the setup were varied and the fraction of skipping trajectories and the overall transmission was investigated. Furthermore, the distribution of neutrons inside the regular island and inside the chaotic sea was examined.

The results as published in [Chi+14] show a decreasing fraction of chaotic scattering trajectories and overall transmission at the end of the selector when increasing the selector's length. The dependence of the slit height shows an increase of chaotic scattering trajectories, as well as transmission, with increasing slit height. Regarding the roughness parameters, the simulations show that a high roughness amplitude and a small correlation length further reduce the number of neutrons on chaotic scattering trajectories. However, a reduction of the chaotic scattering sea also reduces the expected transmission. The distribution of neutrons inside the regular island as well as in the chaotic sea tends to become more uniform with increasing length of the selector, due to the large number of bounces.

Figure 2.5: Illustration of the setup used for the three-dimensional Monte Carlo simulations.

For a filter length of 20 cm both distributions are found to be homogeneous. The actual parameters chosen for the new experimental setup were defined on basis of this simulation results and their experimental feasibility.

The selector's slit height is created by brass spacers between the lower mirror and the scatterer. Their possible influence on the phase space is also discussed in [Chi+14] and has been considered during the design process (see subsection 3.1.1).

Prior to the experiment, simulations for the selector as used in the experiment, with a length of 20 cm and a width of 15 cm were performed. The slit height was set to 250 µm and a roughness amplitude of $R_a = 3$ µm and a correlation length of 2 µm were used. A Poincaré surface of section onto the (v_z, z) plane of the phase space at the end of the filter, obtained from the simulations can be seen in figure 2.6a. For this system, a fraction of around 5% of total transmission is found to lie within the chaotic sea.

Figure 2.7: Illustration of the setup used for the three-dimensional Monte Carlo simulations including the upper mirror's shift.
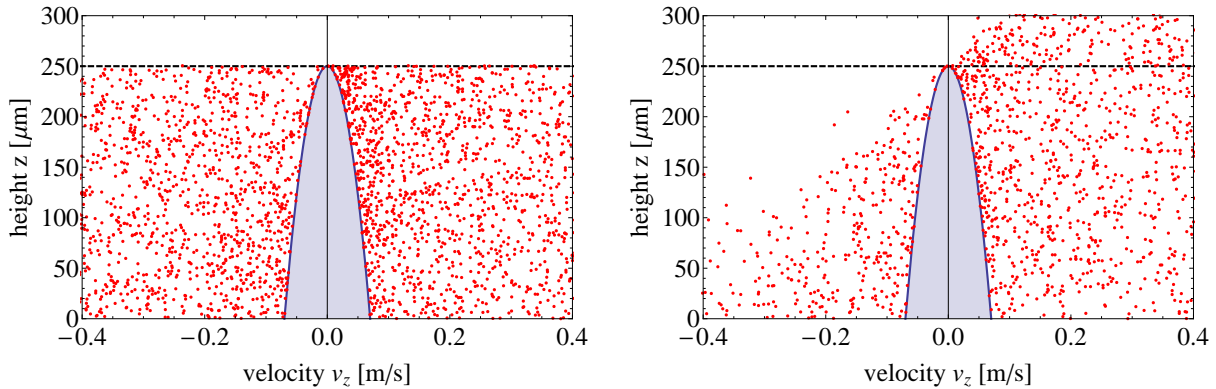
For purposes of experimental conduction, the selector's scatterer was shifted towards the collimator with respect to its lower mirror (see subsection 3.1.1 for a explanation and figure 2.7 for an illustration). To estimate the consequences on the phase space due to this mirror shift further simula-
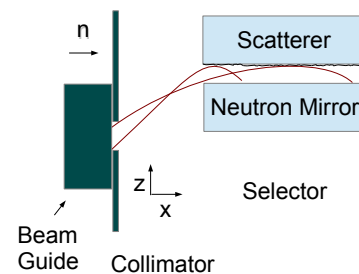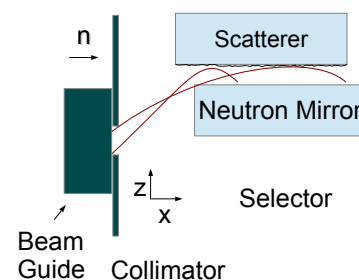
(a) Poincaré surface of section onto the (v_z, z) plane of the phase space at the end of the filter without a shift.

(b) Poincaré surface of section onto the (v_z, z) plane of the phase space at the end of the filter with a shift of 5 mm.

Figure 2.6: Comparison of the phase space at the end of the vectorial velocity filter with and without a shift of the selector's scatterer versus its lower mirror, obtained from three-dimensional Monte Carlo simulations.

tions have been performed. In figure 2.6b the Poincaré surface of section onto the (v_z, z) plane of simulations for the phase space at the end of the shifted filter is shown. First of all, the mirror shift reduces the active filtering length of the selector and the fraction of neutrons on scattering trajectories is therefore slightly increased. Furthermore, the shift introduces a transition from the confined system with two surfaces above each other to the free system. Therefore neutrons on scattering trajectory when leaving the confined system can fly upwards as clearly visible by the scattering trajectories above 250 µm. This effect reduces the probability of UCNs on scattering trajectories to enter the measurement part, leading to even better defined initial conditions for the transport measurements.

2.3 Region II - The Transport Measurements

The actual transport measurements are performed in region II of the experimental setup, represented by the so called measurement part.

The measurement part is a mounting device where two neutron mirrors can be installed above each other, creating a slit in the same way as the selector. In contrast to the selector used for the vectorial velocity filter, the measurement part was designed in such a way, that the distance between the two mirrors can be varied with submicrometer precision during measurements. It therefore allows for performing transmission measurements in dependence of the systems slit height (z_{slit}).

The measurement part was operated in two different configurations:

1. an ARMS, with a rough mirror on top and a flat neutron mirror below

2. a mirror-mirror system (MMS), i.e. an ARMS with two flat mirrors

Operating the measurement part as an ARMS allows us to investigate the neutrons' interaction with the rough surface, including localization effects in the quantum mechanical regime. Since the interaction is material dependent, also differently coated scatterers were used to investigate this material dependence. However, using different scatterers makes it necessary to control their roughness to ensure stability of this parameter (see subsection 3.1.3 for an explanation of the production process). To do so, only scatterers produced in the same way were used to keep this parameter constant during all measurements. The roughness of the scatterers used was investigated in detail and is presented in section 3.2.

Operating the measurement part as a MMS, no filtering due to the interaction with the rough surface occurs and only neutrons with a vertical velocity higher than the critical velocity of the material used are extracted from the system. Therefore, by comparing the transmission through MMS and ARMS the fraction of neutrons being filtered due to interaction with the surface disorder can be extracted.

Theoretical Expectations for the Transport Measurements

Based on the phase space prepared by the vectorial velocity filter, here the theoretical expectations for the quantum transport measurements are presented. The discussion is based on the phase space of a perfectly working filter, in absence of scattering trajectories, but the expected changes due to their presence are mentioned. First the expectations for the classical regime are given. Afterwards the quantum mechanical regime is discussed. The expectations are given for the mirror-mirror as well as for the scatterer-mirror system (ARMS).

Theoretical Expectations for the Classical Regime

In the classical regime, the UCNs can again be viewed as point-like particles traversing the system. For a mirror - mirror system used inside the measurement part, UCNs with a hopping height larger than the slit height and hence $v_{z_{max}} > \sqrt{2gz_{slit}}$, will scatter off the upper mirror without any momentum transfer. Therefore, only neutrons with $v_\perp > v_{cr}$ will be removed, independent of their absolute velocity.

Using a mirror - mirror system is identical to cutting out a part of the Poincaré surface of section onto the (v_z, z) plane of the phase space prepared by the vectorial velocity filter, up to the measurements part's slit height z_{slit}. This is indicated in figure 2.8a. The transmission function $T(z_{slit})$ is proportional to the area cut out from the regular island $A(z_{slit})$, that can be calculated as follows. For a given slit height h of the selector, the allowed absolute velocities at a given height $z \leq h$ ranges from $0 \leq v \leq \sqrt{2g(h-z)}$. This can be expressed as $v_{z_{max}}(z) = \sqrt{2g(h-z)}$. To obtain the area cut out from the regular island this has to be integrated with respect to z up to the slit height of the measurement part z_{slit}, leading to:

$$T(z_{slit}) \propto A(z_{slit}) = \frac{2\sqrt{2g}}{3}\left(h^{3/2} - \left(h - z_{slit}\right)^{3/2}\right) \tag{2.12}$$

When increasing z_{slit} above the filters slit height h no further increase is expected, but the
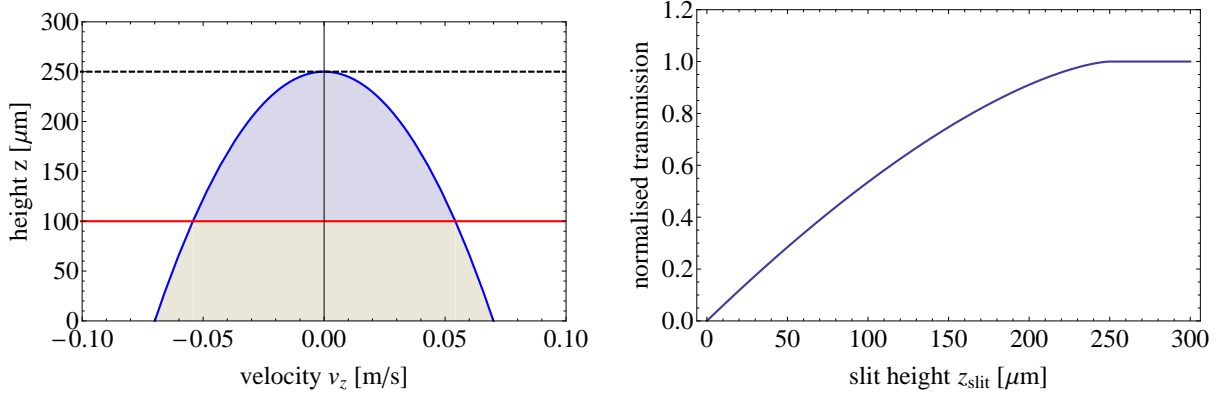
(a) Poincaré surface of section onto the (v_z, z) plane of the phase space at the end of a perfectly working vectorial velocity filter is indicated in blue. The red line shows the position of the measurement part's upper mirror for a slit height of $z_{slit} = 100\,\mu m$. UCNs belonging to the beige area below the red line, are allowed to traverse the measurement part, since no filtering occurs.

(b) Expected transmission at the end of the measurement part in dependence of the slit height z_{slit}.

Figure 2.8: Theoretical expectations for the mirror-mirror system in the classical regime.

transmission saturates since no further UCNs enter the measurement part.

Since no filtering occurs for the mirror-mirror system, the obtained measurements can be used to investigate the initial phase space for the measurements and by comparison with the measurements performed with an ARMS, the fraction of filtered UCNs can be obtained.

Regarding influences of the chaotic sea, the number of neutrons on scattering trajectories entering and traversing the mirror-mirror system are thought to increase linear with increasing slit height due to their homogeneous distribution. Therefore a steeper increase in transmission is expected with respect to the ideal case. Furthermore, for $z_{slit} > h$ a further increase in transmission is expected in contrast to the ideal case. This is, since due to the shift of the filter's scatterer, neutrons on scattering trajectories are able to reach heights larger than the slit height h of the selector at the measurement part's entrance (see figure 2.6b).

For a scatterer - mirror system (ARMS) again, like in the vectorial velocity filter, a filtering process occurs, removing all neutrons with $v_{z_{max}} > \sqrt{2gz_{slit}}$. From the initial phase space, therefore, another regular island is extracted as illustrated in figure 2.9a. The transmission scales with the area of the extracted island, that can be calculated in a similar way as for the mirror - mirror case. For a given slit height z_{slit}, the allowed absolute velocities at a given height $z \leq z_{slit}$ ranges from $0 \leq v \leq \sqrt{2g\left(z_{slit} - z\right)}$. This can again be expressed as $v_{z_{max}}(z) = \sqrt{2g\left(z_{slit} - z\right)}$ and the transmission function is obtained by integrating over all heights $0 \leq z \leq z_{slit}$ leading to:

$$T(z_{slit}) \propto \frac{2\sqrt{2g}}{3} z_{slit}^{3/2}. \tag{2.13}$$
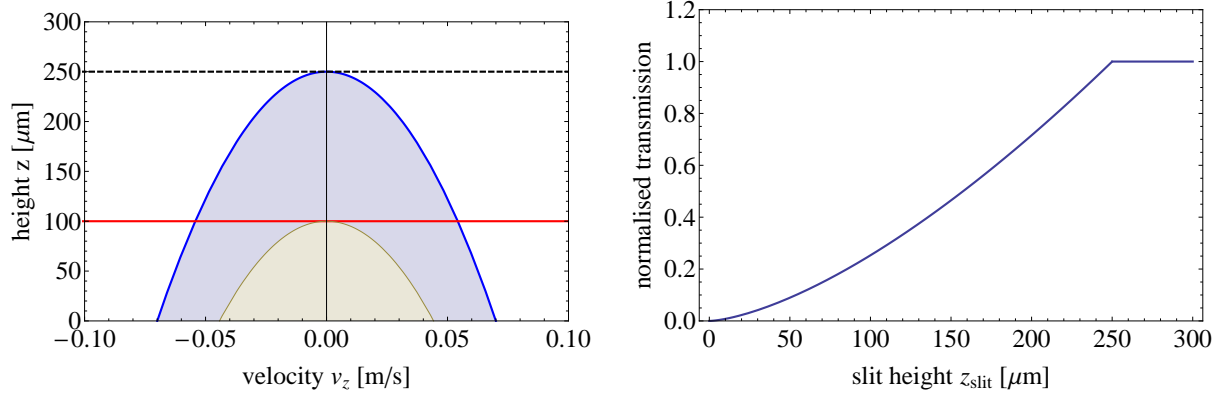
(a) Poincaré surface of section onto the (v_z, z) plane of the phase space at the end of a perfectly working vectorial velocity filter is indicated in blue. The red line shows the position of the measurement part's upper mirror for a slit height of $z_{slit} = 100$ µm. Since due to the scatterer's rough surface neutrons are filtered for their hopping height while traversing the measurement part, only neutrons inside the smaller regular island (indicated in beige) are allowed through.

(b) Expected transmission at the end of the measurement part in dependence of the slit height z_{slit}

Figure 2.9: Theoretical expectations for the scatterer-mirror system in the classical regime.

The transmission is expected to saturate for $z_{slit} > h$ as well.

Considering the influences of the chaotic sea for the ARMS, the transmission is expected to not fundamentally change its behavior, since neutrons on scattering trajectories entering the measurement part have a high probability of being ejected from the system while traversing. Only, like for the mirror-mirror system, for $z_{slit} > h$ a further increase in transmission is expected in contrast to the ideal case.

Theoretical Expectations for the Quantum Mechanical Regime

For the transmission measurements using a mirror-mirror system no changes in the quantum mechanical regime with respect to the classical is expected since no removal of UCNs in absence of a surface roughness is expected.

Regarding the ARMS, in the quantum mechanical regime, the regular island and the chaotic sea composing the phase space are no longer completely separated like in the classical case, but become connected by dynamic tunneling [Fei+09], since in the quantum regime the UCNs' wave functions become relevant. The transport of UCNs through an ARMS is now determined by the interaction of their wave functions with the surface roughness and every state has, even though possibly very small, a finite interaction probability. When interacting with the rough surface, again a momentum transfer from the forward to the vertical component can take place and the neutron can therefore tunnel from the regular island to the chaotic sea and vice versa.

Furthermore, the interaction with the surface leads to wave phenomena due to interference. In detail, the propagation of the wave function from one point to another inside the ARMS can be realised by many different paths. Quantum mechanically, the total probability of reaching a given point is calculated by summing up the wave functions' amplitudes. The wave interference between multiple scattering paths can then lead to localization effects like weak localization, where the backwards direction is more probable compared to classical physics or even Anderson localization, where the particle is completely localized inside the system. Due to the state dependent interaction probability, for different states (modes) traversing the ARMS, different transport regimes can be realised at the same time. For a relatively large slit height for example, the transport of the first state will be rather ballistic since its interaction probability with the surface disorder is very small, while the transport for a higher state might be diffusive or even localized.

However, the detailed dynamics of such localization effects are very complex and are not discussed in detail within this thesis. Here, only theoretical expectations on the basis of a model developed by Westphal et al. [Wes+07] are presented. This model illustrates the main idea of the filtering process of an ARMS in the quantum mechanical regime. A more detailed discussion of the underlying theory and the derived expectations including localization effects will be presented by the theory group of S. Rotter.

The model developed by Westphal et al. assumes, that the filtering process depends on the overlap of the wave function with the surface disorder. It introduces a phenomenological loss rate $\Gamma_n(z_{slit})$, for the nth gravitational state that depends on the slit height z_{slit} of the ARMS.

The loss probability of a neutron in the nth gravitationally bound state while traversing the ARMS can in general be described by:

$$\mathrm{d}\langle\psi_n|\psi_n\rangle = -\langle\psi_n|\psi_n\rangle\,\Gamma_n(z_{slit})\mathrm{d}t. \tag{2.14}$$

Since:

$$\langle\psi_n|\psi_n\rangle = |P_n(t)|^2, \tag{2.15}$$

it follows:

$$P_n(t) = e^{-\frac{1}{2}\Gamma_n(z_{slit})t}, \tag{2.16}$$

an exponential dependence of the occupation number of the nth state $P_n(t)$ from the phenomenological loss rate and from the time the UCNs need to traverse the system. For the time needed, a neutron with a horizontal velocity of 5 m/s and a ARMS with length 20 cm and therefore $t_{final} = 0.04$ s is assumed. The dependence of the loss rate on the overlap of the wave function with the rough surface is now introduced:

$$\Gamma_n(z_{slit}) = \alpha_{loss}\int_{z_{slit}-2R_q}^{z_{slit}} dz|\psi_n(z)|^2 \tag{2.17}$$

where R_q represents the root mean square average roughness and α_{loss} is a constant depending on the roughness and material parameters of the ARMS. α_{loss} can be seen as state independent
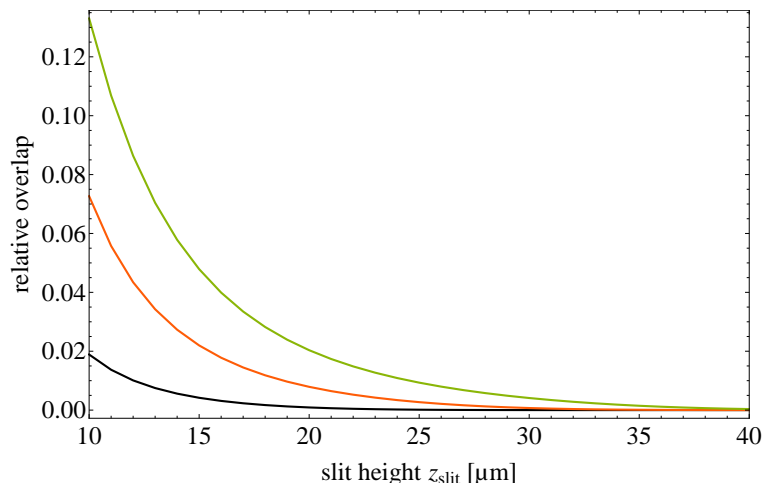
Figure 2.10: Overlap of the wave functions for the first three gravitational states with a surface roughness with $R_q = 0.75$ µm. The different overlaps of the states, leading to different removal probabilities, are clearly visible.

since the loss due to the interaction with the surface roughness should depend only on the interaction probability defined by the wave function's overlap with the roughness and the surface roughness properties themselfes.

The fraction of the wave functions belonging to the highest 1.5 µm and hence its overlap with a rough surface with $R_q = 0.75$ µm, in dependence of the slit height is shown in figure 2.10. A decrease of overlap with increasing slit height is clearly visible leading to a increase of transmission. The different overlaps of different gravitational states lead to a slit height dependent loss and therefore a slit height dependent transmission for every state. Assuming a homogeneous distribution of states at the measurement part's entrance ($P_n(t = 0) = 1 \quad \forall n$), the transmission function can simply the written as sum of occupation probabilities at the detector:

$$T(z_{slit}) = \sum_n e^{-\frac{1}{2}\Gamma_n(z_{slit})t_{final}} \tag{2.18}$$

The transmission furthermore depends on the loss constant α_{loss}, which has been used as a fit parameter for the evaluation of previously obtained measurement data. The transmission in dependence of the slit height for the first three gravitational states and the overall transmission as there sum is shown in figure 2.11a for $\alpha_{loss} = 3.4 \cdot 10^4$ as found in [Wes+07], and in figure 2.11b for $\alpha_{loss} = 5 \cdot 10^5$. The plots show the dependence of the point where the transmission starts to increase and the visibility of the steps on the loss constant α_{loss}.

Influences of Different Materials

The transport measurements were performed with different mirrors and scatterers inside the measurement part. In detail four systems have been used. A mirror-mirror system with two flat Ni-58 coated mirrors, an ARMS with a flat, Ni-58 coated mirror and a Ni-58 coated scatterer, an ARMS with a flat, borosilicate glass mirror and a Ni-58 coated scatterer and an ARMS

(a) Expected transmission ($T(z_{slit})$) in the quantum mechanical regime and contributions of the individual states for $\alpha_{loss} = 3.4 \cdot 10^4$.

(b) Expected transmission ($T(z_{slit})$) in the quantum mechanical regime and contributions of the individual states for $\alpha_{loss} = 50^5$
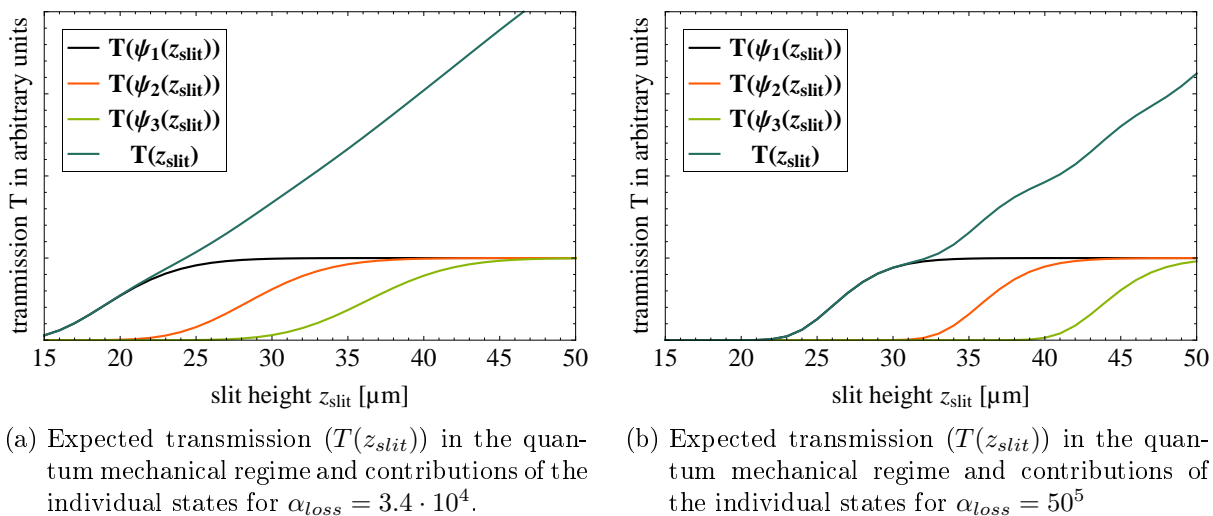
Figure 2.11: Expected transmissions at the end of the measurement part ($T(z_{slit})$) and contributions of the individual states, for the quantum mechanical regime. The stepwise increase in transmission due to the individual contributions is clearly visible. A comparison of the two plots shows the dependence of this stepwise increase and the dependence of the position of the first increase from α_{loss}.

with a flat, borosilicate glass mirror and a uncoated borosilicate glass scatterer.

Ni-58 has a higher critical velocity of $v_{cr} = 8$ m/s than borosilicate glass with $v_{cr} = 4.3$ m/s. This difference in critical velocity leads to different absorption behavior inside the different system and hence different expected results for the transmission measurements. In detail, the system using uncoated, borosilicate glass is thought to have the lowest transmission, since neutrons on scattering trajectories can be absorbed while interacting with the flat mirror or the scatterer. For the system with an flat borosilicate mirror and a Ni-58 coated scatterer transmission is expected to be higher since the scatterer's coating reduces the absorption probability. For the completely coated ARMS transmission is expected to be highest.

3 Experimental Setup

In the following chapter, the experimental setup is introduced. The reader is first lead through the design process and the final setup used, including all important components, is presented. Afterwards the investigation of the scatterers' roughness is presented. Possible sources of error, their evaluation and estimation are discussed at the end of the chapter.

3.1 Technical Realisation of the Experimental Setup

The experiment is carried out under high vacuum conditions to reduce the interaction of neutrons with atoms in the air. The setup presented below is therefore placed inside a vacuum chamber. The chamber is additionally shielded with mu-metal to prevent any magnetic field gradients from entering the system and distorting the measurements due to an interaction with the neutron's magnetic moment. Inside the vacuum chamber the setup is placed on a granite plate, offering a flatness better than 0.7 µm.

3.1.1 Design of the Experimental Setup

There were two design goals defined for the new experimental setup with respect to the first setup used in 2011. The setup then was not solely designed for the task of performing quantum transport measurements. It consisted of one long mirror, acting as a lower mirror for both, the selector as well as the measurement part and the slit height of both ARMSs was adjusted using brass spacers. The usage of brass spacers within the measurement part meant, that for every measurement point with a different slit height the vacuum had to be broken and the scatterer had to be readjusted by hand, using different brass spacers to obtain different slit heights. This procedure was very time consuming. The two design goals therefore were first, to introduce the possibility of changing the measurement part's slit height without having to break the vacuum. And secondly the new design should consist of two completely seperated parts, making it possible to use differently coated mirrors within the setup's measurement part.

For the setup mainly aluminium type EN AW 7075 is used. Aluminium is widely used as construction material in neutron physics. This is, on the one hand, due to its non magnetic nature, avoiding magnetic interactions between the experimental setup and the neutrons. And on the other hand, aluminium is a fairly light and non expensive material, making the handling of the setup easy and keeping production costs down. An illustration of the experimental setup can be seen in figure 3.1. For a schematic view see figure 2.1.
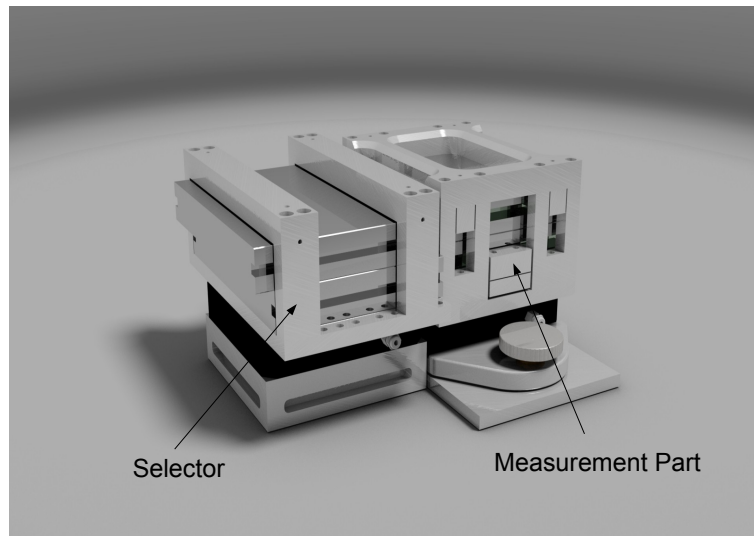
Figure 3.1: The experimental setup; neutrons enter from the left.

To introduce the possibility of changing the measurement part's slit height without having to break the vacuum, a nanopositioning stage[1] was used. This nanopositioning stage uses piezo elements for positioning along three axis and offers a closed-loop vertical/tilt range of 200 µm/2 mrad and an open-loop vertical/tilt range of 240 µm/2.4 mrad. A detailed sketch of the measurement part can be seen in figure 3.2. The mounting device for the scatterers was designed in such a way, that the upper mirrors (/scatterers) were held on top of the lower mirror from the nanopositioning stage under the lower mirror (see figure 3.3). Since it was desired to use the stages full range for measurement purposes, the stage was placed on a coarse adjustment device consisting of an aluminium plate resting on rubber springs on the measurement part's ground plate. The plate is connected to the ground plate by three screws making it possible to change the nanopositioning table's and thereby the scatterer's or upper mirror's position within a range of several millimeters. The rubber springs are acting as countering springs assuring the systems stability (see subsection 3.3.3).

Another important point to look out for during the design process was the alignment of the two parts of the experimental setup. Since the setup's two parts were now completely separated, the two lower mirrors had to be aligned to avoid a possible step. Therefore, the selector was mounted onto another nanopositioning stage (PI-518) with a range of 100 µm, offering the possibility to change it's height, thereby aligning the lower mirrors of the two parts. For the alignment process, the step between the two parts was measured using Mitutoyo linear gage laser hologages[2]. These linear displacement sensors use laser interference to detect relative displacements of their gage heads, offering a display accuracy of 0.1 µm. For their use in this experiment, the hologages are mounted to a mounting device fixed on a granite pedestal. The

---

[1]P-528 Piezo Z/Tip/Tilt Stage; Physik Instrumente (PI) GmbH & Co. KG, Auf der Römerstrasse 1, 76228 Karlsruhe/Palmbach, Germany (see `http://www.physikinstrumente.com/en/products/prdetail.php?sortnr=201510`)

[2]LGH Laser Hologage high-resolution type 542-711-1; Mitutoyo Europe GmbH, Borsigstrasse 8-10, 41469 Neuss, Germany
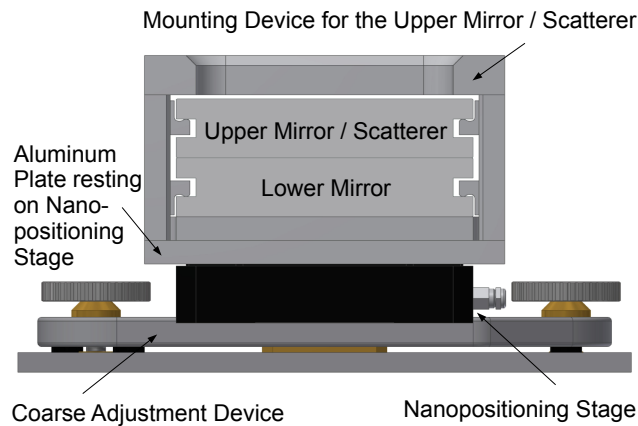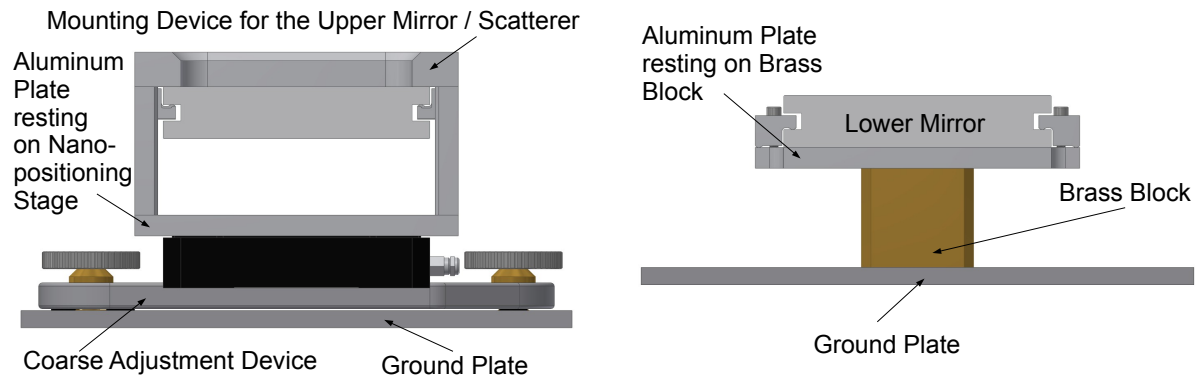
Figure 3.2: Front view of the complete measurement part.

(a) Only parts responsible to hold the upper mirror / scatterer are shown.

(b) Only parts where the lower mirror rests on are shown.

Figure 3.3: Front view of the measurement part explaining the function of the mounting device for the upper mirrors (/scatterers).

step between the two lower mirrors was measured as described in subsection 3.3.1 and the selector's height was then adjusted accordingly. This alignment process made it necessary to have space above the step to place the linear gages. This is the reason why the scatterer of the selector is not directly above it's lower mirror, but is shifted forward by 1.5 cm. For the measurement part it was not necessary to shift the upper mirror since the step was adjusted prior to the installation of the upper mirror (/scatterer). For a discussion of the changes introduced by this shift see subsection 2.2.

Since the slit height of the selector was not to be changed during the measurements, it was also in the new design fixed by brass spacers. Within the previously used setup, bass spacers spacers as long as the selector were used. For the new setup a possible influence on the prepared phase space due to the spacers, as discussed in [Chi+14] should be reduced. To do so, only four small pieces of brass spacers were employed. Furthermore, wider mirrors (20 cm)

were used for the selector than for the measurement part (15 cm). To fixate the slit height, a total of four micrometer screws, pressing the scatterer downwards against the spacers, were integrated in the upper crossbeams of the selector's casing (not shown in the sketches). A detailed sketch of the selector including captions for all important parts can be seen in figure 3.4. For a sketch of the experimental setup, including dimensions as finally used, see figure 3.5. The boron shielding visible in the sketch was installed to only allow neutrons on trajectories coming directly from the beam guide to enter the selector.
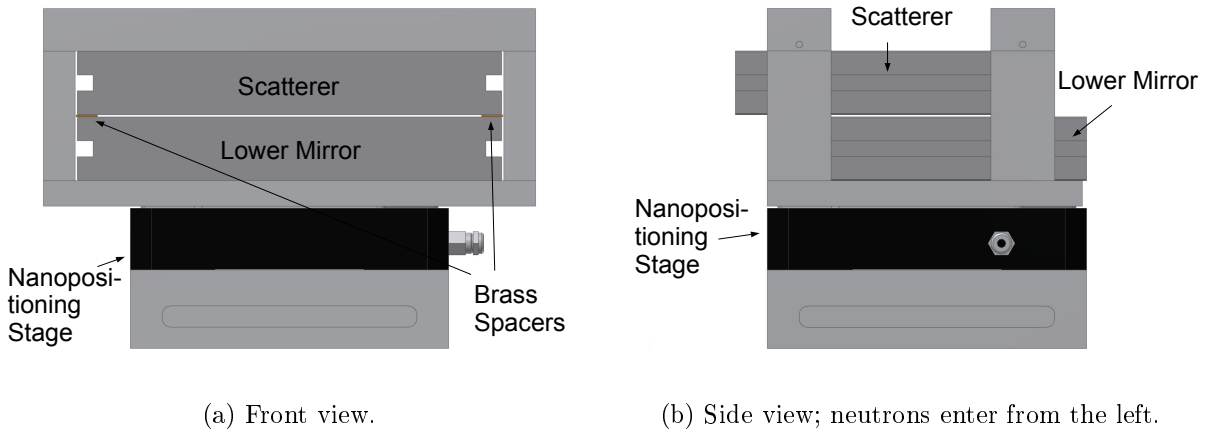

(a) Front view.

(b) Side view; neutrons enter from the left.
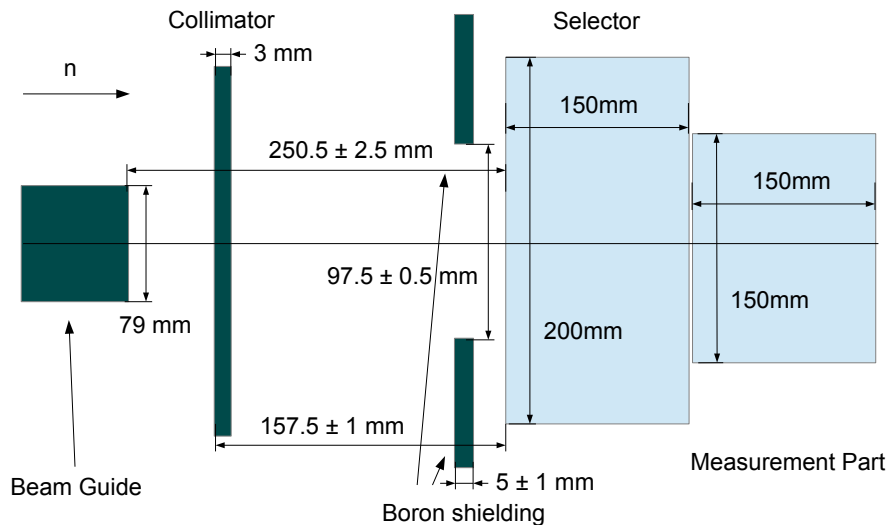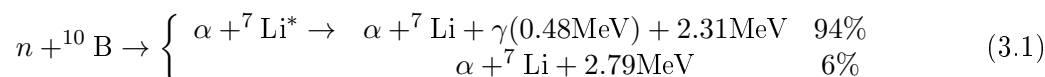
Figure 3.4: The selector.

Figure 3.5: Schematic top view of the experimental setup; not drawn to scale.

3.1.2 Detectors

Track Detector

The detector used for mapping the spatial probability distribution at the end of the selector is a solid-state nuclear detector. Here its fundamental working principle is explained shortly. For a detailed discussion see [Jen+13] or [Jen11, p24 ff]. The track detector in principle consists of a ^{10}B-coated organic substrate (CR39). Neutrons hitting the detector initiate a nuclear reaction. The reaction occurs through neutron capture of ^{10}B, which immediately decays into an α particle and a lithium ion. The conversion follows two possible channels:

$$n +^{10} \text{B} \rightarrow \begin{cases} \alpha +^7 \text{Li}^* \rightarrow & \alpha +^7 \text{Li} + \gamma(0.48\text{MeV}) + 2.31\text{MeV} & 94\% \\ & \alpha +^7 \text{Li} + 2.79\text{MeV} & 6\% \end{cases} \qquad (3.1)$$

Due to momentum conservation the decay products are emitted in almost opposite direction, ensuring that one of the particles is interacting with the organic substrate. The interaction leaves imperfections in the crystal structure of the organic substrate. After exposure, the organic substrate is subject to chemical treatment, where these imperfections are widened through etching. After the etching process, the imperfections due to the impingement of neutrons are large enough to be read out using an optical microscope and the spatial probability distribution can be investigated. The spatial resolution of such detectors can be in the micrometer regime depending on the effor put in the read out process and the efficiency is 77 % [Jen+13].

Neutron Counter

For the transmission measurements a low background electronic neutron detector developed by the qBounce collaboration was used [Sau11]. The detector is a proportional counter with an neutron converting foil at the entrance. It is specially designed for the requirements of measuring neutron transmission after a mirror system, offering an entrance slit of 110mm length and 10mm height. The foil itself consists of brass, coated with ^{10}B, converting neutrons into charged particles through the same process as shown in equation 3.1. After conversion, one of the charged decay products enters the proportional counter, where $ArCO_2$ is used as filling gas. The charged particles ionize the Argon atoms and the set free electrons are accelerated towards the anode wire. Close to the anode wire the field strength becomes large enough to produce an avalanche of electrons that is collected at the anode wire. The resulting signal is then recorded [Tha13].

3.1.3 Neutron Mirrors

The neutron mirrors used in our experiment consist of borosilicate glass (BK7) with a Fermi potential of around 100 neV and a criticlal velocity of $v_{cr} = 4.3$ m/s [Wes02, p3]. The mirrors used all have a thickness of three centimeters to reduce bending to a minimum.

Flat Mirrors

The flat mirrors used are polished to a very high degree of flatness by the producer. Roughness as well as waviness have to be very small to provide a flat surface where specular reflection can take place. Furthermore, parallelism between the top and bottom side plays an important role.

The mirrors of a former batch have been examined closely [Jen11, p23]. The mirrors' roughness and waviness were tested by S-DH[3]. The roughness (R_a) was found to be smaller 2 nm and the waviness was found to be 0.1 µm. A parallelism of smaller than 0.8 µm was demanded from the producer and was verified using an outside micrometer.

Scatterers

The scatterers are produced on basis of the flat mirrors by the glass blowing workshop of Physikalisches Institut of Universität Heidelberg[4]. To introduce roughness an abrasive powder consisting of silicon and corundum is used. The powder is mixed with distilled water and spread evenly onto a flat surface. The flat mirror is then put on top. Through moving the mirror in circles while on the abrasive mixture it roughens under the pressure of its own weight. The graining process takes about half an hour where it is interrupted several times to check and clean the mirror and renew the abrasive paste. The final roughness very much depends on the granularity of the abrasive powder used, as will be shown in subsection 3.2.4. The different granularities are stated in grains per square millimeter. A granularity of 400 therefore means, that on one square millimeter of powder 400 grains are expected to be found. The decision what granularity to use for this particular experiment has been made from experience. It was decided to use a granularity of 600, for which the filtering properties of the selector have been found to be best.

3.2 Characterisation of the Scatterers

Knowing about the scatterers' rough surfaces is, on the one hand crucial to be able to compare simulation and experimental results of the quantum transport measurements. On the other hand the roughness introduces an uncertainty on the slit height (see subsectioin 3.3.3) and is hence also an important experimental parameter. Therefore, some effort was put into the characterisation of this vital parameter.

The rough surfaces of the scatterers used were measured using a stylus instrument (or stylus profiler) Innovatest SE1700[5] with a 2µm tip radius, giving 2 D surface profiles. In addition, SEM measurements were performed on scatterers produced with differently granulated abrasive paste, yielding 3D surface data. In the following, first an introduction to rough surfaces and their characterisation is given and the evaluation method used is presented (subsection 3.2.1). Afterwards the techniques of measuring rough surfaces using a stylus instrument and using SEM are discussed (subsection 3.2.2 and 3.2.3) and the measurement results are analysed and compared (subsection 3.2.4).

3.2.1 Rough Surfaces

A rough surface is a surface with vertical deviations from the ideal, the flat surface. These deviations, the surface texture, can be different as well in amplitude as in wavelength and different textures will have different physical properties regarding interaction with another

---

[3]S-DH GmbH Heidelberg, Hans-Bunte-Straße 8-10, 69123 Heidelberg, Germany
[4]Physikalisches Institut der Universität Heidelberg, Im Neuenheimer Feld 226, 69120 Heidelberg, Germany
[5]INNOVATEST Europe BV, Borgharenweg 140, 6222 AA MAASTRICHT, The Netherlands

surface or, as in our case, regarding scattering of particles off the surface. Roughness, in detail describes the short wavelength parts of a surface's texture, apart from the waviness, describing the long wavelength parts. The distinction between the two is, however, not conclusively determined as Whitehouse points out [Whi10, p100]. There is no cut-off wavelength defined that divides the two, but the distinction has to be made in dependence of the function under which a surface is evaluated. The cut-off wavelength used for the evaluation in this thesis is discussed below. The raw measured profiles will be filterd to extract the roughness and the waviness profiles and the roughness profiles will be further evaluated. The waviness however, will not be investigated in detail here.

Evaluation of a Rough Surfaces

The evaluation of a rough surface starts with a two- or three-dimensional profile taken with some instrument (contact or non-contact). The profile consists of a series of numbers each referring to a height (z) above or below an arbitrary zero line for each measured point on the surface. The raw profile is then correct for any inclination by fitting a straight line, or a flat surface respectively, to the unfiltered data and subtracting it from the raw profile. Afterwards corrections for the waviness are applied, if necessary. The resulting profiles is then called the roughness profile.

To evaluate the roughness profile different approaches are possible. First many single value parameters exist to describe roughness. These single value parameters have been mainly developed for their use in industry and quality management and are useful in a context where one is only interested in certain surface properties, knowing and only caring about their effects. For our purpose however they are of only limited benefit since they don't provide a complete physical classification. To illustrate that, in figure 3.6 two roughness profiles with the same amplitude parameter, but different in shape, are shown. It is therefore more suitable to also include statistical and random process tools [Whi10, p41 ff] to the evaluation, to gain as much information about the roughness texture as possible. In the following, the different tools used to characterize the roughness profiles are presented.
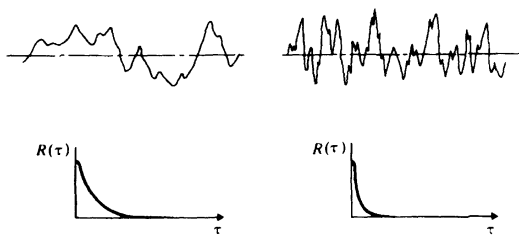

Figure 3.6: Two profiles with same amplitude parameters and there autocorrelation functions; source: [Tho99, p151, fig. 8.1]

Figure 3.7: Roughness parameter R_y; source: [Whi10, p11, fig. 2.6]

The Amplitude Parameters used in this thesis are the root mean square average R_q, the center-line average roughness R_a and the maximum roughness depth R_y. The first two are defined as:

$$R_q = \sqrt{\frac{1}{L} \int_0^L (z(x) - \bar{z}(x))^2 dx} \quad \text{or} \quad R_q = \sqrt{\frac{1}{N} \sum_i (z_i - \bar{z})^2}$$

$$R_a = \frac{1}{L} \int_0^L |z(x) - \bar{z}(x)| dx \quad \text{or} \quad R_a = \frac{1}{N} \sum_i |z_i - \bar{z}| \tag{3.2}$$

and the maximum roughness depth R_y is defined as the difference between the highest peak and the lowest valley of a measured profile (see figure 3.7).

The Amplitude Probability Density Function (APDF) of a surface gives the probability, that an arbitrary point on the surface has height z and is denoted as $p(z)$.

The actual information of the APDF can be extracted looking at the central moments. The central moments are defined as:

$$\mu_k = \int_{-\infty}^{\infty} (z - \bar{z})^k p(z) dz, \tag{3.3}$$

where $\bar{z}$ is the mean value of z, the mean height.

Especially the third and fourth central moments, normalized to the standard deviation ($\sigma = \sqrt{\frac{1}{n} \sum_{i=1}^n (z_i - \bar{z})^2}$), the skew and the kurtosis are often used. They are defined as:

$$\mu_{skew} = \frac{1}{\sigma^3} \int_{-\infty}^{\infty} (z - \bar{z})^3 p(z) dz \quad \text{and} \quad \mu_{kurt} = \frac{1}{\sigma^4} \int_{-\infty}^{\infty} (z - \bar{z})^4 p(z) dz - 3 \tag{3.4}$$

or:

$$\mu_{skew} = \frac{1}{n} \sum_{i=1}^n \left(\frac{z_i - \bar{z}}{\sigma} \right)^3 \quad \text{and} \quad \mu_{kurt} = \frac{1}{n} \sum_{i=1}^n \left(\frac{z_i - \bar{z}}{\sigma} \right)^4 - 3 \tag{3.5}$$

for the discrete case.

The skew is important since it is a measure for the symmetry of the profile while the kurtosis relates to the pointedness or bluntness of the profile. In figure 3.9 an instructive example with surfaces of different skews and kurtosises is shown and in figure 3.8 the APDF of a sine function with wavelength $\lambda = 5$mm can be seen. For a random surface, a Gaussian APDF is expected [Whi10, p43].
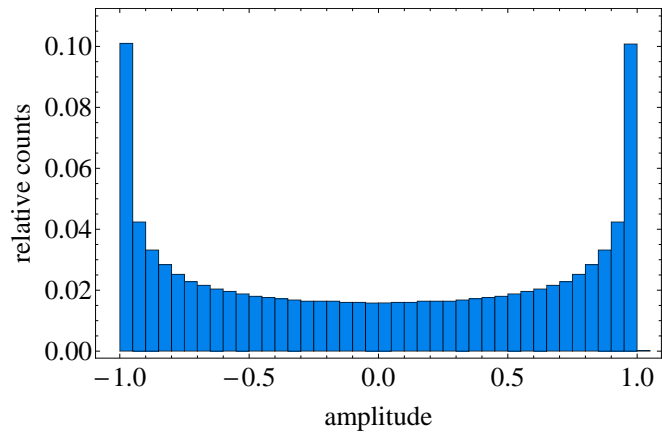

Figure 3.8: Amplitude probability density function of a sine function with wavelength $\lambda = 5$ mm

The standard deviation itself can also be used to characterize the APDF, but it is identical to the roughness parameter R_q and therefore only R_q is stated in this thesis.

(a) $\mu_{skew} > 0$ (b) $\mu_{skew} < 0$

(c) $\mu_{kurt} > 0$ (d) $\mu_{kurt} < 0$
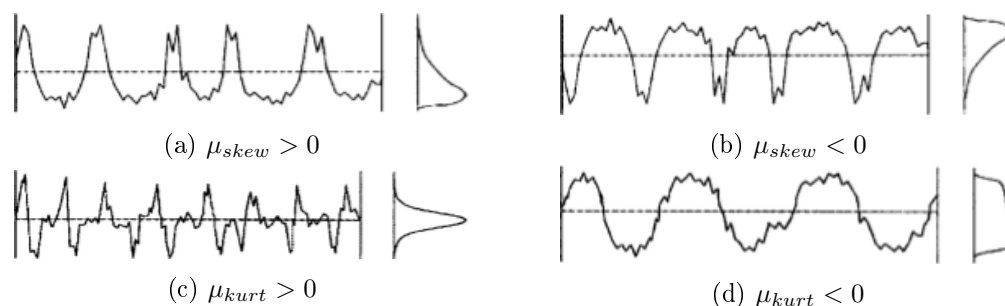
Figure 3.9: Examples for profiles with different skew and kurtosis (profiles on the left, APDF on the right): (a) $\mu_{skew} > 0$, (b) $\mu_{skew} < 0$, (c) $\mu_{kurt} > 0$, (d) $\mu_{kurt} < 0$; source: [Dav10, p44, fig. 2.4 & 2.5]

The Autocorrelation Function (ACF) is defined as:

$$A(\tau) = \lim_{L \to \infty} \frac{1}{L} \int_{-L}^{L} z(x)z(x+\tau)dx \bigg/ \int_{-L}^{L} z(x)^2 dx \qquad (3.6)$$

It is a measure for the correlation of two points on a surface depending on their distance. For two points on a surface z_1 and z_2 at a distance τ the autocorrelation function $A(\tau)$ represents the correlation of this two points in that sense, that it gives a probability for the one point being at a certain height depending on the height of the other.
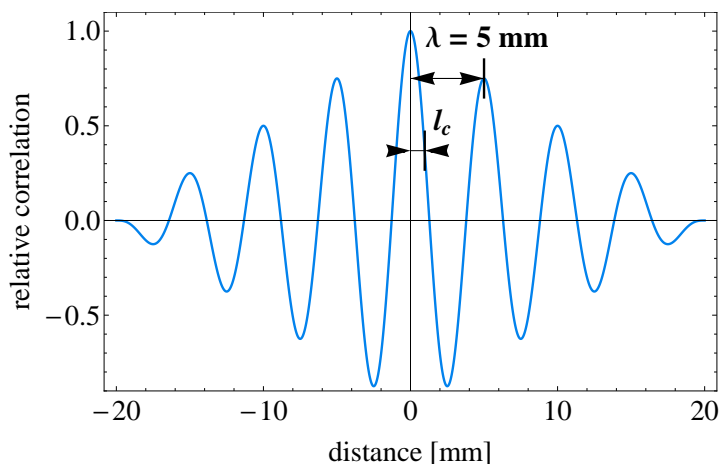

Figure 3.10: Autocorrelation function of a sine function with wavelength $\lambda = 5$ mm.

In the discrete case the definition becomes:

$$A(i\Delta x) = \sum_{j=1}^{N-i} z_j z_{j+i} \left/ \sum_{j=1}^{N} z_i^2 \right.$$

(3.7)

A useful parameter for assessing the ACF is the correlation length l_c, being defined as the length for which the ACF reduced its value to $1/e$ of its initial value $A(0)$.

The ACF of a sine function with wavelength $\lambda = 5$mm and hence frequency $\nu = 0.2$mm^{-1} can be seen in figure 3.10. The periodicity of the sine function is preserved in the oscillations of the decaying ACF. Even the wavelength is preserved as indicated in the Plot. The overall decay of the ACF is due to the finite size of the used sine profiles. For two infinitely long sine profiles the ACF would not decay but be a pure sine function again. For a completely random profile an exponentially decaying ACF is expected [Whi10, p48].

The Frequency Spectrum can be used to further investigate the properties of rough surfaces. Eventhough the ACF is connected to the power spectral density (PSD) over:

$$PSD(\nu) = 2 \int_0^\infty A(\tau) cos(\nu\tau) d\tau,$$

(3.8)

and therefore also contains information about the wavelength and frequencies involved (see figure 3.10), using the frequency spectrum can be useful, since it illustrates the frequency dependence in a more direct way. The following discussion mainly follows [HS02].

To calculate the spectra the Fourier transform, defined as:

$$F(\nu) = \int_{-\infty}^{\infty} f(z) e^{-2\pi i z \nu} dz,$$

(3.9)

or in the discrete case:

$$F_m = \sum_{k=1}^{N} z_k e^{-2\pi i \frac{(m-1)(k-1)}{N}}, \quad m = 1...N,$$

(3.10)

is needed. Since the Fourier transformation is calculated for roughness profiles, real valued arrays of length N, the upper half of the Fourier array $(F_{N/2+2}...F_N)$ is redundant. The discrete and finite form of the profiles, furthermore introduces aliasing effects. The Hanning window was therefore used to reduce this effects. It can be seen in figure 3.11 and is defined as:
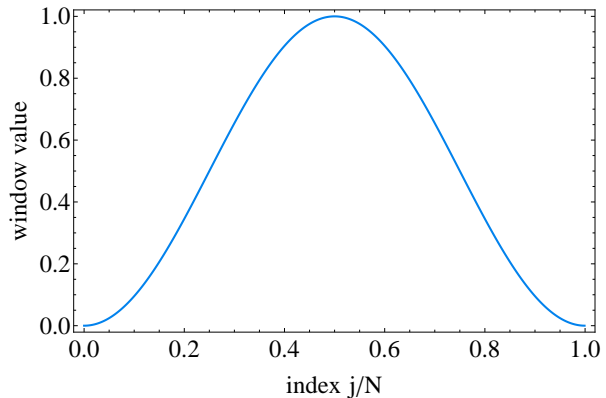

Figure 3.11: The Hanning window

$$H_i = \frac{1}{2} \left(1 - \cos 2\pi (i-1)/N \right), \quad i = 1....N$$

(3.11)

In this thesis the linear spectrum was used to perform the spectral analysis since it displays the amplitudes of the sine waves involved correctly. To obtain the linear spectrum, the roughness profile was first multiplied by the Hanning window. From the resulting array the discrete Fourier transform (DFT) was calculated and the spectrum was obtained from:

$$LS_m = 2\sqrt{\frac{|F_m|^2}{S^2}}, \quad m = 1...N/2 + 1 \tag{3.12}$$

where S is a normalisation constant due to the usage of the Hanning window.

The mean frequency $\bar{\nu}$ of the spectrum is defined as:

$$\bar{\nu} = \int \nu LS(\nu)d\nu \left/ \int LS(\nu)d\nu \right., \quad \text{or} \quad \sum_i \nu_i LS_i \left/ \sum_i LS_i \right. \tag{3.13}$$

and has been calculated as a parameter of the spectrum.

The linear spectrum of the sum of two sine functions, one with wavelength $\lambda_1 = 0.5$ mm (frequency $\nu_1 = 2$ mm^{-1}) and amplitude 1 mm, and one with wavelength $\lambda_2 = 0.05$ mm (frequency $\nu_2 = 20$ mm^{-1}) and amplitude 2 mm is shown in figure 3.12. The mean frequency is $\bar{\nu} = 14$ mm^{-1}. As one can see, the linear spectrum displays the amplitude of the sine functions correctly.
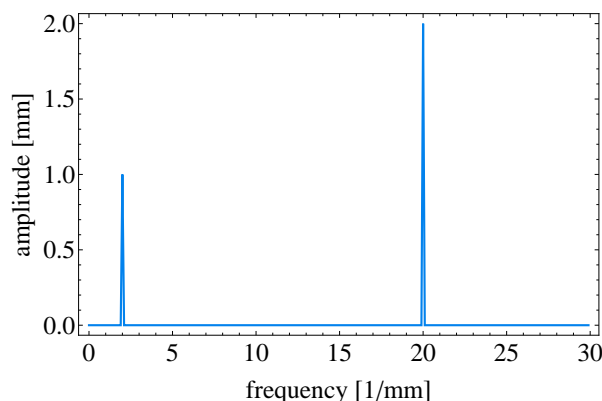
If one computes a spectrum on basis of one profile the standard deviation of one frequency bin is 100%. This error can be reduced by taking the average of several (n) spectra computed from n profiles and thereby reducing the error by a factor of $1/\sqrt{n}$. Regarding the roughness profiles, several measurements for every scatterer were performed and their spectra were calculated and averaged over.

Figure 3.12: Linear spectrum of the sum of two sine functions with wavelengths $\lambda_1 = 0.5$ mm (frequency $\nu_1 = 2$ mm^{-1}) and $\lambda_2 = 0.05$ mm ($\nu_2 = 20$ mm^{-1})

Comparison of roughness 2D and 3D roughness data

To compare the 2D roughness profiles taken with the stylus instrument and the 3D surface data obtained from SEM measurements, 20 2D profiles were taken from equidistant lines along both direction of the 3D surface data. The profiles were then analysed and the results were compared. See below for the evaluation process of the profiles obtained with the stylus instrument and subsection 3.2.3 for the profiles obtained with SEM. The results are presented in subsection 3.2.4.

3.2.2 Measurement of Rough Surfaces Using a Stylus Instrument

A stylus instrument uses a small stylus with a diamond tip on top which is pulled over a surface to measure the surface texture, and hence is a contact method for measuring surface textures. This technique is widely used since it is fairly easy and fast, but it is also subject to several problems. Here, first the function of a stylus instrument in general and the stylus instrument used is presented and the problems of the method as well as the approaches for their treatment are discussed. Thereafter measurements using calibration specimens to test the stylus instrument are presented and the concluded approach to analyse the measurements performed on the scatterers is shown.

A stylus instrument records a surface profile of several millimeters length. Most stylus instruments, including the one used here, are able to automatically perform an analysis of the measured profile. The analysis consists of filtering the profile taken for long wavelength parts (the waviness) and automatically calculating roughness parameters defined by different standards (e.g. ISO97 or JIS94). The output, consists of the raw measured profile, the calculated waviness, the evaluated roughness profile and the calculated parameters.

One of the biggest limitations presents the finite radius of the tip used. It is obvious, that however small the tip is there will always be a valley where it will not be able to follow the real surface texture and hence record a wrong profile (see figure 3.13). Furthermore distortions of the real profile occur due to the fact, that for different slopes the contact point on the stylus tip changes. This effect leads to an adding of curvature of the surface asperities and a subtraction of curvature from the valleys [Whi10, p258]. Another issue of stylus instruments is noise. As Poon and Bhushan point out [PB95], stylus instruments are subject to long wavelength noise in the time domain. Finally, one should keep in mind, that due to the contact between the surface and the tip the surface will always be damaged to some degree by the tip.
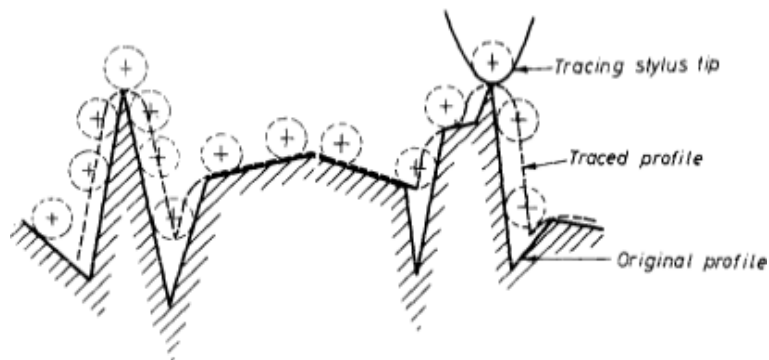

Figure 3.13: Visualization of the effect of the stylus tip radius on the measured profile [Rad70, p326, fig. 1]

To tackle the problem of the finite tip size, Cho and Lee [LC12] investigated the influence of the stylus tip by comparing measurements taken with a stylus instrument with measurements taken with an atomic force microscope and 2D as well as 3D simulations. They were able
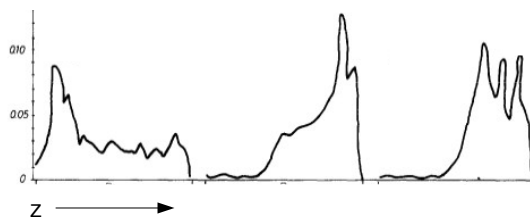
Figure 3.14: Influence of the tip radius (r) on the APDF, left: r = 20µm; middle: r = 550µm; right: r = 3200µm; source: [Rad70, p330, fig. 6]

to obtain a wavelength limit in dependence of the stylus tip radius and the R_q value of the measured profile:

$$\lambda_{min} = 10.915 \left(\frac{R_q}{r_{tip}}\right)^{0.47} r_{tip} \tag{3.14}$$

Those parts of the measured profile with wavelength smaller than the limit are distorted due to the finite tip size and are therefore to be discarded.

Radhakrishnan [Rad70] also investigated the influences of the finite tip size. While comparing measurements from the same surface performed with different tip radii he found a shift of the APDF due to the tip radius (see figure 3.14). This shift is due to the fact, that with increasing tip size more and more valleys can not be reached anymore. The shift can also be parameterised by an increasing negative skewness of the APDF with increasing stylus tip. Regarding the roughness parameters he found a reduction of R_a as well as R_t with increasing tip size.

The results of Radhakrishnan have also been verified by Poon and Bhushan [PB95], who have performed simulations of circles of different radii moving over a profile taken with an atomic force microscope (AFM) and also measured surfaces using AFM and stylus instruments. They found that the roughness parameters reduced with increasing radius and the correlation length increased with incresing tip radius, in their simulations as well as in their performed measurements.

The long wavelength noise introduced to the raw surface profile influences mostly the waviness. This is due to the filtering of the raw profiles for long wavelength parts. The stylus instrument used offers a filter to extract the waviness from the raw surface profile. The actual function of the filter is unknown since no information about it is offered by the instruments manual. According to Bodschwinna [BH92, p86], the filter usually used is a moving average with a Gaussian, or a triangular average function. The Gaussian function used is:

$$S(x) = \frac{1}{\alpha\lambda_c}e^{-\pi\left(\frac{x}{\alpha\lambda_c}\right)^2} \tag{3.15}$$

Here λ_c represents the cut-off wavelength that can be chosen by the user and $\alpha = 0.4697$ is a constant. A filter according to Bodschwinna has been implemented manually and compared with the stylus instruments internal filter. The extracted waviness was investigated for it's reliability by performing repeated measurements along the same paths. The results are discussed below.

Testing the Stylus Instrument using Calibration Specimens

To test the stylus instrument and gain insight about it's integrated roughness analysis, its functionality using calibration specimens was tested. The specimens used were a Mitutoyo roughness specimen[6] with a nominal roughness of $R_a = 0.42$ µm / $R_y = 1.5$ µm and $R_a = 2.95$ µm / $R_y = 11.4$ µm respectively and a Innovatest roughness specimen with a nominal roughness of $R_a = 3$ µm, which was included with the stylus instrument itself. Detailed information about shape of the specimens' surfaces were not available. On each specimen several measurements were performed, varying the instruments parameter.

An example of raw profiles for every calibration specimen taken by the stylus instrument can be seen in figure 3.15. The profiles are shown over the whole measured length of several millimeters. The visible curvature clearly shows the containment of long wavelength parts. It is therefore necessary to filter the raw profiles for these long wavelength parts.
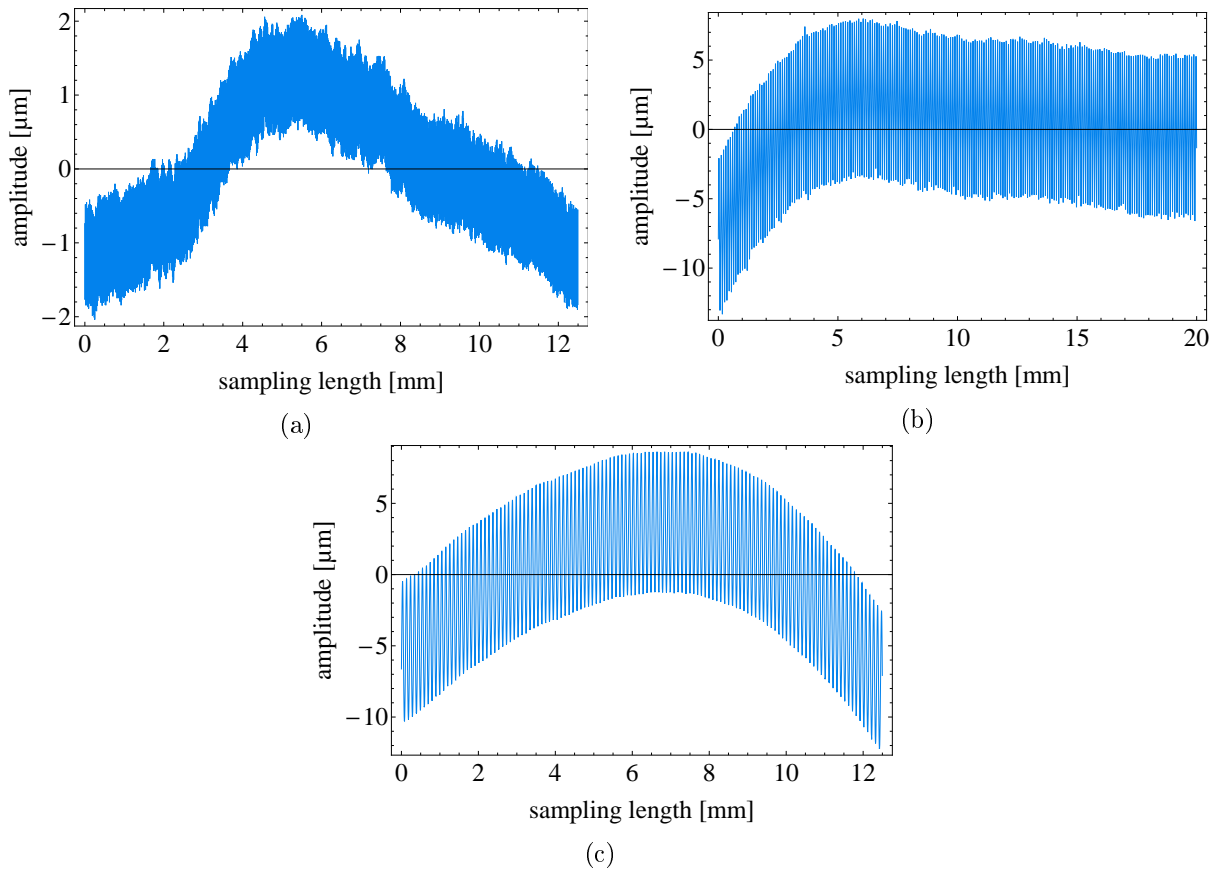

(a)

(b)

(c)

Figure 3.15: Raw profiles of (a) calibration specimen $R_a = 0.42$ µm, (b) calibration specimen $R_a = 2.95$ µm, (c) calibration specimen $R_a = 3$ µm; the profiles are shown over the whole measurement length of several milimeters; the containment of long wavelength parts is cliearly visible in the bending of the profiles.

---

[6]Roughness Specimen, Code No. 178-604; Mitutoyo Europe Gmbh, Borsigstrasse 8-10, 41469 Neuss, Germany
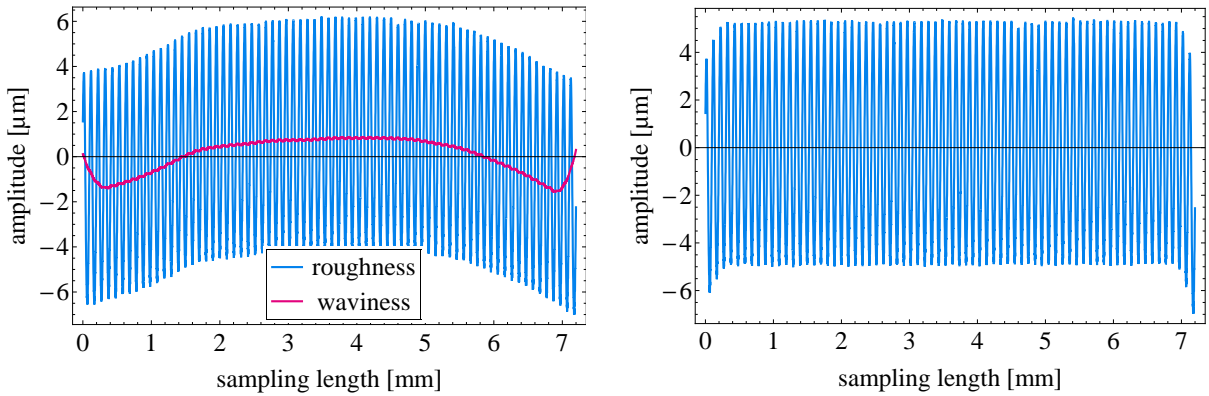
To test the waviness calculated by the instrument's internal filter, a moving average filter according to equation 3.15 and one using a triangular filter function was implemented. The wavinesses calculated by the instrument's internal filter in comparison with the wavinesses calculated manually, both for a cut-off wavelength of $\lambda_c = 2.5$mm, can be seen in figure 3.16a. The wavinesses calculated manually are shorter since a part of length $\lambda_c/2$ of the measured profile has to be taken on each side to calculate the moving average. The waviness calculated by the instrument and the moving average filters, in this case, are in good agreement with each other. However, this is not the case for every measurement. In figure 3.16b the waviness of another measurement of the calibration specimens with $R_a = 3$µm is shown. Here the filtered wavinesses do not agree to such an extend as in the previous measurement. It was not possible to determine the source for this discrepancy since the parameters chosen for the instrument were the same as in the former example. If one has a closer look at the waviness calculated by the stylus instrument, however, the ascend at both sides of the measurement strike out. A comparison with the raw profile (fig. 3.17a) does not indicate a reason for this ascends and indeed, when using the waviness calculated by the instrument to correct the raw profile, an imperfect roughness profile still containing long wavelength parts at the sides (see figure 3.17b) is obtained. The waviness calculated by the sylus instrument is therefore concluded to be unreliable and for further evaluations it is always counter checked with the implemented filters. In case the two filtered wavinesses agree with each other the corrected profile produced by the instrument is taken, since it offers a longer profile length, and the implemented filters are used if not so.
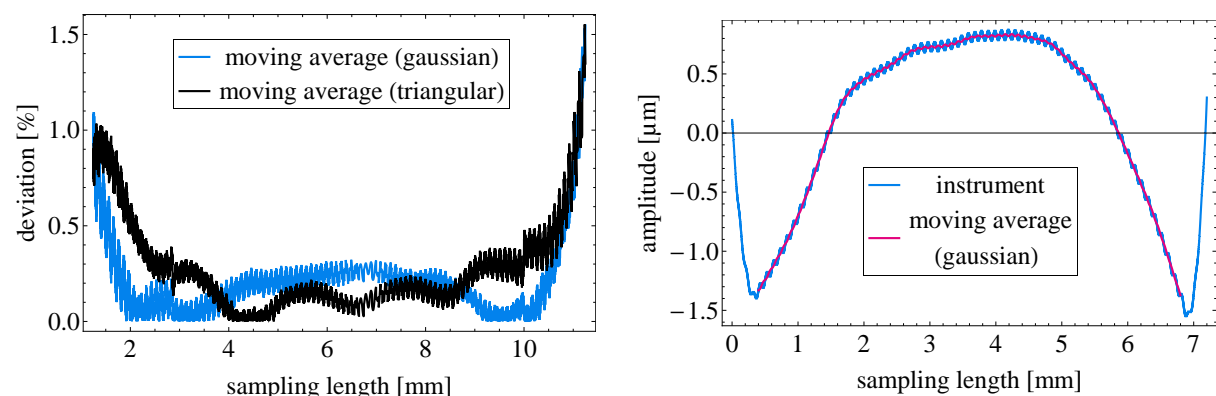
(a) The wavinesses calculated by the instrument and with the implemented gaussian and triangular moving average filters are in good agreement with each other.

(b) The waviness calculated by the instrument differs from the waviness calculated using the gaussian moving average filter for unknown reasons.

Figure 3.16: Comparison of different waviness filters. In (a) the difference between the instrument's filter and the moving average filters for a cut-off wavelength $\lambda_c = 2.5$mm from one measurement on the specimen with $R_a = 3$µm is shown. In (b) the calculated wavinesses for a cut-off wavelength of $\lambda_c = 0.8$mm from a different measurement on the specimen with $R_a = 3$µm can be seen.

Regarding the choice of a cut-off wavelength λ_c for calculating the wavinesses, a comparison of wavinesses calculated for different cut-off wavelengths λ_c, of one measurement of the specimen

(a) Raw roughness profile and waviness calculated by the stylus instrument with unreasonable ascends at the sides.

(b) Roughness profile from (a) corrected by the waviness from (a). The decrease on the sides indicates the incorrectness of the waviness.

Figure 3.17: Example of incorrect correction for waviness by the stylus instrument, of a measurement performed on the calibration specimen with $R_a = 3\mu$m. (a) Waviness, calculated by the stylus instrument and raw profile, and (b) corrected profile.

with $R_a = 3$µm, is shown in figure 3.18a. One can clearly see, that for a lower value of λ_c the filtered waviness gets closer to the measured profile (figure 3.18b). This of course affects the APDF and other amplitude parameters and the cut-off wavelength therefore has to be chosen with caution. To further investigate the effect of the long wavelength filter the linear spectra are investigated. In figure 3.19 the combined linear spectra of three measurements performed on the calibration specimen $R_a = 3$ µm, filtered with different cut-off wavelengths are shown. Since the differently filtered profiles have different length, for comparison only the coinciding profile segments were taken. The spectrum of the unfiltered profiles contains the the long wavelength (short frequency) part, visible as the falling slope at very low frequencies (see inset in figure 3.19a). This part is, as said before, filtered out by the moving average filter, as can be seen in the following figures (insets in (b)-(e)). The main contribution to the roughness comes from frequencies around $10\mu\text{m}^{-1}$ (see the large peaks). Concerning the choice of filters, in this case one can see that for cut-off wavelengths higher that 0.08mm the main peak in the spectrum stays almost the same and hence is rarely influenced by the filter. Only for a cut-off wavelength of 0.08mm the main peak decreases significantly and the roughness itself is therefore distorted. This can also be seen by comparing the calculated R_a values for different cut-off wavelength as done in table 3.1. These results suggest that a cut-off wavelength of 0.25 mm would be the best choice since it gives an R_a value closest to the nominal value of the calibration specimen. However, if one has again a look at figure 3.18a, one clearly sees, that for this cut-off wavelength the waviness already includes short wavelength parts belonging to the roughness and is distorting the roughness profile. It is therefore concluded, that for the calibration specimen with $R_a = 3$ µm a cut-off wavelength of 2.5 mm is best taken, as also suggested by DIN EN ISO 4288:1998. For the calibration specimen with $R_a = 0.42$ µm a similar analysis showed a best result for a cut-off wavelength of 0.8 mm as also suggested by the ISO standards.
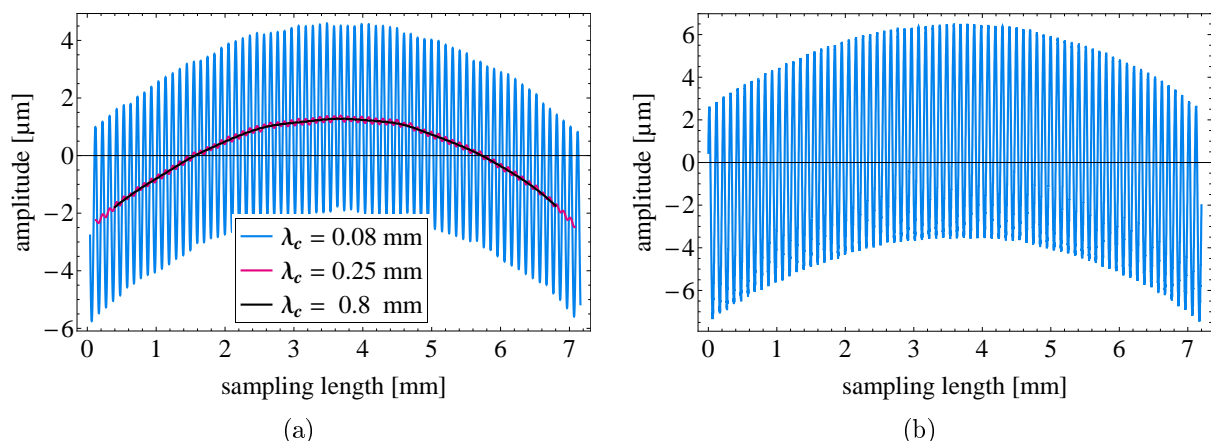
Figure 3.18: (a) Wavinesses filtered with different cut-off wavelength λ_c and (b) raw profile of one measurement from the calibration specimen with $R_a = 3$ µm. For smaller cut-off wavelength λ_c the extracted wavinesses resemble the raw profile to a higher degree.

| Specimen / λ_c	$R_a = 0.42$µm	$R_a = 2.95$µm	$R_a = 3$µm
$\lambda_c = 0.08$mm	0.433 ± 0.013	1.209 ± 0.032	1.104 ± 0.020
$\lambda_c = 0.25$mm	0.433 ± 0.013	3.210 ± 0.112	3.131 ± 0.062
$\lambda_c = 0.8$mm	0.435 ± 0.014	3.248 ± 0.115	3.190 ± 0.064
$\lambda_c = 2.5$mm	0.437 ± 0.015	3.260 ± 0.125	3.180 ± 0.060

Table 3.1: R_a values for different cut-off wavelengths λ_c for the calibration specimens

As a next step, the profiles were filtered for short wavelengths according to [LC12]. To do so, the minimal wavelength resolvable with a stylus instrument (λ_{min}) was calculated following equation 3.14 and the profiles were filtered using a Gaussian lowpass filter. The maximum frequencies (ν_{max}) corresponding to the minimal wavelengths, for the different calibration specimens, are shown in table 3.2. The values shown are the mean values of all measurements performed per specimen and the respective standard deviations. Furthermore the linear spectra before and after filtering are shown in figure 3.20. The influence of the short wavelength correction can also be seen in figure 3.21 were parts of the profiles before and after filtering are shown. The influence of the filtering can be seen particularly good for the $R_a = 3$µm specimen (3.21c).

| Specimen	ν_{max} [1/mm]
$R_a = 0.42$µm	88.597 ± 1.557
$R_a = 2.95$µm	34.117 ± 0.625
$R_a = 3$µm	35.029 ± 0.308

Table 3.2: Maximal resolvable frequencies for the different calibration specimens

Parts of the obtained profiles, after applying the corrections as described, and the APDFs of the combined profiles can be seen in figure 3.22. The linear spectra of the final profiles can be seen in figure 3.23 and the respective mean frequencies ($\bar{\nu}$) are stated in table 3.6. The values for the amplitude parameters R_a and R_y, calculated by the instrument and calculated from the filtered roughness profiles, can be seen in table 3.5. The values after filtering are, in general, closer to the nominal values of the calibration specimens. Furthermore the APDFs have been analysed and the moments of the APDFs are stated in table 3.6 as well.
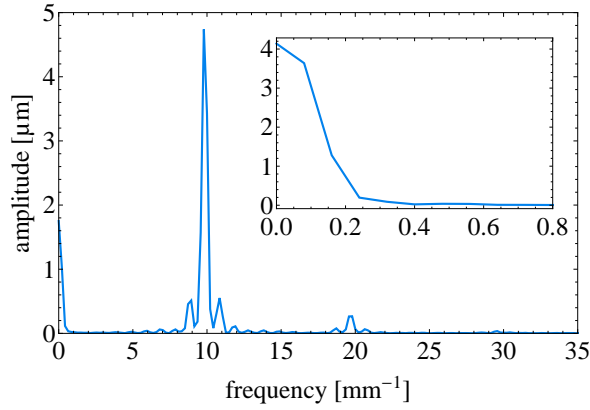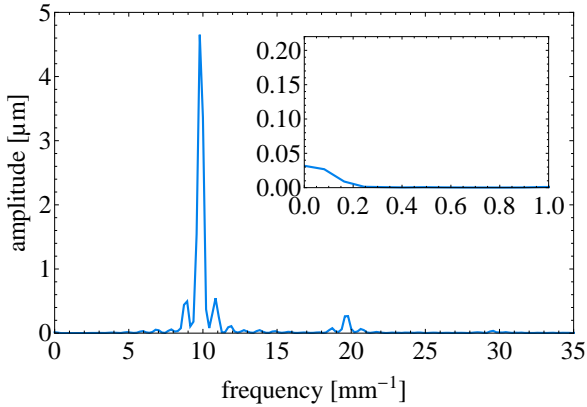
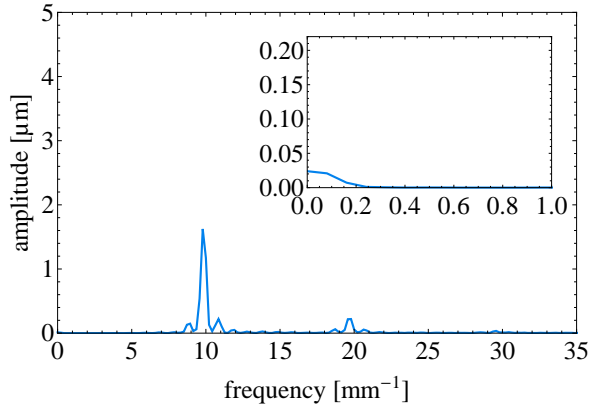(a) Linear spectrum for the unfiltered profile.
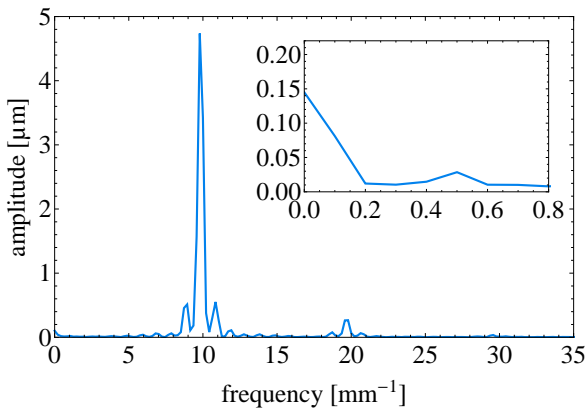
(b) Linear spectrum for a cut-off wavelength $\lambda_c = 2.5$ mm.
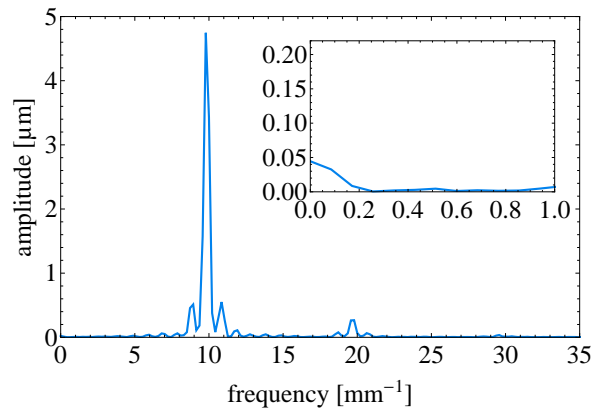
(c) Linear spectrum for a cut-off wavelength $\lambda_c = 0.8$ mm.

(d) Linear spectrum for a cut-off wavelength $\lambda_c = 0.25$ mm.

(e) Linear spectrum for a cut-off wavelength $\lambda_c = 0.08$ mm.

Figure 3.19: Linear spectra of measurements for the calibration specimen $R_a = 3$ µm filtered with different cut-off wavelengths λ_c ((a)-(e)). The Insets show the magnified low frequency parts of the spectra. The low frequency parts decrease with decreasing cut-off wavelength. For $\lambda_c \leq 0.25$ mm also the main peak at around 10 mm^{-1} starts to decrease due to the wavelength filtering.
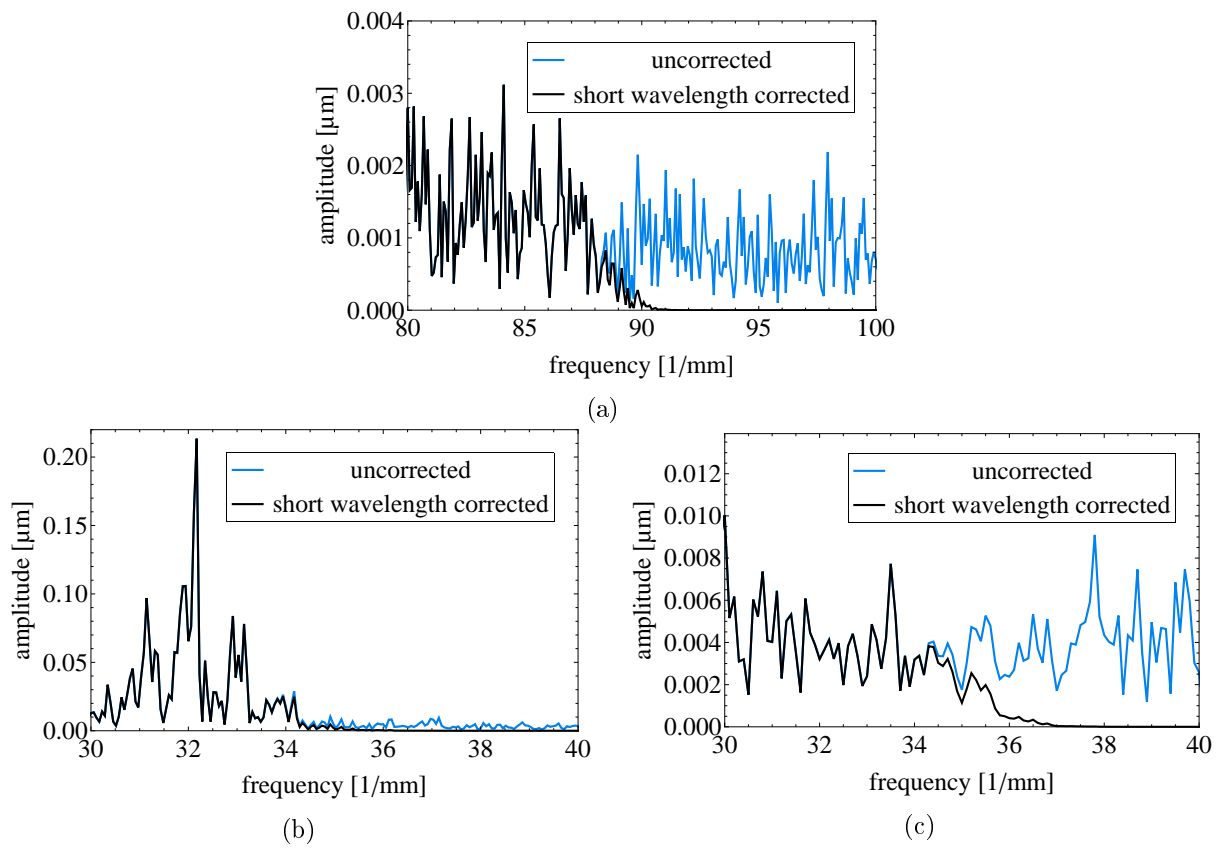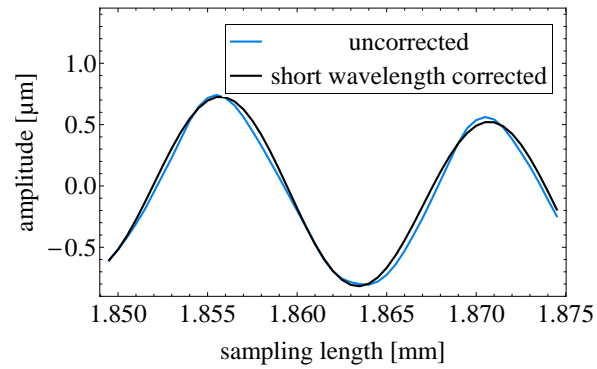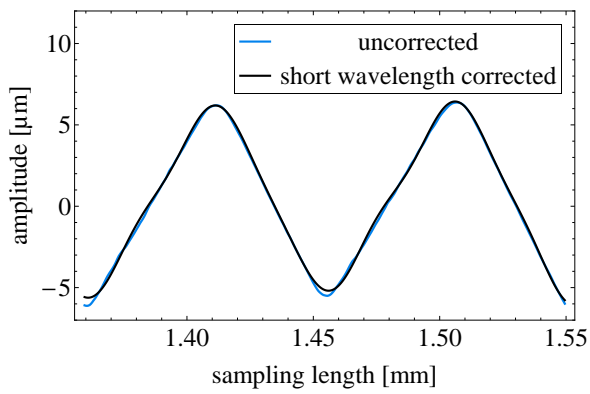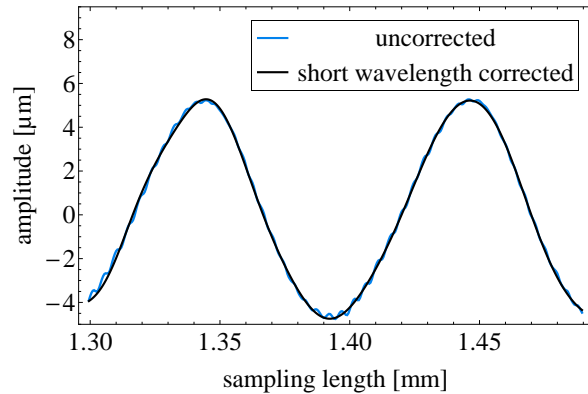
(a)

(b)

(c)

Figure 3.20: Comparison of linear spectra before and after applying short wavelength corrections of (a) calibration specimen $R_a = 0.42\mu m$, (b) calibration specimen $R_a = 2.95\mu m$, (c) calibration specimen $R_a = 3\mu m$; only the region around the minimal resolvable wavelength is shown
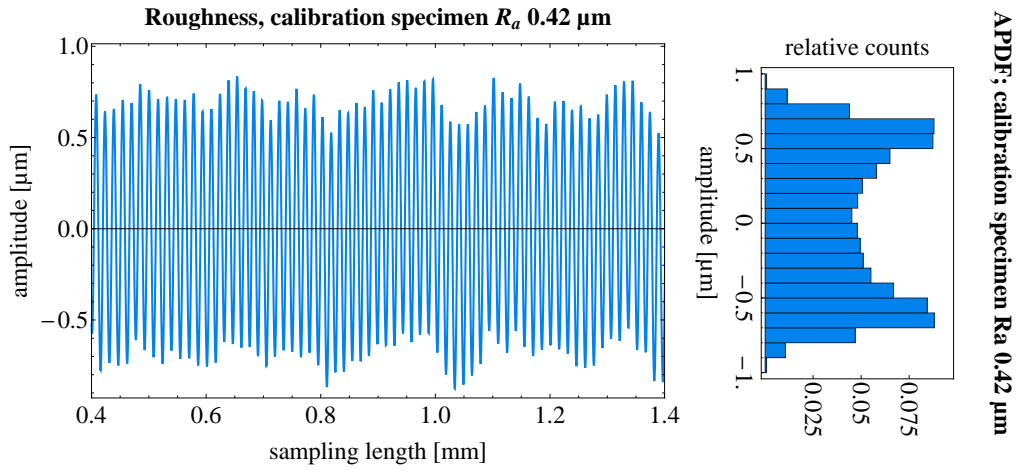
Figure 3.21: Comparison of profiles before and after applying short wavelength corrections of (a) calibration specimen $R_a = 0.42$ µm, (b) calibration specimen $R_a = 2.95$ µm, (c) calibration specimen $R_a = 3$ µm. The smoothing due to the short wavelength correction is particularly visible in (c).
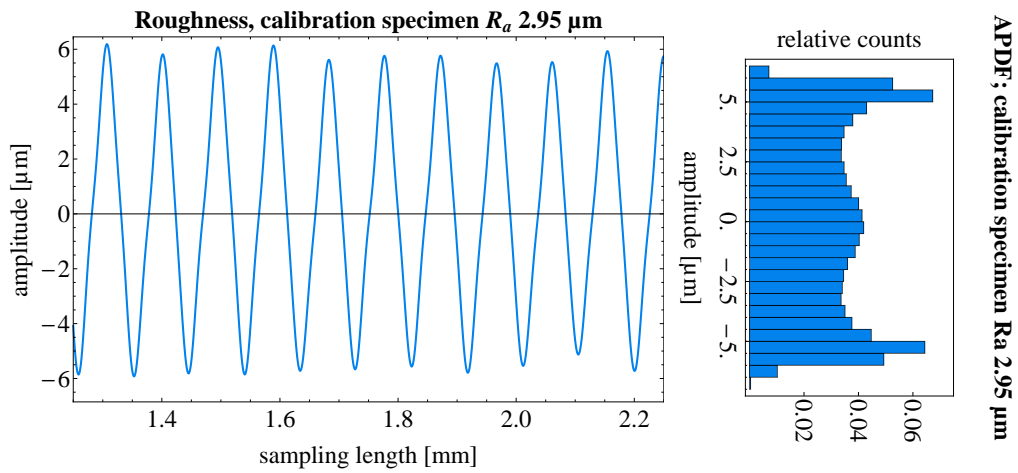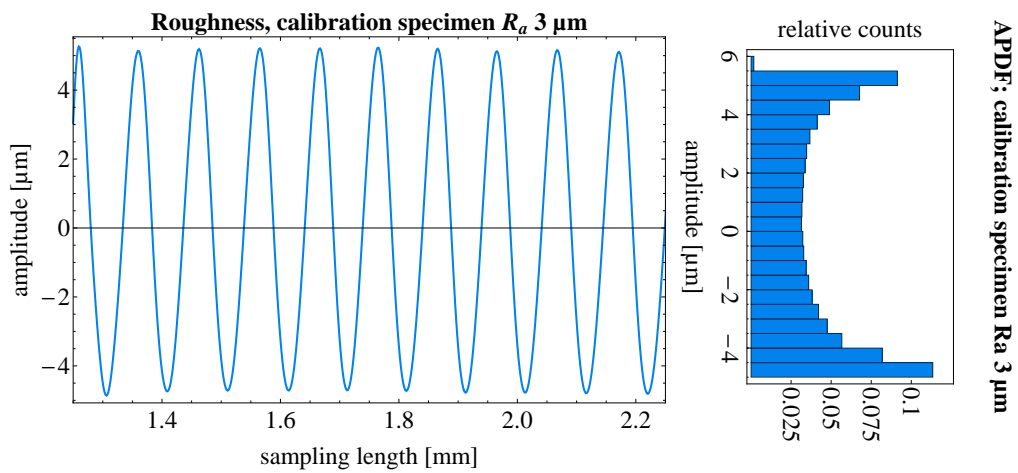
Figure 3.22: Filtered roughness profiles and APDF of (a) calibration specimen $R_a = 0.42$µm, (b) calibration specimen $R_a = 2.95$µm, (c) calibration specimen $R_a = 3$µm; only 1mm of the measured length is shown to increase visibility; information of full measured length taken for the APDFs

Figure 3.23: Linear spectra of (a) calibration specimen $R_a = 0.42\mu\text{m}$, (b) calibration specimen $R_a = 2.95\mu\text{m}$, (c) calibration specimen $R_a = 3\mu\text{m}$.

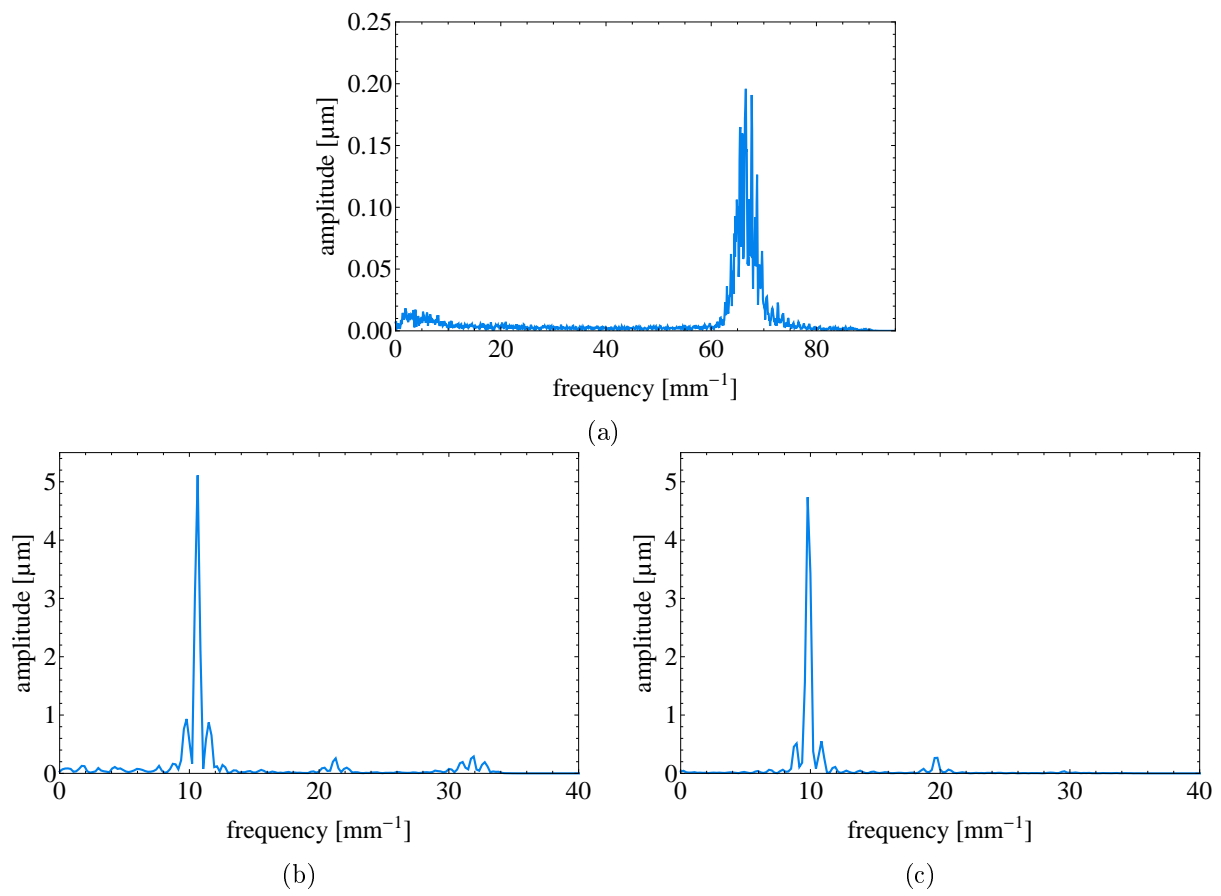To see whether the stylus instrument is suspect to long wavelength noise as mentioned above, repeated measurements of the same surface profile were compared. This was done for the R_a = 3µm as well as for the R_a = 2.95µm specimen. The measured profiles, after correcting for an offset, matched to a relative high degree. Parts of the profiles, as well as the calculated wavinesses, can be seen in figure 3.24. The reproducibility shows, that the stylus instrument is subject to only a small amount of long wavelength noise and it is therefore possible to use it to at least estimate the waviness.

	R_a [µm]	R_y [µm]	R_a [µm]	R_y [µm]
nominal value	0.42	1.5	2.95	11.4
instrument value	0.437 ± 0.012	2.05 ± 0.13	3.250 ± 0.109	13.517 ± 0.702
calculated value (after long-wavelength corrections)	0.435 ± 0.014	1.776 ± 0.095	3.263 ± 0.125	12.959 ± 0.267
calculated value (after short-wavelength corrections)	0.436 ± 0.015	1.807 ± 0.090	3.255 ± 0.125	12.687 ± 0.308

(a)   (b)

Table 3.5: Values of amplitude parameters of
(a) calibration specimen R_a = 0.42µm,
(b) calibration specimen R_a = 2.95µm,
(c) calibration specimen R_a = 3µm.

R_a [µm]	R_y [µm]
3	n/a
3.180 ± 0.061	12.185 ± 0.312
3.180 ± 0.060	10.385 ± 0.284
3.178 ± 0.058	10.346 ± 0.205

(c)

Finally, the ACFs for the final roughness profiles were calculated. The mean ACFs of every specimen can be seen in figure 3.25 and the correlation lengths are stated in table 3.6. The ACFs resemble the high periodicity of the calibration specimens.

Specimen	$R_a = 0.42$ µm	$R_a = 2.95$ µm	$R_a = 3$ µm
Skewness	-0.001 ± 0.006	0 ± 0.005	0.105 ± 0.002
Kurtosis	-1.401 ± 0.022	-1.292 ± 0.003	-1.481 ± 0.002
$\bar{\nu}$ [mm^{-1}]	54.606 ± 1.592	13.1129 ± 0.386	10.902 ± 0.049
Correlation length [µm]	2.864 ± 0.027	17.645 ± 0.076	18.376 ± 0.018

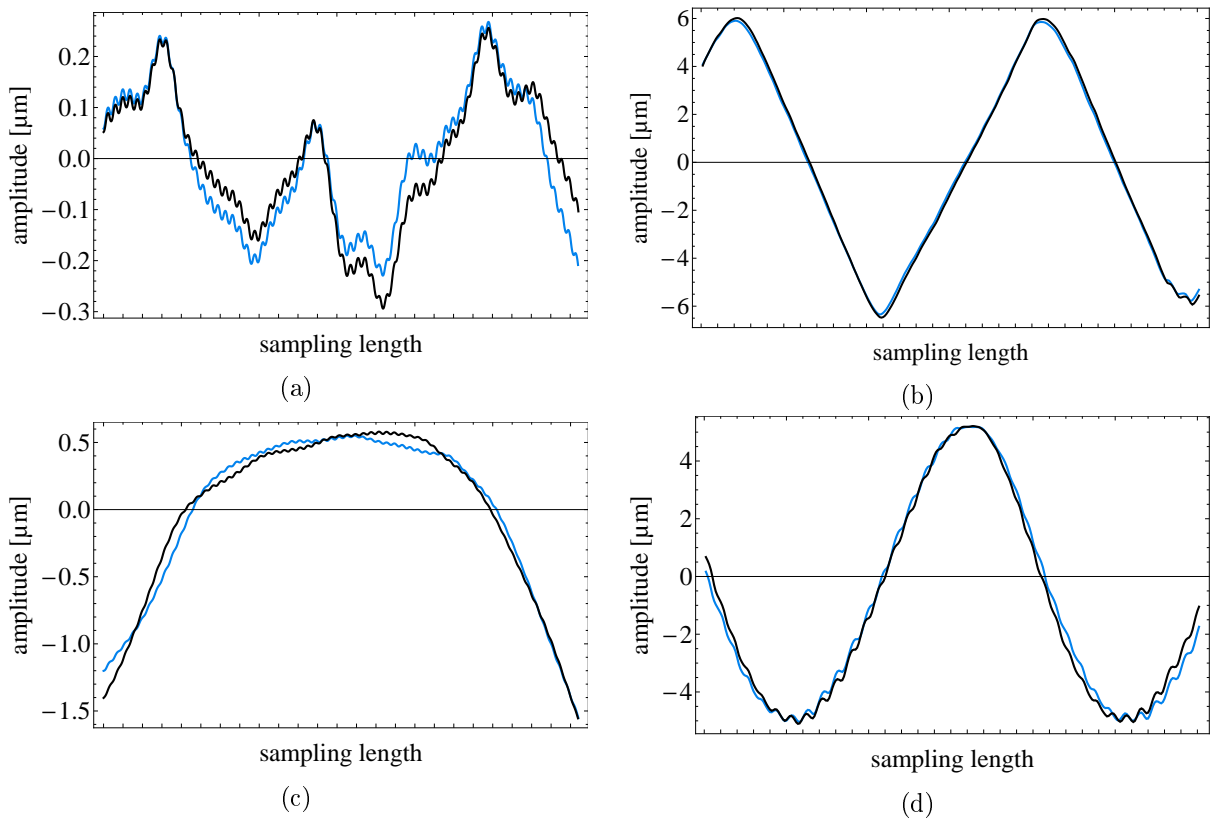Table 3.6: Parameters of the APDFs, mean wavelengths and correlation lengths of the final roughness profiles.

Figure 3.24: Comparison of the wavinesses of two repeated measurements along the same path for (a) callibration specimen $R_a = 2.95$ µm and (c) callibration speciment $R_a = 3$ µm and parts of the profiles (b) and (d) respectively. The plots show the reproducability of measurements performed with stylus instrument.
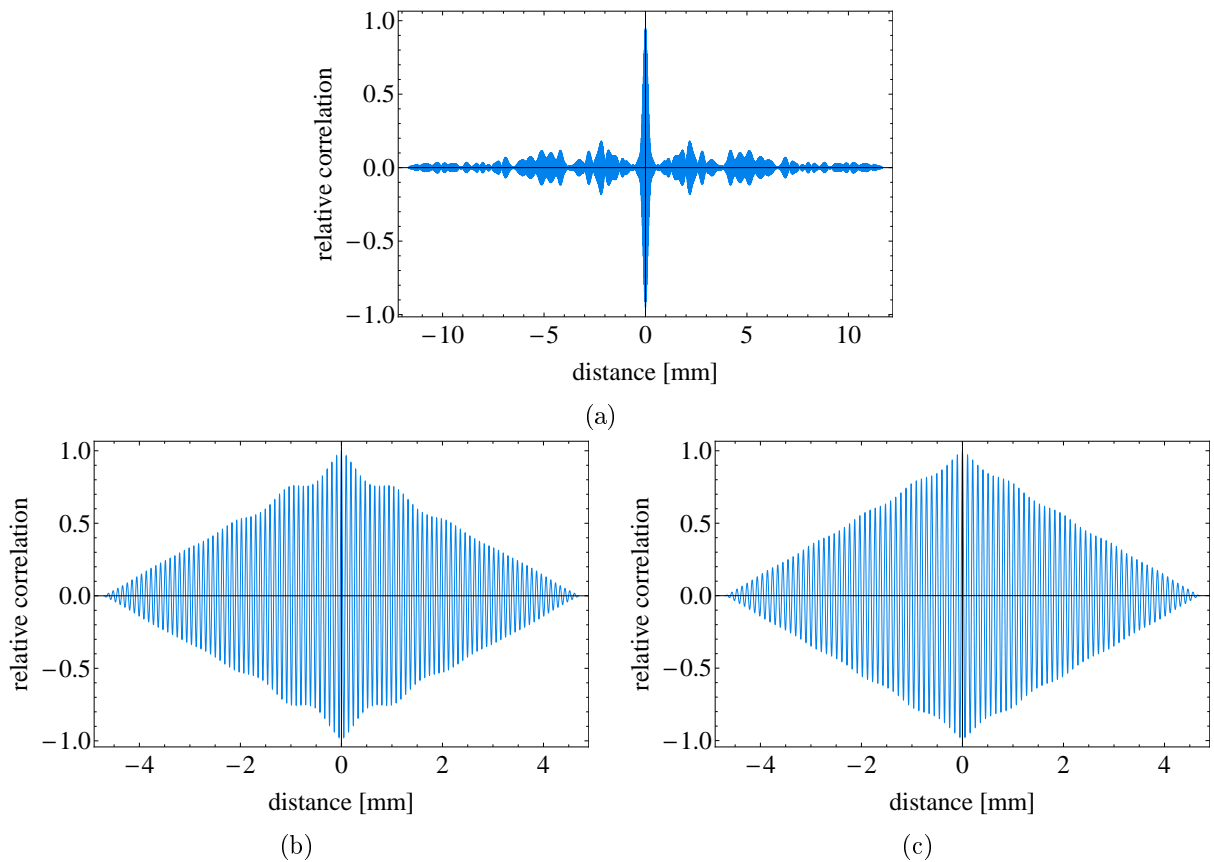
Figure 3.25: Mean ACF of (a) calibration speciment $R_a = 0.42$µm, (b) calibration specimen $R_a = 2.95$µm, (c) calibration specimen $R_a = 3$µm

Analysis of a surface profile taken with a Stylus Instrument

From the test with the calibration specimen it was concluded to proceed as follows for the analysis of the surface profiles taken from the scatterers used in the experiment:

First the raw profiles taken from one scatterer were corrected for a possible inclination by fitting a straight line to the profiles and subtracting it. The resulting profiles were then filtered for long wavelength parts and the short wavelength correction was applied. From the resulting filtered profiles, mean values and standard deviations of the parameters R_a, R_q and R_y were then calculated. Furthermore the APDFs were analysed for their skewness and kurtosis and the mean values and the standard deviations are stated as well. In a next step the autocorrelation function for every profile was calculated and the mean correlation length and its standard deviation is stated. For illustration purposes also the mean autocorrelation function is shown. Finally the linear spectrum for every profile taken from one scatterer was calculated using the Hanning window and the resulting spectra were averaged over. The mean spectrum is shown and the mean frequency was calculated. The results are presented in subsection 3.2.4.

3.2.3 Measurement of Rough Surfaces Using SEM

A scanning electron microscope uses a focused electron beam to investigate a sample and is therefore a non-contact method for measureing rough surfaces. The electrons produced are focused by magnetic lenses and directed towards the sample. When hitting the sample, the electrons interact with the atoms of the sample producing different interaction products as shown in figure 3.26. When investigating the surface of a sample, usually, and as well in our case, the secondary electrons - the electrons emitted by the atoms, exited by the electron beam - are used. To obtain a decent number of secondary electrons, the energy barrier for leaving the material has to be low and hence the surface has to be electrically conductive. Therefore only the Ni coated scatterers, as used in the experiment, were measured using SEM.

To investigate the surface, the scanning electron microscope scans the surface in a raster scan pattern. The number of secondary electrons emitted is proportional to the tilt between the electron beam and the surface and so an image of the surface is created by recording the electron intensity as a function of position. The correspondence between this intensity image and the true geometric surface is, however, not simply one to one and also shadowing presents a problem. To really gain a surface profile stereoscopic viewing needs to be used. For stereoscopic viewing several intensity pictures (in our case three) of a surface are taken, where for every measurement the surface is tilted slightly. The resulting images are the combined to obtain a very accurate picture of the surface. In figure 3.27 the three raw pictures of one measured surface can be see. However, as Whitehouse [Whi10, p394 ff] states, it is still important to realise, that the electrons are not produced at the surface itself, but within the sample, a few nanometers below the surface.
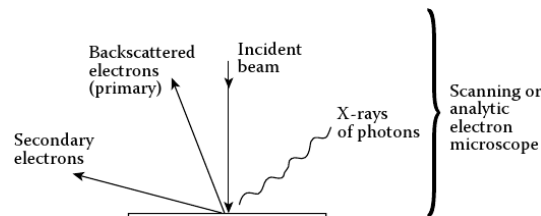

Figure 3.26: Interaction products of electrons with a surface used in scanning electron microscopy. Picture taken from [Whi10, p393, fig. 4.246]

Even tough it is in principle possible to investigate larger samples using SEM, the microscope used is only able to measure relatively small samples. In our case for each sample, prepared with a differently granulated abrasive paste, two pictures, one with a size of around 20×20 µm^2 and a resolution of 0.012µm, and on with a size of 100×100 µm^2 and a resolution of 0.049 µm were obtained. The actual sizes varied due to the stereoscopic combination process.

Analysis of a rough surface measured using SEM

The surface profiles obtained by SEM were first evaluated as a 3D surface. To do so, the APDF of the surface profiles were analysed for their skewness and kurtosis and the roughness parameters R_a, R_q and R_y were calculated.

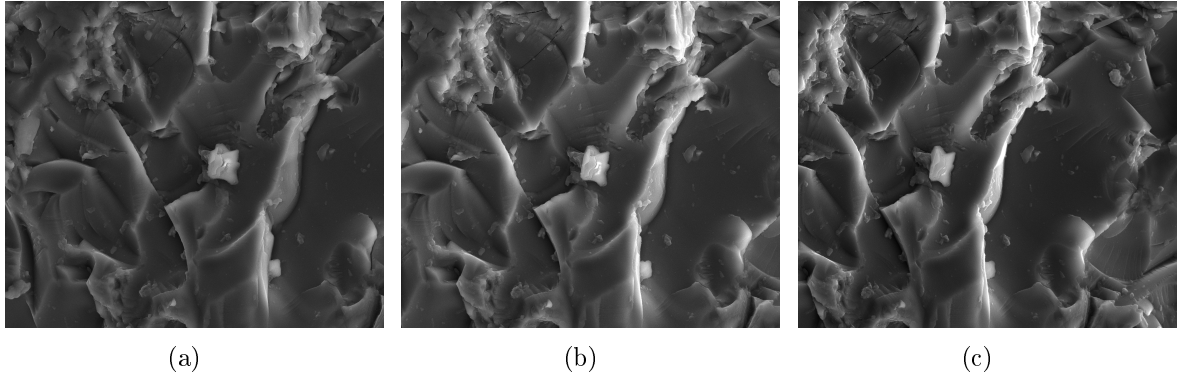<center>(a)   (b)   (c)</center>

Figure 3.27: Raw electron intensity images of a surface. The sample has been tilted for 12 degrees between every measurement.

Furthermore, to be able to compare the measurements taken with the stylus instrument and the measurements obtained by SEM, 10 2D profiles in each direction along equidistant lines were taken from the 3D surface profiles obtained by SEM. The profiles were then corrected for an inclination and the roughness and APDF parameters were calculated. Due to the shortness of the 2D profiles (maximal 100 µm) no corrections for long wavelength parts needed to be applied.

3.2.4 Analysis and Comparison of the Measurements

In the course of this master thesis, the scatterers used in the experiment (granularity 600) were measured using a stylus instrument. To compare these measurements and gain knowledge about the rough surfaces so vital for this experiment, a number of samples have been investigated using SEM. The samples investigated were prepared with an abrasive paste of different granularities of 320, 600, 800 and 1000 as explained in subsection 3.1.3.

Here, first the measurements obtained from the stylus instrument are presented. Afterwards the measurements obtained by SEM are shown and finally the data obtained from the stylus instrument and by SEM performed on samples produced with the same granularity are compared.

Measurements using a Stylus Instrument

Three scatterers used in the experiment were measured prior to their usage: an uncoated scatterer used inside the selector (410), an uncoated scatterer used inside the measurement part (402) and a Ni coated scatterer. For each scatterer several measurements were performed at the sides of the scatterers to avoid destruction of the rough surfaces in the region were most neutrons traverse. For the scatterer 410, five individual measurements were performed. For the scatterer 402, four individual measurements were performed, and for the Ni coated scatterer three measurement were performed. The analysis was performed as described above and a cut-off wavelength of $\lambda_c = 0.8$ mm was used for the long wavelength corrections.

The evaluated parameters can be seen in table 3.7. The parameters of the uncoated scatterers are in good agreement with each other. This confirms the reproducibility of the preparation process. Only the Skewness as well as the Kurtosis are very unstable, as seen by their large standard deviations. The parameters of the Ni coated scatterer differ from the parameters for the uncoated measurements. The differences are thought to be due to the coating. The coating is expected to fill up deep valleys and round off pointed peaks thereby centering the APDF and increasing it's skewness, as reflected by the calculated parameters. However, to really access the influence of the coating more measurements would have to be performed. In figure 3.28 parts of the measured profiles and the combined APDFs of all measurements can be seen. The linear spectra are shown in figure 3.29. They show a decrease in amplitude with increasing frequency until the cut off due to the short wavelength corrections. The mean ACFs are plotted in figure 3.30. The large peak in middle indicates the fast decay of correlation as expected for random surfaces. Futhermore, a first period of negative correlation is visible after the main peak decayed.

Scatterer	glas 410	glas 402	Ni
R_a	0.361 ± 0.012	0.368 ± 0.024	0.387 ± 0.024
R_q	0.475 ± 0.019	0.477 ± 0.034	0.506 ± 0.041
R_y	3.908 ± 0.406	4.021 ± 0.770	5.010 ± 1.346
Skewness	-0.917 ± 0.266	-0.717 ± 0.175	-0.632 ± 0.046
Kurtosis	2.132 ± 1.207	1.513 ± 1.106	2.115 ± 1.632
$\bar{\nu}$ [mm^{-1}]	35.514 ± 1.120	35.070 ± 1.738	34.035 ± 2.278
Correlation length [μm]	6.380 ± 0.378	6.303 ± 0.291	6.586 ± 0.493

Table 3.7: Roughness parameters, parameters of the APDFs, mean wavelengths and correlation lengths of the measured scatterers.
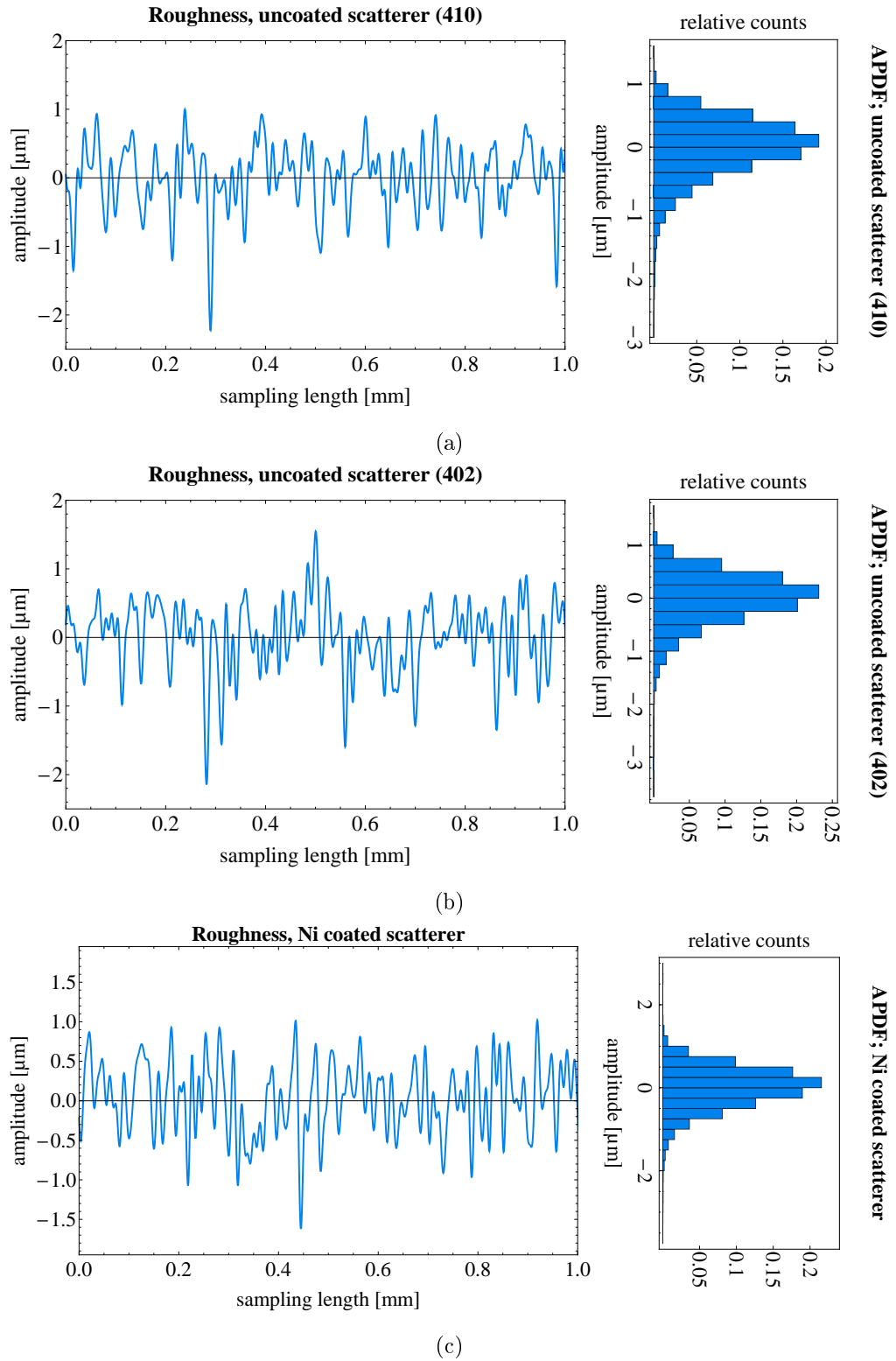
Figure 3.28: Parts of the profiles measured and APDFs of (a) the uncoated scatterer 410, (b) the uncoated scatterer 402 and (c) the Ni coated scatterer. The more centered APDF of the Ni coated scatterer with respect to the APDFs of the uncoated scatterers is clearly visible.

(a)

(b)

(c)

Figure 3.29: Linear Spectra of (a) the uncoated scatterer 410, (b) the uncoated scatterer 402 and (c) the Ni coated scatterer. The fast decay due to the short wavelength corrections is clearly visible around a frequency of 90 mm^{-1}.
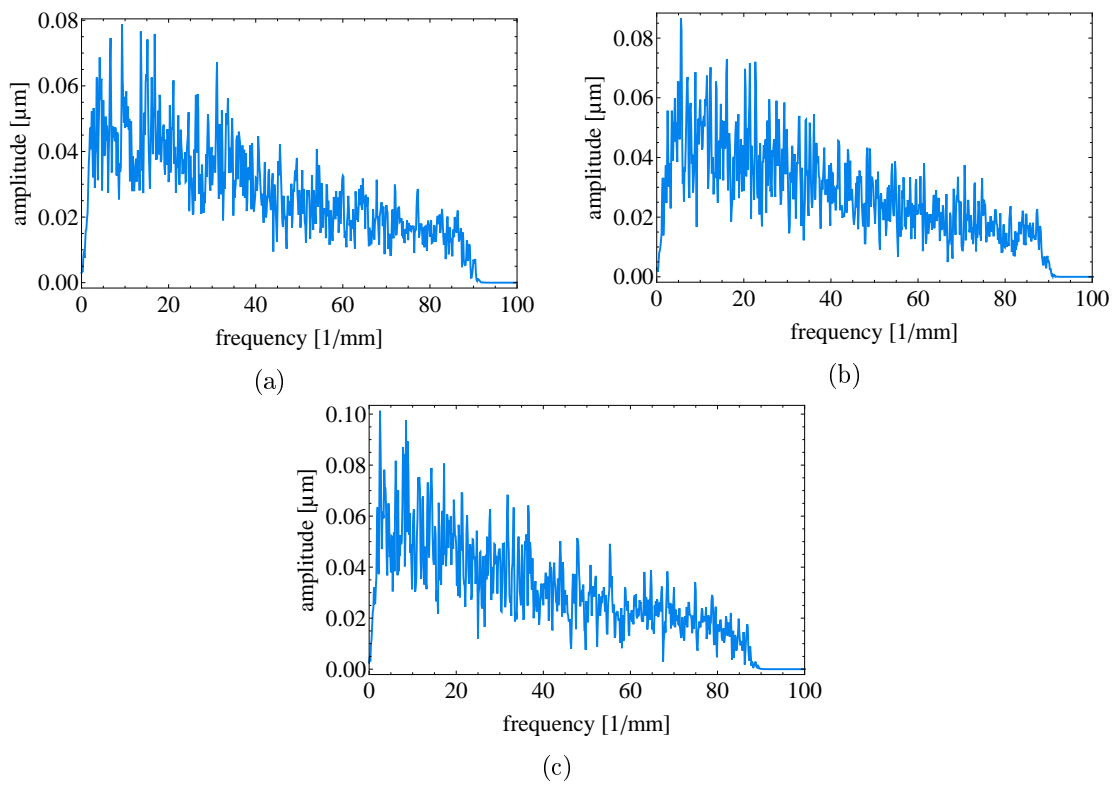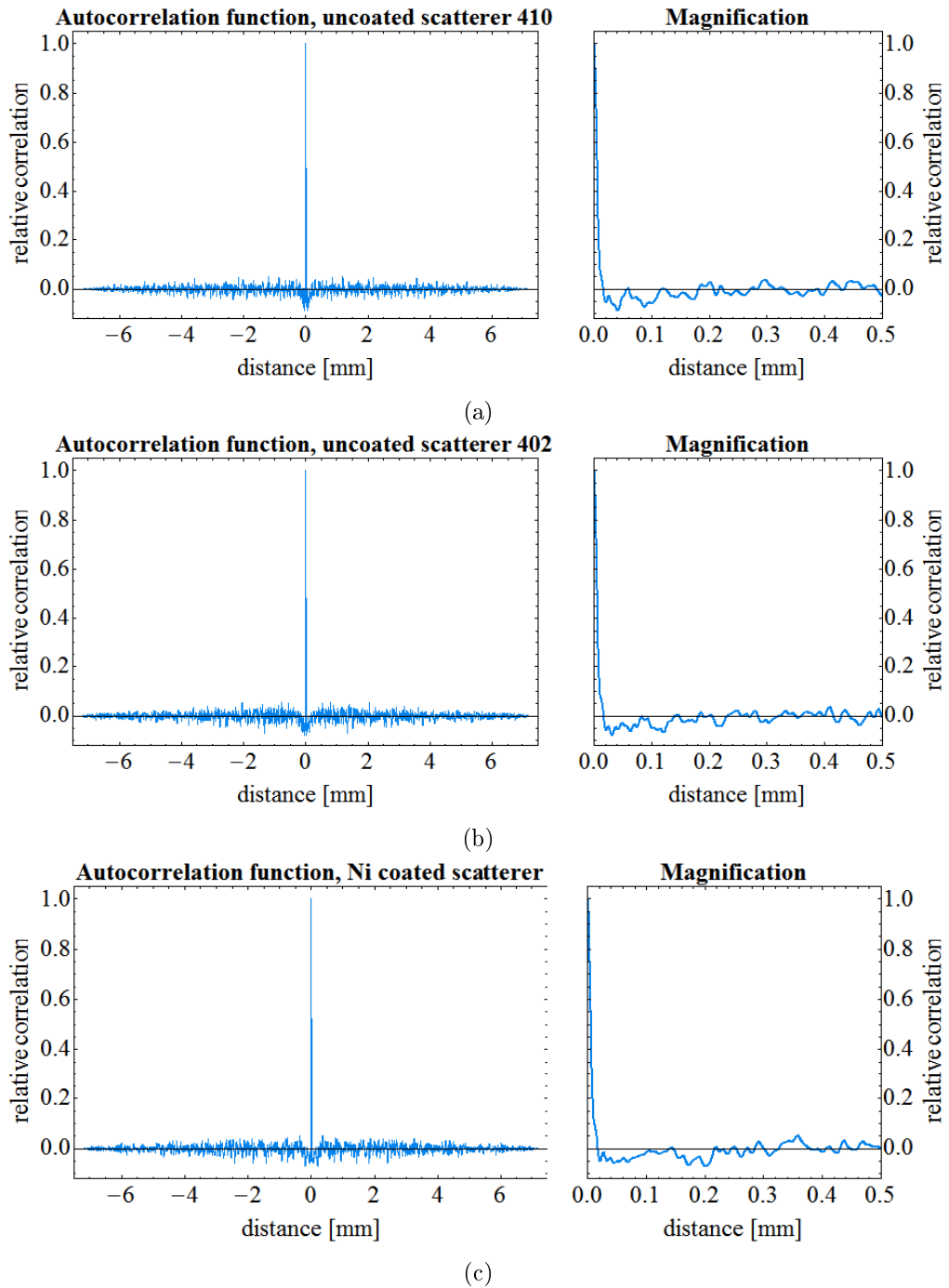
Figure 3.30: ACFs of (a) the uncoated scatterer 410, (b) the uncoated scatterer 402 and (c) the Ni coated scatterer. The expected fast decrease of correlation due to the surfaces' randomness is visible in the fast decay of the main peak.

SEM Measurements

From every sample prepared with an adhesive paste with different granularity, two 3D surface profiles were taken, one with a high resolution of 0.012µm and an area of around 20×20 µm^2 and on with a resolution of 0.04857µm and a size of around 100×100 µm^2. The small high resolution profiles were found to contain a too small area to be statistically significant, since when looking at segments of the same size from the low resolution profiles, all roughness as well as APDF parameters vary significantly. For the larger area measurements the situation is better and their evaluation is presented here. First the parameters calculated from the whole surface profiles are presented and discussed. Afterwards the test for statistical significance is shown.

The calculated parameters for the low resolution surface profiles with different granularities, on basis of the full surface profiles, can be seen in table 3.8. Their APDFs are shown in figure 3.31. The roughness parameters R_a, R_q and R_y show a decrease with increasing granularity. This seems reasonable since it is expected to obtain a "finer" roughness using an abhesive paste with higher granularity. Only the increase in R_a and R_q from granularity 800 to granularit 1000 does not fit the picture. Regarding the APDF parameters the kurtosis seems to follow a trend as well. With increasing granularity, the kurtosis decreases. This can be explained since with smaller grains, single deep valleys are less likely, leading to a more compact and rectangle shaped APDF. The skewness however varies without any trend at all. Especially the change in scewness between the granularit of 320 and the granularity of 600 is not understood.

Scatterer	320	600	800	1000
R_a	1.089	0.510	0.451	0.511
R_q	1.436	0.678	0.608	0.621
R_y	11.790	6.829	5.676	3.998
Skewness	−1.083	0.656	−0.580	−0.061
Kurtosis	2.795	3.021	1.694	−0.533

Table 3.8: Roughness and APDF parameters for the SEM measurements of scatterers with different granularities for the whole surface profiles.

The not understood behavior questions the statistical significance of the surface profiles. To further investigate the surface profiles they have therefore been split into four equally large parts. Every part was then corrected for a possible inclination and their surface parameters were calculated. The mean values and standard deviations for the parameters are stated in table 3.9. The values follow largely follow the same trend as for the parameters obtained from the whole surfaces. This is especially true for the roughness parameters, but they, in part, differ significantly from their counter parts obtained from the whole suraces. The roughness parameters furthermore show relatively small standard deviations and therefore, seem to be reliable. However, the APDF parameters, skewness and kurtosis, show fluctuations even larger than between the single measurements performed with the stylus instrument (table 3.7). They also differ hugely from the ones obtained from the whole surfaces. Here it is therefore concluded, that the surface profiles obtained by SEM are too small and not statistically significant. Nevertheless, below the stylus measurements are compared with the SEM measurements.
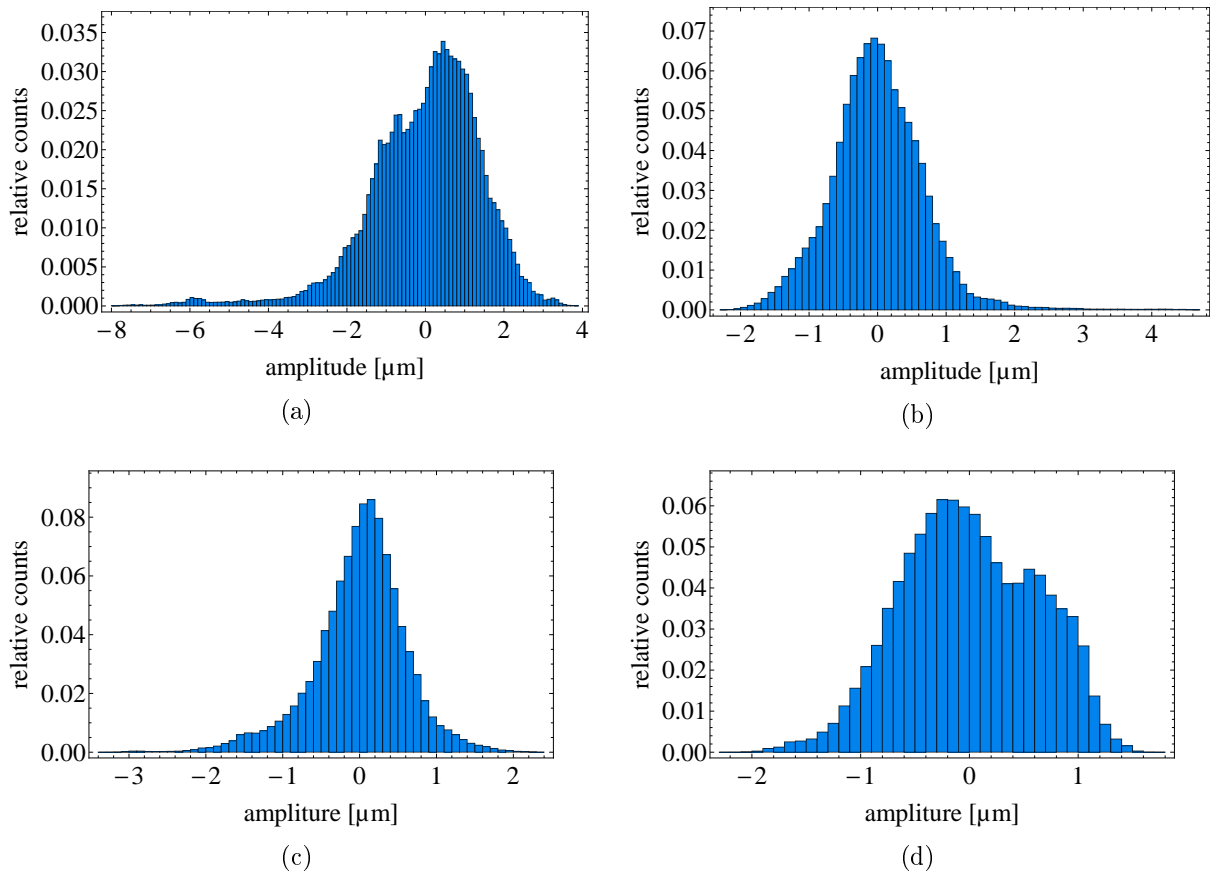
Figure 3.31: APDF of the sample prepared with a granularity of (a) 320, (b) 600,(c) 800 and (d) 1000.

Scatterer	320	600	800	1000
R_a	1.000 ± 0.236	0.501 ± 0.029	0.427 ± 0.055	0.455 ± 0.039
R_q	1.263 ± 0.285	0.651 ± 0.065	0.554 ± 0.083	0.557 ± 0.034
R_y	7.628 ± 1.282	5.057 ± 0.967	3.836 ± 0.722	3.558 ± 0.331
Skewness	-0.428 ± 0.281	0.472 ± 0.647	-0.335 ± 0.508	-0.315 ± 0.180
Kurtosis	0.315 ± 0.747	1.349 ± 2.297	0.619 ± 1.111	-0.236 ± 0.638

Table 3.9: Roughness and APDF parameters of the split SEM surface profiles.

Comparison

To compare the measurements of the Ni coated scatterers with granularity 600, performed with the Stylus instrument and using SEM, the 3D surface profile was converted to 2D profiles as described above. The fact, that the SEM measurements are more accurate can be seen in figure 3.32, where a circle with a radius of 2µm representing the stylus tip is shown on a 2D profile obtained from the SEM measurements. It is clearly visible, that the tip cannot follow the profile recorded by SEM.
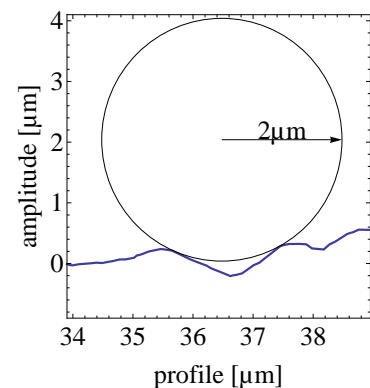
The calculated parameters for the SEM measurements can be seen in table 3.10 and the combined APDF of the 2D profiles is shown in figure 3.33a. In comparison with the APDF obtained from the stylus measurements (figure 3.28c) the different skewness is clearly visible. This can be interpreted as due to the

Figure 3.32: "Stylus tip" on surface measured using SEM

finite tip size of the stylus, since the APDF of the stylus measurements is shifted towards positive values (see figure 3.14). This argument is also supported by the comparison of the roughness values and the correlation length. R_a, R_q as well as R_y are smaller for the stylus measurements then for the SEM measurements and the correlation length is larger for the stylus measurements than for the SEM measurements. This trend has also been seen by Poon and Bhushan [PB95], as mentioned above (subsection 3.2.2). In addition, a positive skewness of the APDF resulting from our production process seems more reasonable, since it seems likely that some grains pressed into a flat surface leave comparatively large valleys and sharp peaks in between.

It has furthermore been checked, that the difference in the roughness parameters and the APDF is not due to the different sampling intervals. To show that the SEM measurements were reduced until reaching a sampling interval of 0.389µm, that is in the region of the sampling interval of 0.5µm of the stylus measurements, by repeatedly dropping every second measurement point. The resulting APDF only differed slightly from the original one and also the roughness parameters changed not significantly.

The mean ACF calculated from the 20 2D profiles in comparison with the mean ACF of
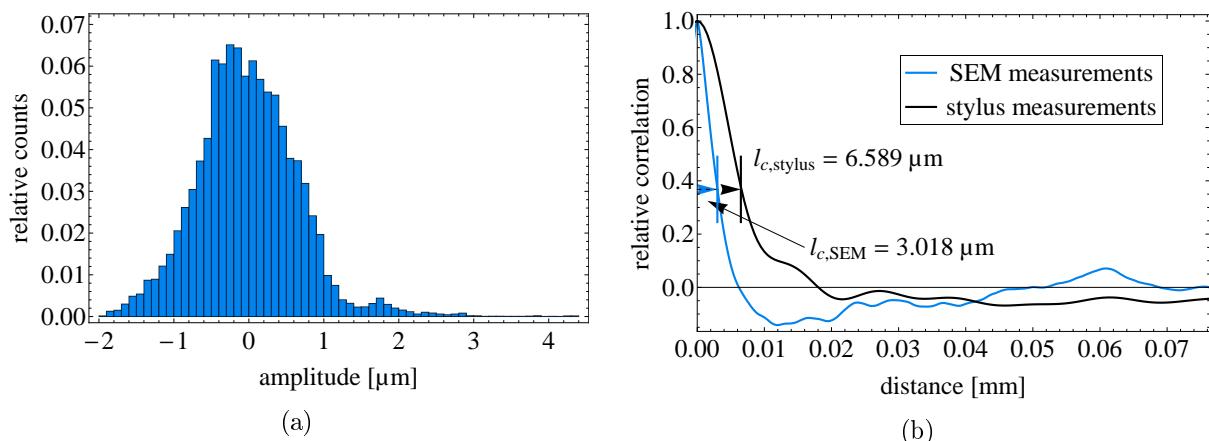
Figure 3.33: (a) combined APDF of the 2D profiles from the SEM measurements of the scatterer with granularity 600 and (b) mean ACF of the 2D profiles from the SEM measurements of the scatterer with granularity 600 and the stylus measurements. The correlation lengths (l_c) are stated in the plot.

the stylus measurements can be seen in figure 3.33b where also the values for the correlation lengths are stated. Due to the different measurement lengths the ACF of the SEM measurements is of course shorter than the ACF of the stylus measurements and only the part where both ACF exist is shown. The larger correlation length of the stylus measurements is clearly visible.

R_a	0.480 ± 0.104
R_q	0.604 ± 0.143
R_y	2.949 ± 0.774
Skewness	0.211 ± 0.573
Kurtosis	0.136 ± 1.173
Correlation length	3.272 ± 0.824

Table 3.10: Roughness and APDF parameters for the SEM measurement of the scatterer with granularity 600 evaluated as 2D profiles.

The mean linear spectrum of the 2D profiles taken from the SEM measurements was calculated as well. It is shown in figure 3.34a. Due to the different length and sampling frequencies of the 2D SEM profiles and the stylus measurements, the frequency resolutions of the spectra are different and hence the spectra cannot be compared directly. The frequency resolution of the spectrum obtained from stylus measurements is 0.139 mm^{-1} and 13.097 mm^{-1} for the 2D SEM profiles. To obtain a spectrum from the SEM measurements with a frequency resolution about the same as the resolution of the stylus instrument spectrum, 50 2D profiles in each direction were taken from the SEM measurements. The profiles were each corrected for an inclination and the corrected profiles were then combined to form one longer profile. The linear spectrum of this profiles was then calculated. It shows a frequency resolution of 0.131 mm^{-1}, so about the same as spectrum from the stylus measurements. The spectrum is plotted against the spectrum of one stylus measurement in figure 3.34b. Both spectra show the same

magnitude in their amplitudes. The low long wavelength region of the SEM spectrum is due to the corrections for inclination of every 2D profile and the assembling to one large profile. The visible peaks are also thought to be artifact from the assembling process, since the taken profiles are very close to each other and therefore will not vary much. The spectrum obtained from the 50 2D profiles from the SEM measurements is therefore not thought to be reliable, but the fact, that the two spectra are in the same magnitude is positive for the evaluation process.
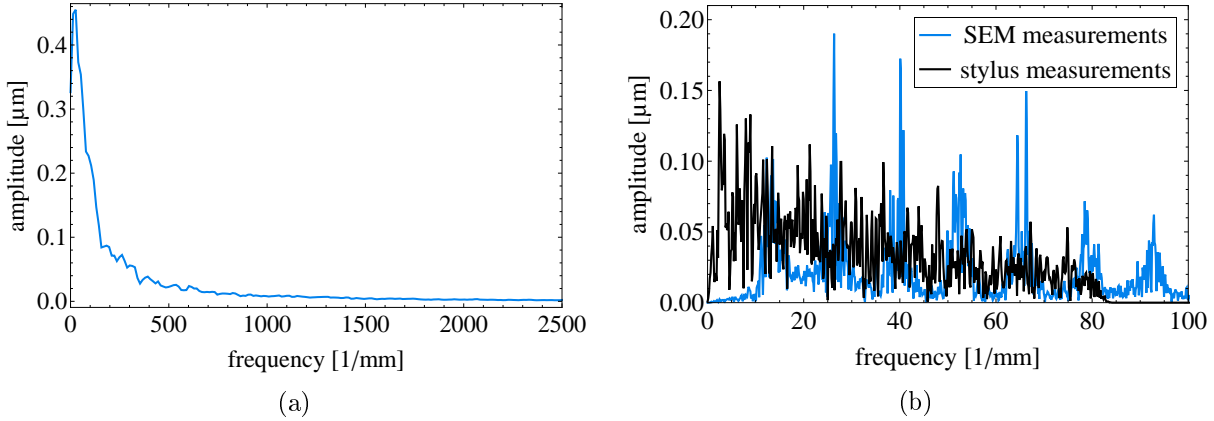

(a)   (b)

Figure 3.34: (a) Mean linear spectrum of the 20 2D profiles taken from the SEM measurements and (b) comparison of the linear spectra from 50 combined 2D profiles taken from the SEM measurements and from one stylus measurement

3.2.5 Conclusion

It is concluded that the comparison between the measurements performed with the stylus instrument and the measurements obtained by SEM showed the influence of the stylus tip on the measured roughness. The found distortions were in agreement with the ones published by the authors cited. The obtained information could therefore in principle be used to derive corrections for the stylus measurements. However the question about the statistical significance of the SEM measurements demands further investigation and it has therefore been decided to derive the corrections for the slit height due to the roughness from the stylus measurements as has been done by the qBounce team in the past (see subsection 3.3.3).

To further improve the knowledge about the scatterers used, most importantly, the measurement area should be enlarged with respect to the performed SEM measurements. This can in principle be done using SEM, but also an atomic force microscope (AFM) can be used. AFM measurements would additionally have the advantage, that they don't need an electrically conductive surface and so also the uncoated scatterers could be measured to investigate the changes due to the coating process.

3.3 Systematic Effects

The experimental setup presented contains three main possible sources of systematic uncertainties:

- A possible step in height between the lower mirror of the selector and the lower mirror of the measurement part presents a possible source of uncertainty since the two parts of the experimental setup are completely separated from each other.

- The gap between the two parts of the setup represents a source of systematic uncertainty and is inevitable since the lower mirror of the selector has to be changed in height to reduce the step between the lower mirrors of the two parts.

- The slit height is a source of error due to several aspects as discussed below.

These three sources of errors are discussed individually below. For each of them, first the evaluation process is explained and the resulting uncertainties are stated. Their possible influences on the measured transmission are discussed thereafter.

3.3.1 A Possible Step Between the Setup's Parts

Since the experimental setup consists of two completely separated parts, a step between the two lower mirrors had to be controlled. For this purpose, after installing the lower mirror of the measurement part two linear gage laser hologages were placed on each side, on top of one of the lower mirrors. The step was then measured by sliding the linear gages from one mirror to the other, recording the height changes shown by the linear gages. This procedure is possible since both, the granite plate holding the experimental setup and the granite pedestal on which the hologages are mounted offer a very high degree of flatness (better 0.7 µm). The recorded height change can therefore be accounted to the misalignment of the two mirrors. Using the nanopositioning stage of the selector, the two mirrors were then aligned to each other until the step was small enough within measurement resolution. The resulting values for the step were combined for a value for the step height at the center (z_{step}) and an uncertainty was evaluated (Δz_{step}) as well.

The individual results for every measurement series will be presented later when discussing the quantum transport measurements (see section 4.3).However, for all measurement the step was in range of $-0.34 \leq z_{step} \leq 0.35$ µm, where a negative value indicates a step down from the selector to the measurement part.

For the estimation of the step's systematic influence, the upper mirror/scatterer used in the measurement part is ommitted.

The situation for a step down from the selector to the measurement part is shown in figure 3.35. The gravitational states before and after the step are shifted against each other since the lower boundary condition (the neutron mirror) is shifted. This means a change of basis at the step, where $\psi_i(z)$ is the wave function of the ith gravitational state before the step and $\phi_i(z)$ is the ith gravitational state after the step. Let the neutron before the step be in the ith
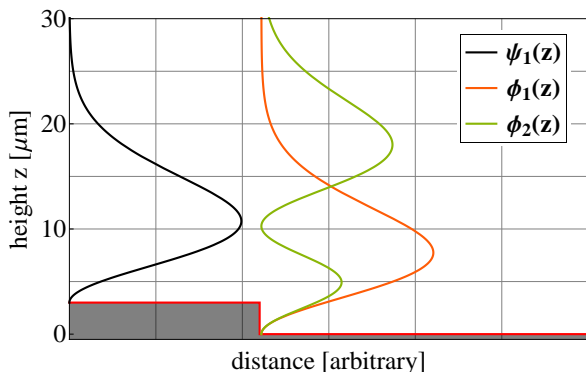
Figure 3.35: First gravitational state before the step (ψ_1) and first and second gravitaional state after the step (ϕ_1 and ϕ_2).

Table 3.11: Transition probabilities P_{ij} for the first and second gravitational state before the step (ψ_1 and ψ_2) to the first four gravitational states after the step (ϕ_1 to ϕ_4).

	ψ_1	ψ_2
ϕ_1	0.978	0.008
ϕ_2	0.011	0.962
ϕ_3	0.003	0.017
ϕ_4	0.002	0.004

gravitational state $\psi_i(z)$. After the step it will be in a gravitational state of the new basis and the probability of being in state $\phi_j(z)$ is given by the overlap of the two wave functions:

$$P_{ij} = |\int \psi_i(z)\phi_j(z)dz|^2 \tag{3.16}$$

For a step of one micrometer the probabilities for a neutron in the first state before the step, to be in the jth state after the step are shown in table 3.11. The transition probabilities into different gravitational states while traversing the step are very small and hence the occupation of states before and after the step can be assumed to be identical.

Furthermore, reflection will occur at the step. This can be calculated following [RSS09, p10 ff]. For a step of one micrometer reflexion is negligible.

A step up from the selector to the measurement part will lead to a loss in transmission. This is due to the fact that neutrons bumping into the front of the measurement part's lower mirror will be reflected or absorbed, since the mirror itself represents a high energy barrier for them. To estimate the influence of a step up on transmission, the probability of presence for neutrons in region of the step's height above the neutron mirror has to be calculated (see figure 3.36). For the first state the probability of presence in a region of 1 µm above the mirror's surface is 0.16 %. This is also the percentage of neutrons in the first state being reflected or absorbed due to the step. For higher states this number decreases. The average probability of presence in a region of 1 µm above the mirror for the first 50 states is 0.14 %. It can therefore be concluded, that the loss in transmission due to a step of 1 µm, or below as evaluated during experimental time, is negligible.
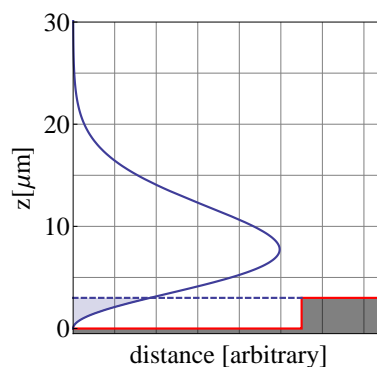

Figure 3.36: Overlap of neutron's probability of presence in ground state above the mirror with a step of 3 µm.

However, since lower states are effected more, a step will change the state distribution entering the measurement part. Furthermore, one should also keep in mind, that a step not only leads to a loss in transmission, but also interaction phenomena such as interference between reflected and incoming neutrons may occur. These effects are, however, not considered here.

3.3.2 A Possible Gap Between the Setup's Parts

Besides a possible step between the two parts of the setup, also the gap between them had to be controlled. For this cause brass spacers of different sizes were used. When adjusting the setup, the slit was evaluated by sliding spacers with increasing thickness between the two lower mirrors. The slit was concluded to be larger than the thickness of the last spacer that was fitting between the two mirrors and smaller than the first spacer that did not fit. The gap has been evaluated to be between 30 and 150 µm for all measurement series. The values for every measurement series are stated in section 4.3, in the subsections corresponding to the individual measurement series.

To estimate the loss in transmission due to the gap, the traverse of neutrons through the selector is considered classically. A classical neutron traverses the selector on a hopping trajectory as illustrated in figure 3.37a. The distance between two points of contact with the lower mirror is given by:

$$2 \cdot v_x \sqrt{2 \cdot h \cdot g} \tag{3.17}$$

and depends on the horizontal velocity v_x , the hopping height h and the Earth's gravitational acceleration g. For a hopping height of 200 µm and a vertical velocity of $v_x = 3$ m/s, the distance between two points of contact is 38.31 mm. The situation at the gap is illustrated in figure 3.37, where the trajectories over the gap for two neutrons with the same hopping height of 10 µm is shown. The two neutrons' trajectories are shifted towards each other and have a contact point with the mirror exactly before, or after the gap, respectively. Assuming that the contact points for neutrons with a given hopping height are evenly spread out over the mirror, the loss in transmission due to the gap can be estimated by dividing the distance between two points of contact on a hopping trajectory by the width of the gap. The loss in transmission due to a gap of 100 µm for neutrons with a hopping height of 200 µm and $v_x = 3$ m/s then becomes $3.7 \cdot 10^{-3}$. For a neutron with a hopping height of 20 µm the loss of transmission in the same situation is $8.3 \cdot 10^{-3}$. An estimation for neutrons with different hopping heights between 15 and 200 µm and vertical velocities between 3 and 6m/s leads to a mean loss of $2.7 \cdot 10^{-3}$ for a 100 µm gap. For a 200 µm gap the value changes to $5.4 \cdot 10^{-3}$. Between the gap width and the neutron loss therefore, exists a linear dependency and neutrons with a lower hopping height and a smaller vertical velocity are more likely to be removed from the system. For the evaluated values of the gap between 30 and 150 µm, therefore a negligible loss in overall transmission between 0.13 and 0.54 % is expected.
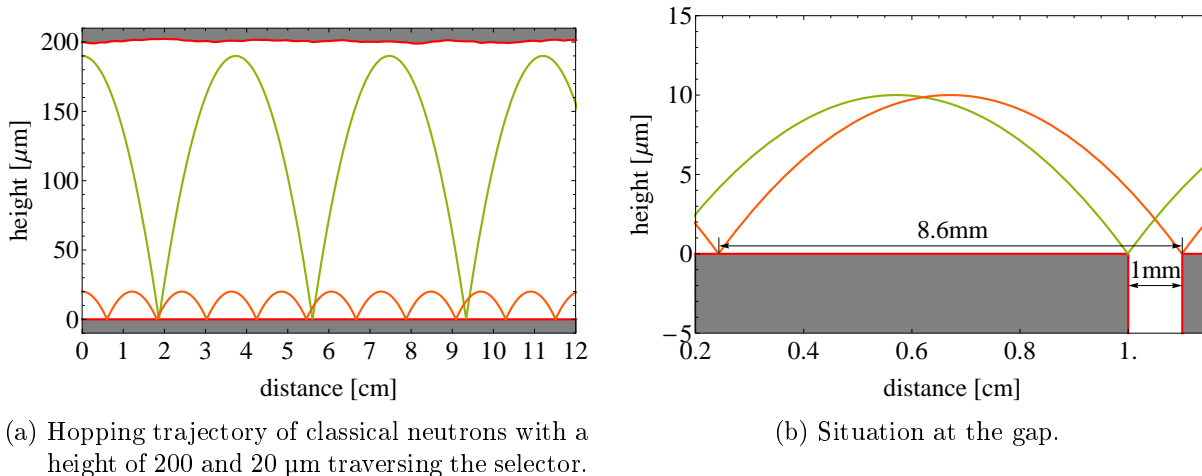
(a) Hopping trajectory of classical neutrons with a height of 200 and 20 µm traversing the selector.

(b) Situation at the gap.

Figure 3.37: Movement of a classical neutron over the gap for two neutrons with a hopping height of 10 µm.

3.3.3 The Slit Height

In this section the final evaluation of the slit height is presented. There are three sources of error regarding the slit height:

- a possible drift of the coarse adjustment device

- an instability of the nanopositioning stage

- the installation process of the upper mirror / scatterer (including the roughness)

Here, first the drift measurements of the coarse adjustment device are presented. Afterwards the stability of the nanopositioning stage is investigated. After that the installation process of the upper mirror / scatterer is presented and the influence of the scatterer's roughness on the evaluation of the slit height is discussed. The composition of the final slit height values are presented at last.

Drift Measurements

The position of the measurement part's upper mirror is held in place by the coarse adjustment device, consisting of an aluminum plate resting on rubber cylinders working as countering springs (see subsection 3.1.1). Since these rubber parts react under pressure with time the stability of this system had to be ensured. The experimental setup does not include any tool to monitor the coarse adjustment devices drift during measurement. Therefore, to be able to estimate the drift and the error on the slit width, drift measurements were performed prior to the experimental time. For this purpose the coarse adjustment device was first adjusted to its designated position with a slit of around 1mm between the setups ground plate and the coarse adjustment aluminum plate. The system was then loaded with different weights and three linear gage laser hologages were placed on top of the aluminum plate. After a certain amount of time the coarse adjustment device was readjusted, meaning that the slit width was varied and the measurement was repeated. This was done to obtain knowledge about the devices

reaction to small changes, as done when changing the setup (the upper mirrors or scatterers respectively) later in the actual experiment.

First, a measurement with three rubber springs, which were unstressed prior to the measurement, without any load was performed. The result seen in figure 3.38 shows a maximum drift of -2.8µm for one linear gage over a time of more than 12 hours. The mean absolute drift of the three linear gages after 10 hours is (1.7 ± 0.06) µm. It is clearly visible, that the drift gets slower with time but did not plateau for this measurement. To further decrease the setups drift it was decided to use six instead of three rubber springs.
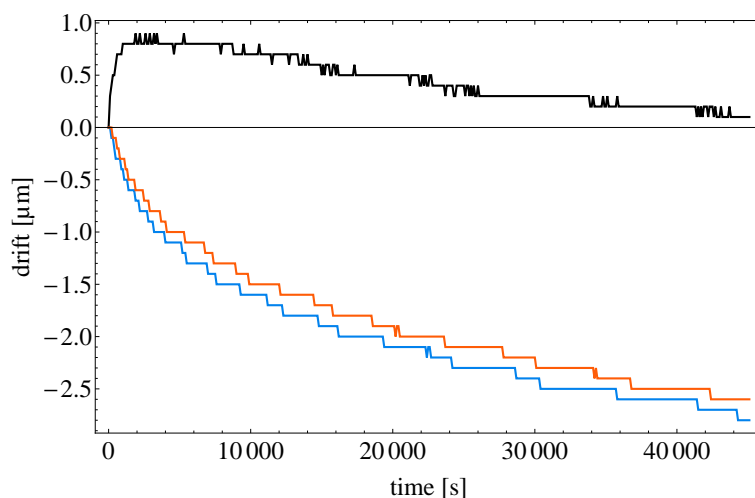

Figure 3.38: Drift measurement of the unloaded system which has been unstressed before. The three lines correspond to the three linear gages used.

As a next step, drift measurements with a load were performed using six rubber springs. The actual load on the coarse adjustment device in the experiment was estimated to around 4.25 kg consisting of 1.2 kg accounting for the aluminum plates and the system to hold the upper mirror, 1.65 kg for the mirror itself consisting of BK-7 glass with a density of 2.51 g/cm^3 and a volume of ($15 \times 15 \times 3$) cm^3, and around 1.4 kg for the nanopositioning stage. The measurements were performed with a load of around 3.95 kg.

After loading the system, the device was again adjusted to a position with a slit of around 1 mm between the setups ground plate and the coarse adjustment aluminum plate and a drift measurement was started to see the devices response when unstressed before. The results can be seen in figure 3.39. In comparison with the unloaded system the mean drift of the three linear gages after 10 hours decreased slightly to (1.43 ± 0.06) µm. Furthermore the drift seems to have decreased faster with time compared to the unloaded system.

The maximum drift as well as the drift time depend on the height change of the coarse adjustment device. Therefore several measurements with different height changes were performed. This approach is also valid since between changing the mirrors, or scatterers respectively, resting on the coarse adjustment device, the system was never completely unstressed but only
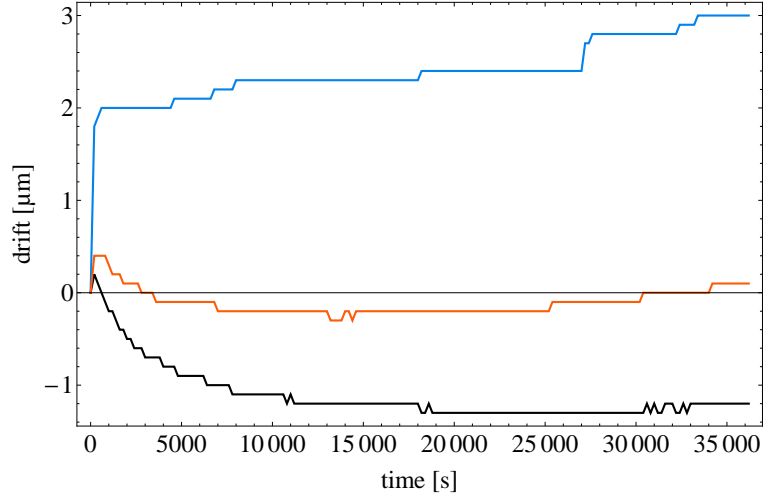
Figure 3.39: Drift measurement of the system loaded with 3.95 kg, which has been unstressed before. The three lines correspond to the three linear gages used.

changed slightly. The measurements were done for height changes of -200, -100, 100 and 200 µm were the negative sign corresponds to a height change down, meaning that the coarse adjustment device was further stressed. The results have been fitted to a model including a relaxation time τ and a maximal drift d_{max}:

$$D(t, \tau, d_{max}) = d_{max}(1 - e^{-\frac{t}{\tau}}) \tag{3.18}$$

An example of a measurement and the resulting fit, for a height change of 200 µm can be seen in figure 3.40. For this measurement the mean drift time and mean maximum drift of the three linear gages are $\tau = (1396.28 \pm 4.68)$ s and $d_{max} = (0.6543 \pm 0.0002)$ µm. It is also visible, that for only small height changes the drift time decreases. For this measurement the drift plateaued after around 3.5 h.

The resulting maximal drifts and drift times of the performed measurements were then further analysed. Both parameters were fitted to straight lines depending on the height change. The results can be seen in figure 3.41. The resulting fits are in good agreement with the measurements.

For the drift times the fit model is:

$$\tau(x) = a \cdot x + d \tag{3.19}$$

The resulting parameters are $a = $ (-7.18 $\pm$ 0.06) and $d = $ (3002.4 $\pm$ 10.3). The results predict a τ of (1566.89 $\pm$ 22.41) seconds for a height change of 200 µm . This means that after (1566.89 $\pm$ 22.41) seconds 63.2 % of the maximal drift occurred. For the experimentalist this means that after changing the upper mirror, waiting a time of τ seconds decreases the error on the slit width for 63.2 %.

For the maximal drift the same fit model was used. The resulting parameters are $a = $ (42.0 $\pm$ 0.022)$\cdot10^{-6}$ and $d = $ (140.0 $\pm$ 3.4)$\cdot10^{-4}$.
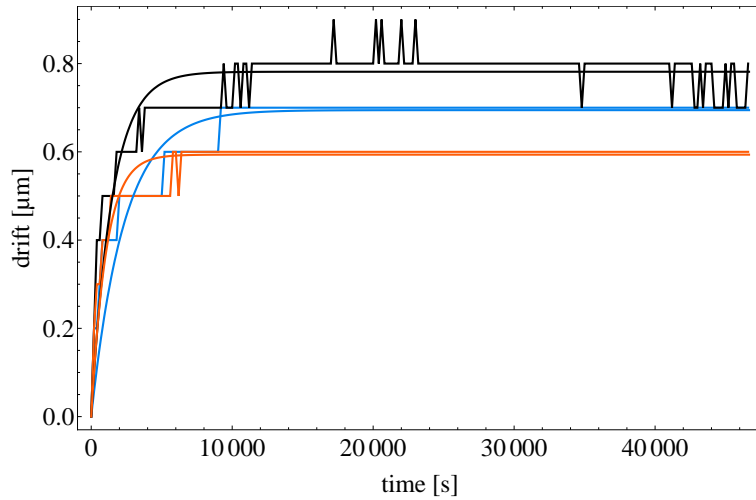
Figure 3.40: Drift measurement of the system loaded with 3.95 kg. The system has been tensed before and a change in height of 200 μm was induced prior to the measurement. The three lines correspond to the three linear gages used.

For future experiments this model can be used to estimate the drift of the coarse adjustment device and thereby the uncertainty of the slit width of the measurement part depending on the height changes done during changing the upper mirrors. For the transport measurements presented in this thesis, however, these results were not available prior to the experiment and neither the height changes not the waiting times between adjusting the upper mirrors with the coarse adjustment device and the measurements have been sufficiently recorded. We are however certain, that the height change when changing the mirrors did not exceed 250 μm and the time between employing the coarse adjustment device and starting the transport measurements did not exceed a few minutes. Therefore, a conservative value of $\Delta z_{drift} = 1$ μm for the uncertainty of the slit width for every measurement series due to the systems drift seems reasonable. Furthermore it was assumed, that the drift affects the slit height evenly, not introducing any tilt.
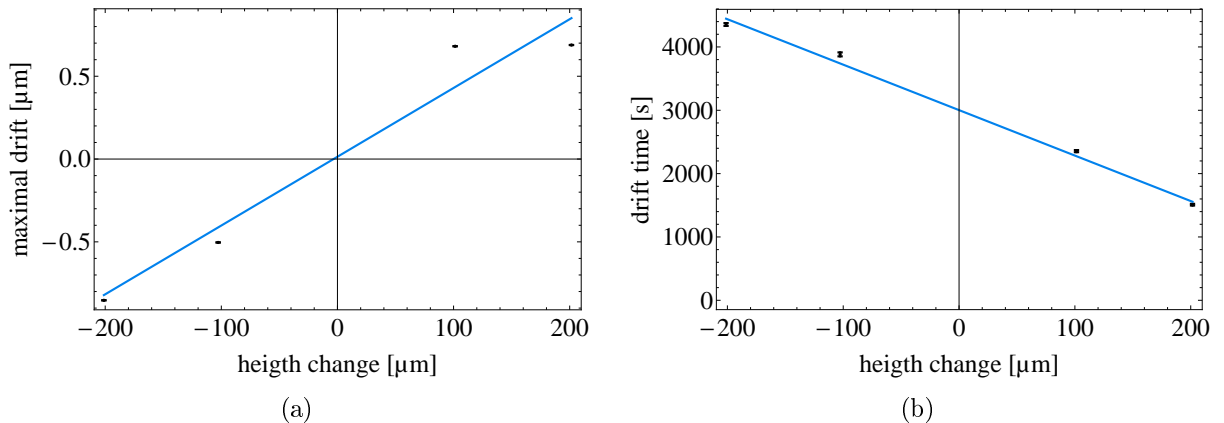

(a)

(b)

Figure 3.41: Straight line fit to (a) maximal drifts and (b) drift times, depending on the height change.

Stability of the Nanopositioning Stage in Open- and Closed-Loop Mode

The stability of the slit height is influenced not only by the drift of the coarse adjustment device, but also by the stability of the nanopositioning stage. The nanopositioning stage is driven by piezo elements. These elements also drift over time, changing the nanopositioning stage's position. To control this drift, the stage is equipped with capacitive sensors. While driven in closed-loop mode the nanopositioning stage is extremely stable since the position is adjusted automatically according to the internal sensors. In figure 3.42 the nanopositioning stage's fluctuations in position over time, when set to a position of 200 µm and the corresponding distribution are shown. The stability is reflected in the narrow distribution with a standard deviation of only 0.032 µm.
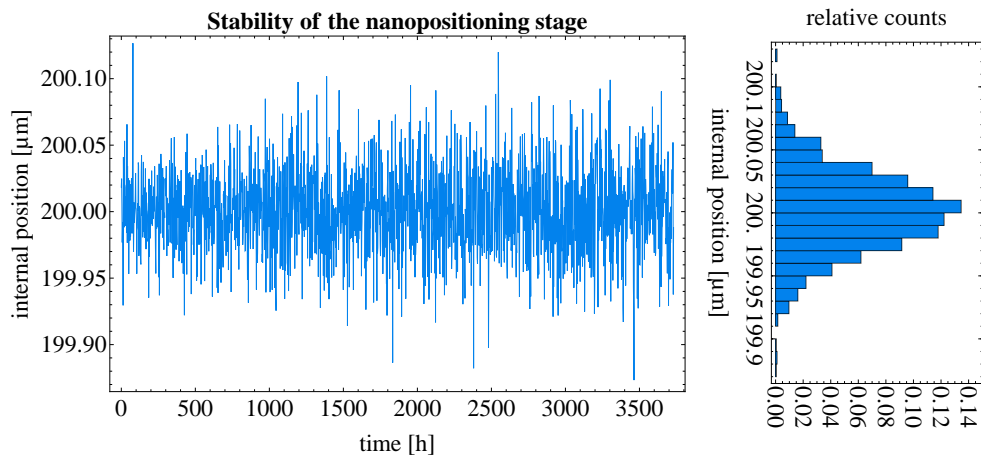

Figure 3.42: Variation of the nanopositioning stages position in closed-loop mode over time (left) and distribution as histogram (right), recorded by the stages internal sensors.

In some cases, however, instabilities as seen in figure 3.43 occurred. In these cases the stage's position changed for a short time for several micrometers. Since this changes occurred for a very short time they are not thought to change the measurement outcome drastically and no special treatment during evaluation was applied.
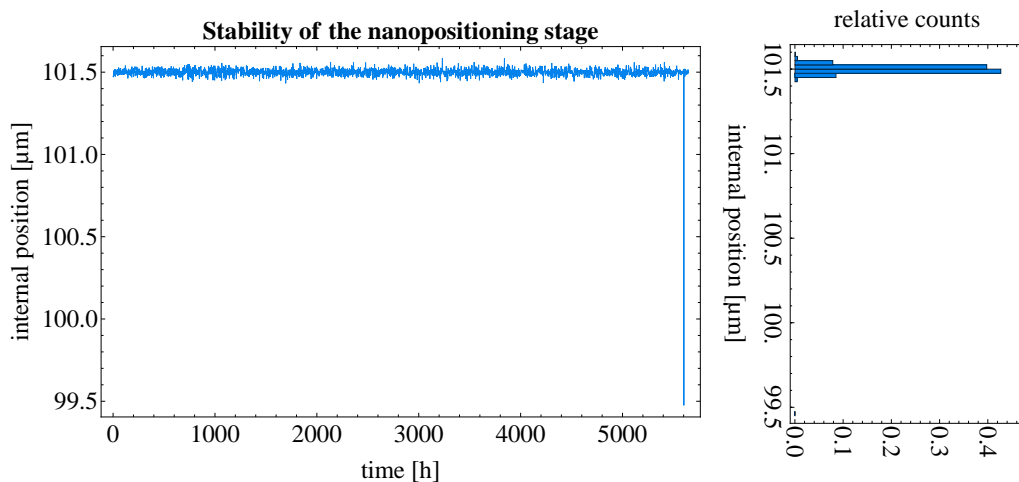

Figure 3.43: Variation of the nanopositioning stages position in closed-loop mode over time (left) and histogram (right), recorded by the stages internal sensor.

Since the maximum range of the nanopositioning stage when driven in closed-loop is restricted (in our case 200µm) we also performed measurements in open-loop mode to increase the measurement range. In open-loop mode the stage's position is still monitored by the internal sensors but the adjustment has to be done by hand. A graph of the nanopositioning stage's position over time, when driven in open-loop mode, is shown in figure 3.44.
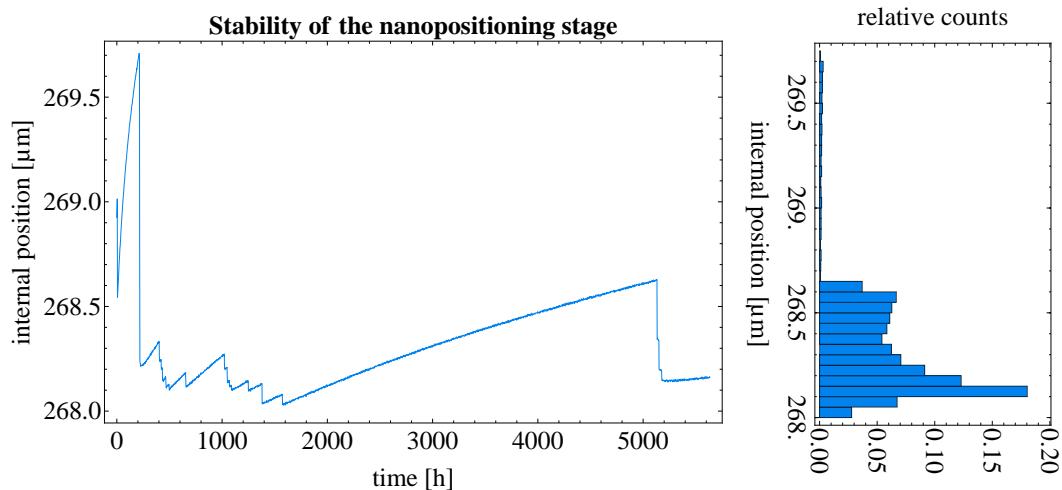

Figure 3.44: Variation of the nanopositioning stages position in open-loop mode over time (left) and histogram (right), recorded by the stages internal sensor.

For the data analysis the recorded position for every measurement has been evaluated. The mean value was taken as actual position (z_{nano}) and the uncertainty (Δz_{nano}) is the deviation from the mean value within which 68 % of the recorded values lie. The calculated values for the three presented measurements can be seen in table 3.12. For the closed-loop mode the calculated uncertainties are small compared to the open-loop mode.

mode	mean [µm]	error [µm]
closed-loop	200.001	0.03
closed-loop	101.499	0.018
open-loop	268.325	0.205

Table 3.12: Mean values and errors of the nanopositioning tables position

Installation Process of the Upper Mirror / Scatterer

The installation process of an upper mirror or a scatterer above a flat lower mirror is explained in the following. For the measurement part, flat mirrors as well as scatterers were installed above the lower flat mirror. In case of a flat mirror, brass spacers with a nominal height of 30µm were used to adjust the upper mirror parallel above the lower mirror. The spacers were used to avoid the two mirrors of getting in direct contact with each other, since it would have been impossible to separate them again, due to adhesion effects. The spacers were placed on top of the lower mirror and the upper mirror was placed on top of them. The position of the lower mirror resting on the brass spacers was from here on monitored by three linear gage laser hologages placed on top of the upper mirror. The actual thickness of the brass spacers was measured prior to their usage using a micrometer screw gauge [7]. The results can be seen in table 3.13. The values stated are the mean value and the standard deviation of several measurements taken along the spacer. The mean as well as the standard deviation are subject to uncertainties due to the micrometer's measurement uncertainty. This uncertainties, obtained by Gaussian error propagation, are stated in table 3.13 as well. For the correction on the slit height at the center of the upper mirror the means of the two mean thicknesses and their standard deviations were calculated. The correction amounts to (38.7 ± 0.1) µm. The standard deviation is (1.4 ± 0.1) µm. To obtain one value for the uncertainty the standard deviation was taken. The shift on the slit height due to the spacers therefore is $z_{spacers} = 38.7$ µm and the uncertainty amounts to $\Delta z_{spacers} = 1.4$ µm.

Spacer	Mean Thickness	Standard Deviation
A	39.13 ± 0.15 µm	1.46 ± 0.15 µm
B	38.19 ± 0.13 µm	1.29 ± 0.13 µm

Table 3.13: Results of the measurements of the brass spacers thickness including their measurement uncertainty

For the installation process of the scatterers no spacers were needed since the roughness keeps the surfaces from attaching to each other. Therefore, the scatterers were simply placed on top of the lower mirror and the position was then, again, monitored by three linear gage hologages placed on top of the them. However, for the scatterer the roughness accounts for an uncertainty and a shift of the slit height, since when placing a scatterer on top of a flat mirror the contact points are the highest peaks of the scatterer's rough surface as illustrated in figure 3.45. The slit height is counted as the distance between the surface of the flat mirror and the mean line of the scatterer's rough surface. Therefore, when placing the scatterer on top of the lower mirror the slit is not equal zero but to the highest peak. The value of the highest peak therefore constitutes the shift on the slit height (z_{rough}) and furthermore the root mean squared value of the roughness (R_q) was added as an uncertainty of the slit height (Δz_{rough}). The values for the evaluation were taken from the stylus measurements as presented in subsection 3.2.4.

From here on the installation process continued similarly for both, an upper flat mirror or a scatterer. The upper mirror (/scatterer) was clamped to its mounting device and was ad-

---

[7]Coolant Proof Micrometer type 293-240; Mitutoyo Europe Gmbh, Borsigstrasse 8-10, 41469 Neuss, Germany

justed back into a parallel position above the lower mirror. This position constituted the zero position for the nanopositioning stage. From the values shown by the three linear gages the mean height ($z_{LG} \pm \Delta z_{LG}$) at the center of the upper mirror (/scatterer) above the starting position was calculated. Again, also the tilt was evaluated but is not stated here.

The installation process of the selector was different since no mounting device for the scatterer was used. The scatterer was placed on top of the lower mirror and the position was from here on monitored by the linear gage hologages. Subsequent, brass spacers were placed between the scatterer and the lower mirror by elevating the scatterer slightly. The slight height was then adjusted using the micrometer screws integrated into the selector casing's crossbeams. The final value for the slit height was calculated as the mean height shown by the linear gage hologages $z_{LG} \pm \Delta z_{LG}$ and also the shift and the uncertainty due to the scatterer's roughness was considered.
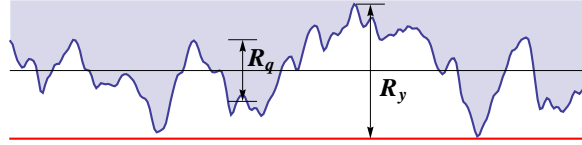

Figure 3.45: Illustration of a scatterer (rough surface; blue) placed on top of a flat mirror (red). The mean line as well as the roughness parameters R_q and R_y of the profile are shown. The picture is not drawn to scale.

Final Slit Height

The final values for the shift and the uncertainty of the slit height comprise as follows. For the overall shift on the slit height the respective single contributions are added: $z_{shift} = z_{spacers} + z_{LG} + z_{rough}$. For the uncertainty on the slit height the square root of the sum of the squared respective single contributions is taken:$\Delta z_{slit} = \sqrt{\Delta z_{spacers}^2 + \Delta z_{LG}^2 + \Delta z_{rough}^2 + \Delta z_{drift}^2 + \Delta z_{nano}^2}$. The resulting slit height for the selector is identical to the shift, since the slit height was unchanged during the measurements: $z_{selector} = z_{LG} + z_{rough}$. For the measurement part the slit height was changed using the nanopositioning stage and hence: $z_{mp} = z_{shift} + z_{nano}$ for the respective measurements.

The resulting values are stated in chapter 4 for the every measurement. The stated values for the slit height refer to the center of the mirrors. A possible tilt of the scatterers with respect to the lower mirrors was evaluated as well, but the values are not stated to keep this thesis within readable limits.

4 Measurements and Evaluation

In this chapter, the results of the performed measurements and their evaluation is presented. First, the velocity spectrum for v_x at the end of the vectorial velocity filter was recorded. Afterwards, a track detector measurement was performed to investigate the neutron distribution in front of the measurement part. Finally, transmission measurements in dependence of the measurement part's slit height, the quantum transport measurements, were performed.

The parameters regarding the setup are stated for every measurement performed. The stated values refer to the symmetry axis of the experimental setup. Inclination have also been evaluated but are not stated here. The values stated contain the height of the selector $h_{selector}$ and the height of the measurement part h_{mp} above the granite, the position of the upper and lower collimating plate above the granite h_{upper} and h_{lower}, the height of the step z_{step} and the width of the gap between the two setup parts x_{gap}. The slit height of the selector was constant during all measurements and amounted to $z_{selector} = (194.5 \pm 0.6)$ µm. z_{slit} denotes the slit height of the measurement part.

4.1 Velocity Spectrum

The first measurements after installing the selector concerned the velocity spectrum (v_x) of neutrons exiting the selector, representing the initial velocity spectrum for the transport measurements performed inside the measurement part. The neutrons' velocity at this position is controlled by the position of the collimating plates and the slit height of the selector as explained in section 2.2. However, for the evaluation, as performed here, the slit height was assumed to be infinitesimal small. For an infinitesimal small slit only neutrons with a vertical velocity component $v_z = 0$ at the slit entrance are allowed to traverse the filter. Neutrons with a higher vertical velocity are removed. With respect to the finite slit case, the calculation of horizontal velocities traversing the selector and the maximal and minimal horizontal velocities allowed, change to:

$$v_x = l_d \cdot \sqrt{\frac{g}{2\delta z}} \quad \Rightarrow \quad \begin{cases} v_{x_{min}} = l_d \cdot \sqrt{\frac{g}{2\delta z_{down}}} \\ v_{x_{max}} = l_d \cdot \sqrt{\frac{g}{2\delta z_{up}}} \end{cases} \tag{4.1}$$

The extracted velocity spectrum when neglecting the finite slit height might differ significantly from the real velocity spectrum. However, in this thesis the assumption is still made since the evaluation process for an infinitesimal small slit is well known and has been used previously by the qbounce collaboration). A more detailed evaluation process, incorporating the finite slit height is in development and will be published in [Cro15]. The evaluation process as presented here follows [Jen11, p43 ff].
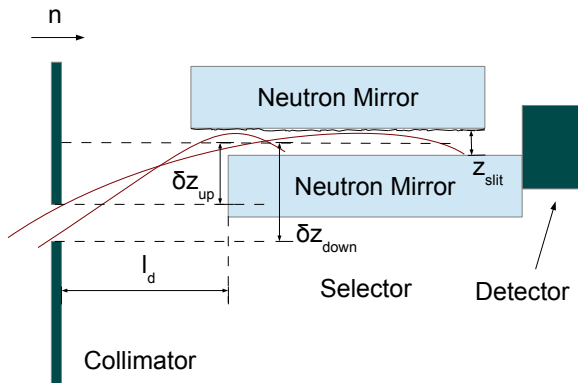
Figure 4.1: Schematic view of the experimental setup while recording the velocity spectrum.

Table 4.1: Setup parameters while recording of the velocity spectrum.

Parameter	Value
$h_{selector}$	109.19 ± 0.01mm
$z_{selector}$	194.5 ± 0.6 µm

To record the velocity spectrum, transmission measurements in dependence of the position of the collimating plates were performed. To do so, the neutron counter was placed directly behind the selector (see figure 4.1 for a schematic view and table 4.1 for the setup's parameters). First, the upper collimating plate had to be adjusted into a position where it influences neutrons entering the filter. This position was found by varying its height until a drop in transmission was recorded. The lower collimating plate was, in the meantime, fixed at a position of (87.11 ± 0.07) mm above the granite. These measurements are shown in figure 4.2a. A clear drop in transmission between the measurement ID 272 with a position of (107.17 ± 0.7) mm and ID 273 with position (106.20 ± 0.06) mm, can be seen. The upper collimating plate was then fixed at a position of (106.69 ± 0.08) mm, allowing neutrons with a maximum velocity in x direction of (6.85 ± 0.11) m/s (according to equation 4.1) into the selector. To investigate the velocity spectrum, now transmission measurements in dependence of the position of the lower collimating plate were performed. The measurements can be seen in figure 4.2b. The transmission drops with increasing height of the lower collimating plate since the opening between the two collimating plates becomes smaller.

For the extraction of the velocity spectrum $\partial f / \partial v_x$ one has to consider, that for the transmission T holds:

$$T(\delta z_{down}) = \int_{\delta z_{down}}^{\delta z_{up}} dh \frac{\partial \tilde{f}}{\partial h} = \int_{v_{min}}^{v_{max}} dv_x \frac{\partial f}{\partial v_x} \tag{4.2}$$

where the relationship between height and velocity is:

$$h = \frac{g}{2} \left(\frac{\Delta x}{v_x} \right)^2 \tag{4.3}$$

For the velocity spectrum the ansatz:

$$\frac{\partial f}{\partial v_x} = \begin{cases} e^{-(v_x - v_0)^b} (v_x - v_0)^c & z_B \geq 0 \\ 0 & z_B < 0 \end{cases} \tag{4.4}$$

as found in [Jen11, p44], is taken. Here $v_0 = 3.24$ m/s is the minimal velocity obtained from the Fermi potential of the aluminum foil the UCNs have to pass through when entering the
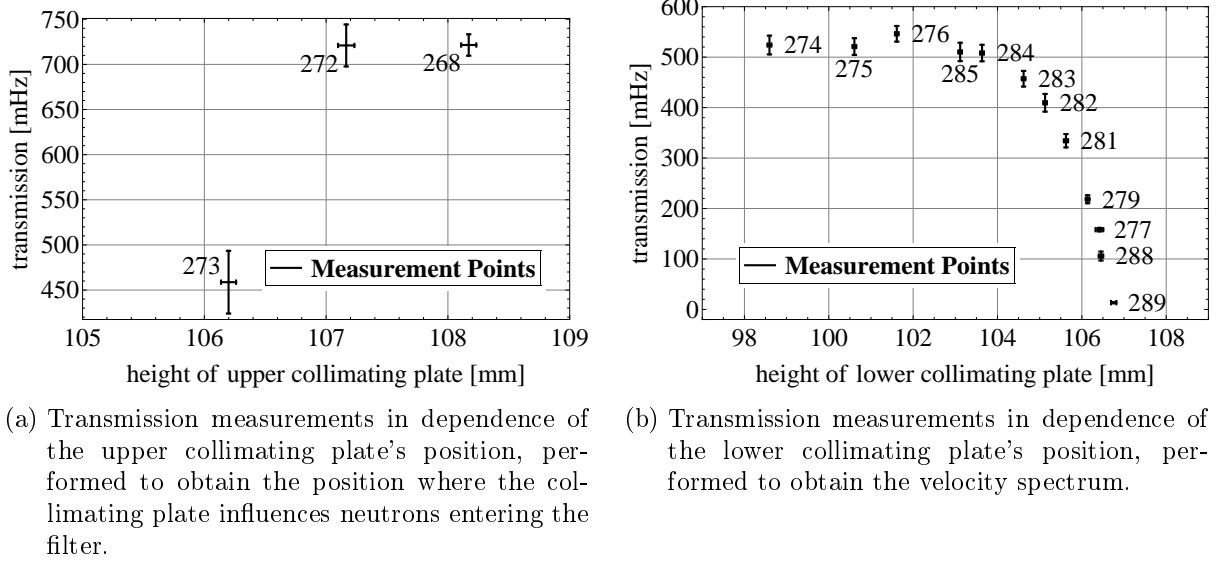
(a) Transmission measurements in dependence of the upper collimating plate's position, performed to obtain the position where the collimating plate influences neutrons entering the filter.

(b) Transmission measurements in dependence of the lower collimating plate's position, performed to obtain the velocity spectrum.

Figure 4.2: Transmission measurements in dependence of the collimating plates' position, performed to obtain the velocity spectrum.

vacuum chamber and b and c are free fit parameters. With this ansatz, after integration, one obtains a fit function of the form:

$$F(z_B) = N \cdot \Gamma \left(\frac{c+1}{b}, (v_x(z_B) - v_0)^b \right) + N_0 \qquad (4.5)$$

Here Γ denotes the incomplete Gamma function with additional parameters. N represents the global norm and N_0 the detector background.

With the fit function a χ^2-fit to the data was performed. For the fit the measurements ID 277 and 289 were excluded since they have a much smaller measurement uncertainty compared to the other measurements. This led to incorrect fitting results since the fit parameters are determined mainly by these measurements. Accordingly, no reasonable fit could be obtained including this two measurements. This is also an indication, that the assumption of an infinitely small slit does not hold. Furthermore the fit parameter N_0 was fixed at 0.641 mHz, the evaluated detector's background noise.

The obtained function after fitting is plotted in figure 4.3a, where also the parameters of the best fit are stated. The fit shows a χ^2 of 12.49 with 7 degrees of freedom. The obtained velocity spectrum and the part extracted for the track detector measurements is shown in figure 4.3b. Neglecting the finite slit height the extracted spectrum for the track detector measurements was limited by $v_{x_{min}} = (4.02 \pm 0.01)$ m/s and $v_{x_{max}} = (5.85 \pm 0.06)$ m/s (equation 4.1). Incorporating the finite slit height one obtains $v_{x_{min}} = (4.74 \pm 0.02)$ m/s and $v_{x_{max}} = (7.64 \pm 0.05)$ m/s (equation 2.10). The stated maximal and minimal velocities in the following sections are calculated with respect to the finite slit height.
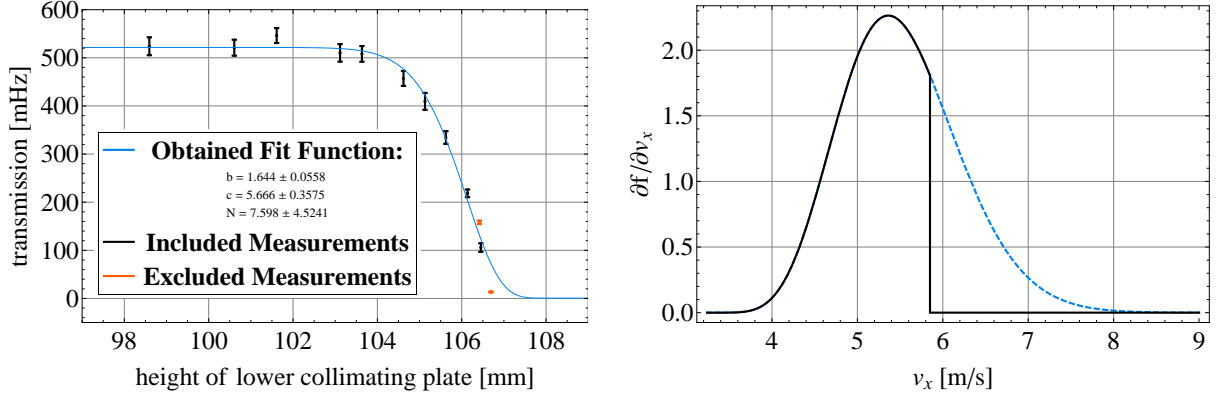
(a) Measurement data recorded to obtain the velocity spectrum for v_x and fitted function $F(z_B)$ from equation 4.5. N_0 was fixed to 0.641 mHz for the fit. The two measurements depicted in orange have been excluded from the fit data due to their comparatively small measurement uncertainty.

(b) Velocity spectrum $\partial f/\partial v_x$ (dashed line) obtained from the fit function $F(z_B)$ shown to the left. The solid black curve represents the part of the spectrum used during the track detector measurements (using the infinitely small slit assumption).

Figure 4.3: Measurement data with fit (a) and obtained velocity spectrum (b).

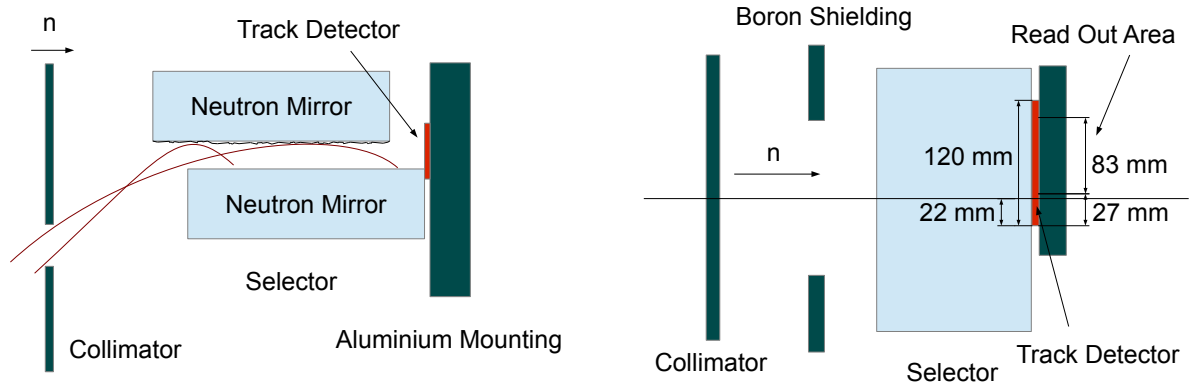## 4.2 Track Detector Measurement

To further investigate the initial phase space for the transport measurements, prepared by the vectorial velocity filter, spatially resolved track detector measurements were performed to record the neutrons' distribution at the selector's end. The track detector used consists of a coated piece of organic substrate as described in subsection 3.1.2. The detector has a length of 120 mm with an active area of 11.2 mm. The detector was installed at the back of the selector, a little left to the center, to record the neutron distribution entering the measurement part. A schematic view of the setup during the track detector measurement can be seen in figure 4.5. The important parameters are shown in table 4.2. The detector was exposed to neutrons for a time of 8 hours and 48 minutes.

4.2.1 Chemical Follow-Up Treatment and Read-Out Process

After exposure, the track detector was treated chemically to allow read-out using an optical microscope. To do so, the ^{10}B-coating was removed using a solution of sulfuric acid an hydrogen peroxide in an ultrasonic bath. Subsequently, the detector was then etched for 5 hours. The

Parameter	Value
$h_{selector}$	109.19 ± 0.01mm
$z_{selector}$	194.5 ± 0.6µm
h_{upper}	105.83 ± 0.07mm
h_{lower}	101.84 ± 0.05mm

Table 4.2: Setup parameters during the track detector measurement.

n →

Track Detector

Neutron Mirror

Neutron Mirror

Selector

Collimator

Aluminium Mounting

Boron Shielding

Read Out Area

n →

120 mm

83 mm

22 mm

27 mm

Collimator

Selector

Track Detector

(a) Side view of the experimental setup during the track detector measurement.

(b) Top view of the experimental setup during the track detector measurement.

Figure 4.4: Schematic view of the setup during the track detector measurement.

etching process magnifies the imperfection in the crystal structure, impinged by the reaction products due to neutron exposure and the track detector can be read out using an optical microscope.

4.2.2 Results

The track detector was read-out using an Olympus optical microscope[1]. The microscope is mounted on a positioning table for the read out. The positioning table allows for a maximal scanning area of around 8.3 cm. The position of the read out area is indicated in figure 4.5. The resulting data were evaluated as described in [Jen11, p45 ff]. The resulting data from the read-out process can be seen in figure 4.5a. Here every point corresponds to an impingement on the track detector. In figure 4.5b the vertical dependence of the data with a bin size of 10 µm is shown. Since the selector is not ideal in the sense, that it does not filter out all neutrons with $v_z > \sqrt{2m_n z_{selector}}$, neutrons above the slit height have also been recorded. These tracks are indicated by the highlighted area in figure 4.5b. (4.45 ± 0.73) % of all neutrons were recorded with $z > z_{selector}$. This results are also published in [Chi+14] were further interpretation is given.

(a) Track detector data; every point represents an impingement and hence a detected neutron.

(b) Vertical dependence of the data with a bin size of 10µm. The red line indicated the background noise.
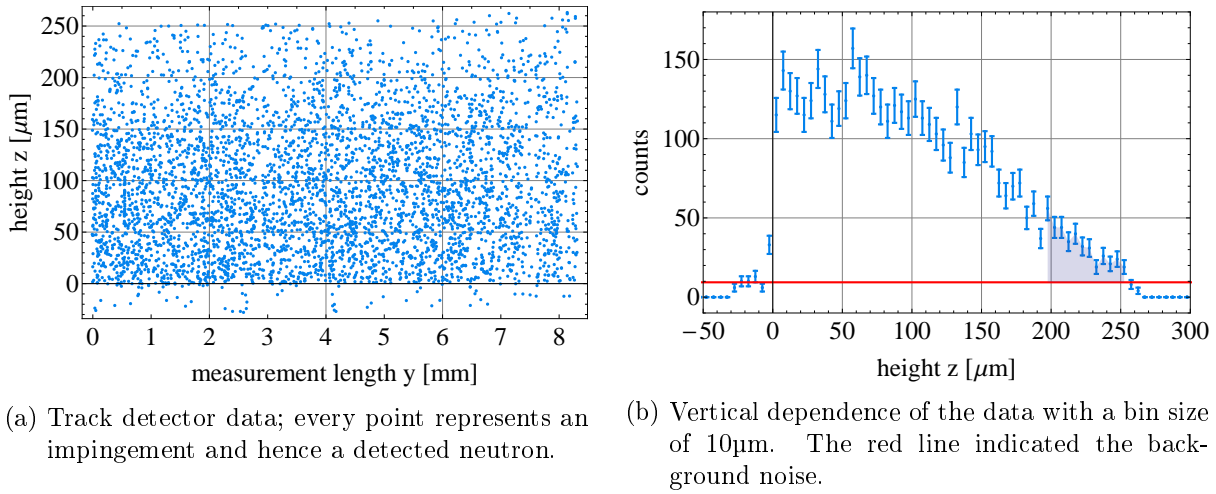
Figure 4.5: Visualization of the track detector data.

4.3 Quantum Transport Measurements

Below, the results of the performed transport measurements are presented. For every measurement series using different mirrors and/or scatterers within the measurement part, the theoretical expectation function for the classical regime has been fitted to the data. The results in the quantum mechanical regime are stated, but are only evaluated for the expectation regarding their material dependence (see subsection 2.3). A detailed interpretation of the results in the quantum mechanical regime will be developed by the theory group of S. Rotter.

For the quantum transport measurements the position of the collimating plates was changed to the values stated in table 4.3 to further increase transmission. This position was fixed for all quantum transport measurements and hence neutrons with a maximal absolute velocity of (9.13 ± 0.17) m/s were allowed to enter the measurement part. For every measurement series val-

Parameter	Value
h_{upper}	106.42 ± 0.06 mm
h_{lower}	101.84 ± 0.05 mm

Table 4.3: Position of the collimating plates for all qTransport measurements

ues for the height of the selector's and the measurement part's lower mirrors above the granite are stated. Furthermore values for the step and the gap between the selector and the measurement part are given. The results of the transmission measurements are shown graphically. The uncertainties plotted refer to the uncertainty of the measurement part's slit height z_{slit} at the center of the upper mirror (/scatterer) and of the recorded neutron rate.

4.3.1 Ni-mirror/Ni-mirror

The final parameters for the measurements using a mirror-mirror system with Ni-58 coated mirrors can be seen in table 4.4. For this measurement series the value for the gap has been estimated to be smaller 150 µm because the standard procedure has been performed, however, no values have been recorded within the laboratory notebook. The height of the selector has not been measured directly, but the values stated are deduced from previous measurements and the change in height recorded by the nanopositioning stage.

Parameter	Value
$h_{selector}$	109.19 ± 0.01 mm
h_{mp}	109.20 ± 0.01 mm
z_{step}	0.35 ± 0.08 µm
x_{gap}	50 µm $\leq x_{gap} \leq 150$ µm

Table 4.4: Final parameters for the measurement series Ni-mirror/Ni-mirror.

The results are shown below in figure 4.6. A function according to the expectations for the mirror-mirror system (see subsection 2.3, equation 2.12) was fitted to the data. Only an overall normalisation constant N was added as sole fit parameter, also containing the prefactors from equation 2.12. The filter's slit height is now denominated $z_{selector}$ instead of h:

$$T(z_{slit}) = N \cdot \left(z_{selector}^{3/2} - \left(z_{selector} - z_{slit} \right)^{3/2} \right) \tag{4.6}$$

The obtained function after fitting is plotted in figure 4.6, where also the parameters for the best fit are stated. The fit shows a χ^2 of 119.18 with 14 degrees of freedom. The badness of the fit can be explained since the theory function does not consider scattering states and the increasing transmission above the selector's slit height, expected due to the selector's mirror shift (see subsection 2.3), as clearly visible in figure 4.6. To better describe the data an additional linear function with it's slope as second fit parameter ($N1$) was added to the theory function:

$$T(z_{slit}) = N \cdot \left(z_{selector}^{3/2} - \left(z_{selector} - z_{slit} \right)^{3/2} \right) + N1 \cdot z_{slit} \tag{4.7}$$

The additional linear increase with slit height can be physically explained as accounting for the scattering states. Since the mirror-mirror system only removes neutrons with an absolute velocity larger $v_{cr} = 8$ m/s neutrons on scattering with an absolute velocity smaller v_{cr} will traverse the measurement part, accounting for an additional increase in transmission. The fit including the linear function is in much better agreement with the data (see figure 4.7) and shows a χ^2 of 41.78 with 13 degrees of freedom.
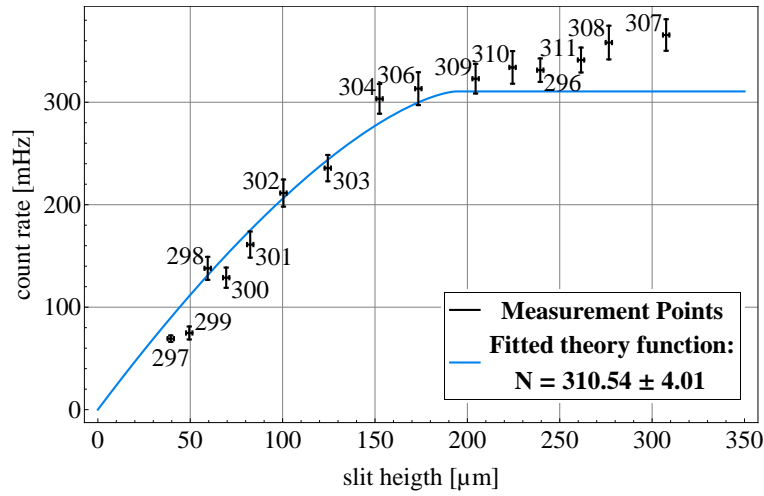
Figure 4.6: Measurement results for the classical regime and fitted theory function ignoring scattering states (equation 4.6) of the measurement series Ni-mirror/Ni-mirror. The numbers reference to the measurement IDs.
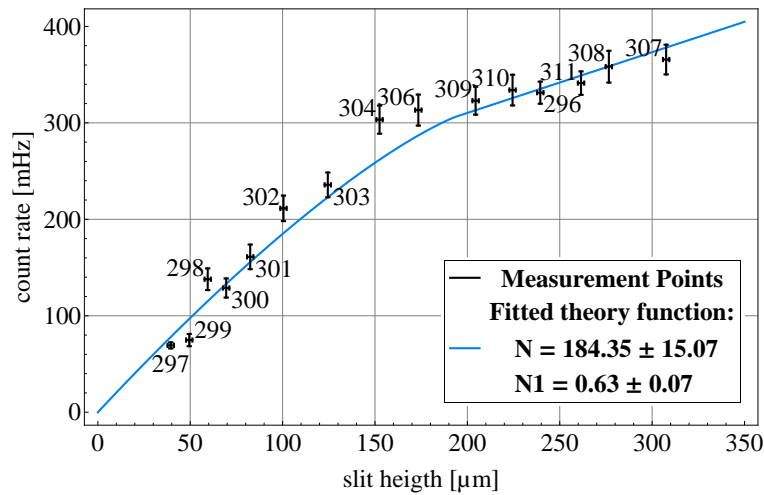

Figure 4.7: Measurement results for the classical regime and fitted theory function including scattering states (equation 4.7) of the measurement series Ni-mirror/Ni-mirror. The numbers reference to the measurement IDs.

4.3.2 Ni-mirror/Ni-scatterer

The final parameters for the measurement series can be seen in table 4.5. The value for the gap has been estimated to be smaller 150 µm because the standard procedure has been performed, however, no values have been recorded within the laboratory notebook. The height of the selector has not been measured directly, but the values stated are deduced from previous measurements and the change in height.

Parameter	Value
$h_{selector}$	109.19 ± 0.01 mm
h_{mp}	109.20 ± 0.01 mm
z_{step}	0.07 ± 0.13 µm
x_{gap}	50 µm $\leq x_{gap} \leq 150$ µm

Table 4.5: Final parameters for the measurement series Ni-mirror/Ni-scatterer.

The results are shown in figure 4.8 and 4.10. Again, the theory function as presented in subsection 2.3 (equation 2.13) for the transport measurements using an ARMS was fitted to the data. An overall normalisation constant N was also added as fit parameter:

$$T(z_{slit}) = N \cdot z_{slit}^{3/2} \tag{4.8}$$

Since the theory function ignores the increase of transmission above the selectors slit height, again, the fit is not in good agreement with the results showing a χ^2 of 30.41 with 11 degrees of freedom. A better fit can be obtained by again adding a linear function to the theory function. However, in case of an ARMS the probability for scattering states to reach the detector is much lower compared to the MMS since filtering due to the interaction with the surface roughness also occurs inside the measurement part. The linear function is therefore only added above the selector's slit height:

$$T(z_{slit}) = \begin{cases} N \cdot z_{slit}^{3/2} & z_{slit} \leq z_{selector} \\ N + N1 \cdot (z_{slit} - z_{selector}) & z_{slit} > z_{selector} \end{cases} \tag{4.9}$$

The fit incorporating the transmission increase above the selectors slit height shows a better agreement with the data, having a χ^2 of 18.83 with 10 degrees of freedom. The fit is shown in figure 4.9.
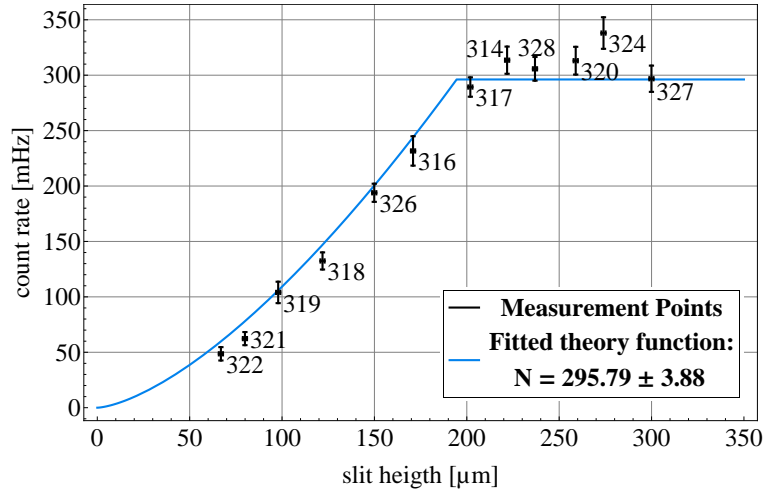

Figure 4.8: Measurement results for the classical regime and fitted theory function ignoring the transmission increase above the selector's slit height (equation 4.8) of the measurement series Ni-mirror/Ni-scatterer. The numbers reference to the measurement IDs.
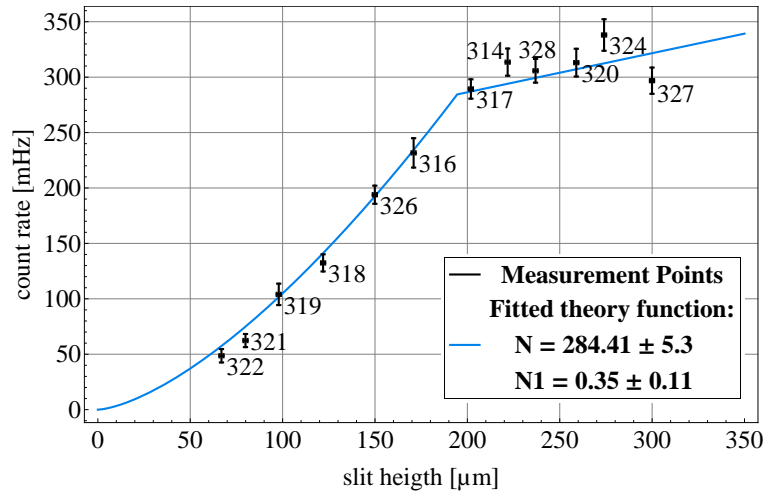
Figure 4.9: Measurement results for the classical regime and fitted theory function incorporating the transmission increase above the selector's slit height (equation 4.9) of the measurement series Ni-mirror/Ni-scatterer. The numbers reference to the measurement IDs.
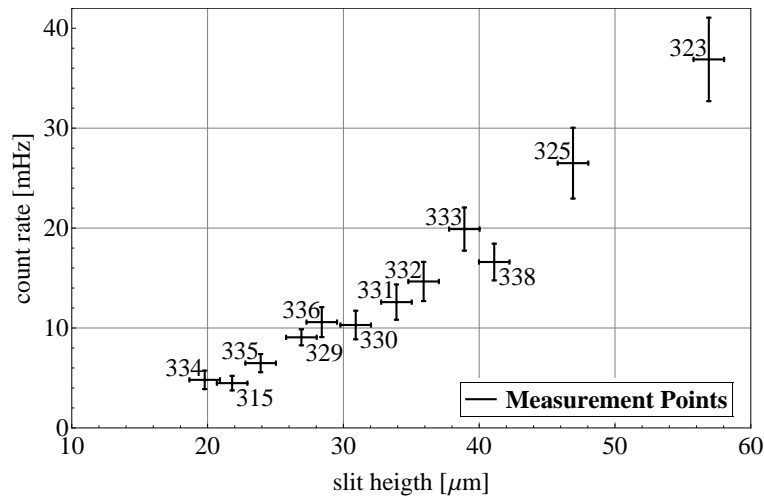

Figure 4.10: Measurement results for the quantum mechanical of the measurement series Ni-mirror/Ni-scatterer. The numbers reference to the measurement IDs.

4.3.3 Glass-mirror/Ni-scatterer

The final parameters for the Glass-mirror/Ni-scatterer system can be seen in table 4.6. Also for this measurement series, equation 4.9, including the transmission increase above the selector's slit height was fitted to the data in the classical regime. The results and the obtained function are plotted in figure 4.11. The fit value for the best fit parameter is also stated there. The fit is in good agreement with the data, showing a χ^2 of 1.47 with 5 degrees of freedom. The additional transmission increase is clearly visible again. The results for the quantum mechanical regime are shown in figure 4.12.

Parameter	Value
$h_{selector}$	109.19 ± 0.01 mm
h_{mp}	109.19 ± 0.01 mm
z_{step}	0.14 ± 0.07 µm
x_{gap}	30 µm $\leq x_{gap} \leq 75$ µm

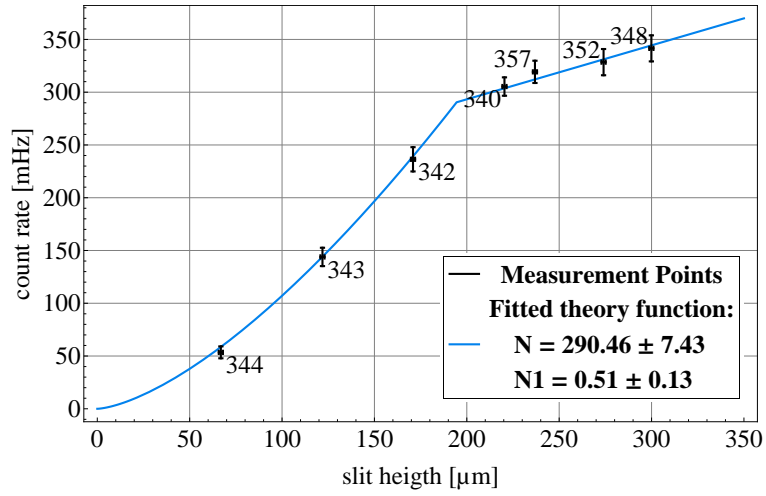Table 4.6: Final parameters for the measurement series Glass-mirror/Ni-mirror.

Figure 4.11: Measurement results for the classical regime and fitted theory function of the measurement series Glass-mirror/Ni-scatterer. The numbers reference to the measurement IDs.
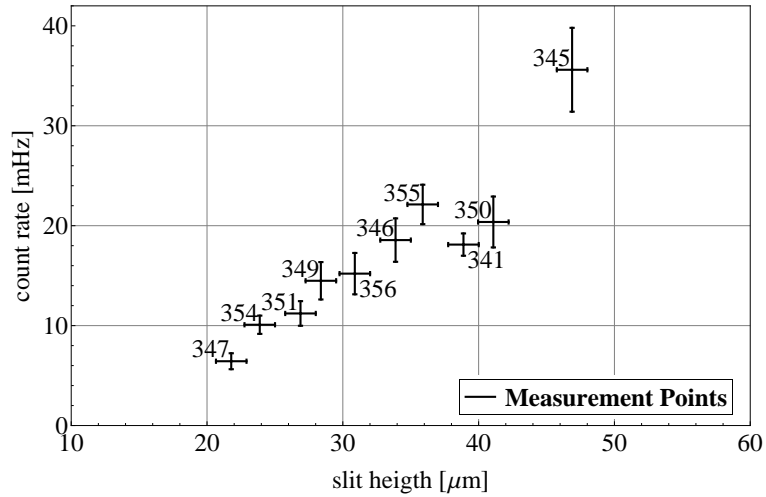

Figure 4.12: Measurement results for the quantum mechanical of the measurement series Glass-mirror/Ni-scatterer. The numbers reference to the measurement IDs.

4.3.4 Glass-mirror/Glass-scatterer

The final parameters for the last measurement series (Glass-mirror/Glass-scatterer) can be seen in table 4.7. The fit for the classical regime (equation 4.9) is in good agreement with the data having χ^2 of 8.35 with 6 degrees of freedom. The results for the classical regime, including the obtained function and the best fit parameter are shown below in figure 4.13. The results for the quantum mechanical regime are plotted in figure 4.14.

Parameter	Value
$h_{selector}$	109.19 ± 0.01 mm
h_{mp}	109.19 ± 0.01 mm
z_{step}	-0.34 ± 0.06 µm
x_{gap}	$75\text{µm} \leq x_{gap} \leq 125$ µm

Table 4.7: Final parameters for the measurement series Glass-mirror/Glass-scatterer.
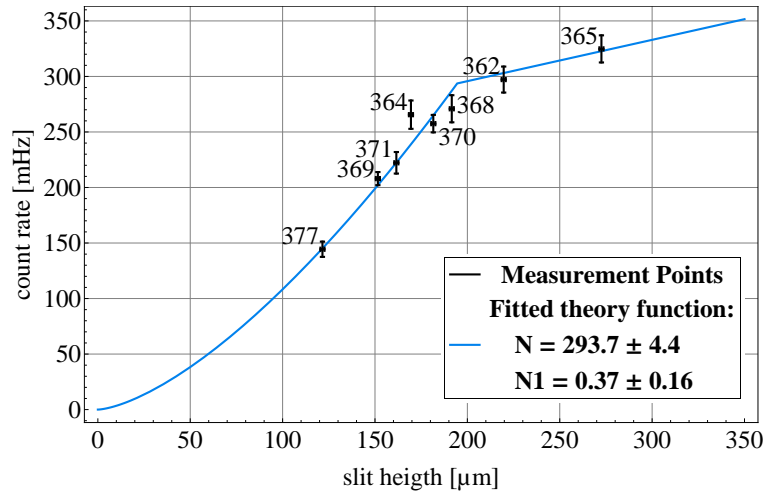

Figure 4.13: Measurement results for the classical regime and fitted theory function of the measurement series Glass-mirror/Glass-scatterer. The numbers reference to the measurement IDs.
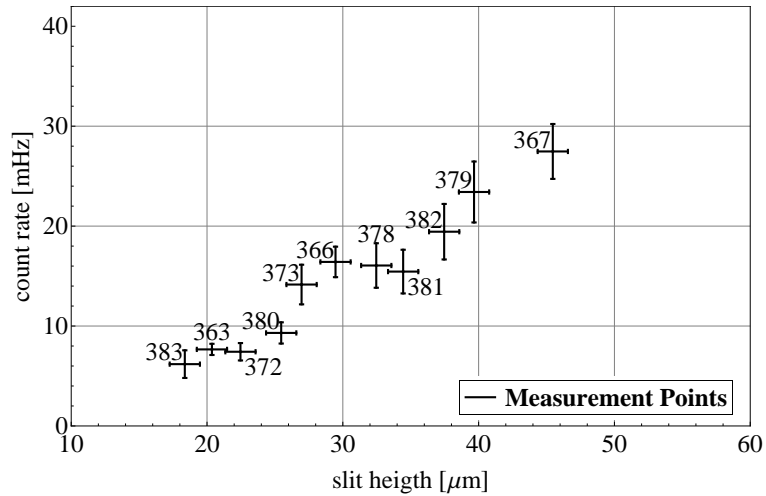
Figure 4.14: Measurement results for the quantum mechanical of the measurement series Glass-mirror/Glass-scatterer. The numbers reference to the measurement IDs.

4.3.5 Comparison of the Results

For the measurements using differently coated mirrors and scatterers, different transmissions were expected (see subsection 2.3). For the Ni-mirror/Ni-scatterer system transmission was expected to be highest due to the large Fermi potential of Ni-58. For the Glas-mirror/Ni-scatterer system transmission was thought to be lower, and for the Glas-mirror/Glass-scatterer system transmission was expected to be lowest.

Comparing the results in the classical regime, transmission does not behave as expected. This is visible when comparing the normalisation constants N for the fit functions. In contrast to the expectations, the Ni-mirror/Ni-scatterer system shows the lowest normalisation constant with $N = 284.41 \pm 5.3$. The Glass-mirror/Ni-scatterer system shows the highest constant of $N = 293.7 \pm 4.4$, and the Glass-mirror/Glass-scatterer system has $N = 290.46 \pm 7.43$, slightly above the Ni-mirror/Ni-scatterer system.

In the quantum mechanical regime transmission also behaves in contrast to the expectations. A plot comparing the results in the quantum mechanical regime is shown in figure 4.15. It is clearly visibly, that the measurements performed with the Ni-mirror/Ni-scatterer system show the lowest transmission, in contrast to the theoretical expectations. For the two other systems it is unclear which shows the higher overall transmission.

An explanation of the unexpected transmission behavior is not known up to now but will be discussed by the theorists.
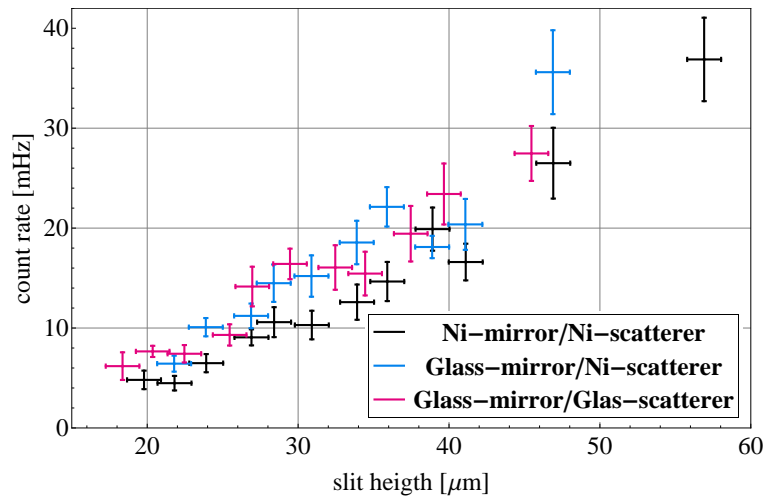
Figure 4.15: Comparison of measurement results for the quantum mechanical regime, obtained by using differently coated mirrors and scatterers inside the measurement part of the experimental setup.

5 Conclusion and Prospect

The intended quantum transport measurements of UCNs traversing a system with one-sided surface disorder have successfully been performed for several systems offering different transport properties. The redesign of the experimental setup enabled the recording of a comparatively large number of measurement points within the same time frame. The results for every system follow, in the classical regime, the behavior of the theory function. However, comparing the results for different systems, the expected transmission dependence on the usage of differently coated mirrors and scatterers has not been verified. Reasons for this unexpected discrepancy, as well as the evaluation of the results for the quantum mechanical regime are to be done by the theory group around S. Rotter.

In addition to performing the quantum transport measurements, the spatial distribution of neutrons entering the measurement part was recorded using a track detector. These measurements allow for a better interpretation of the transport measurements' results. The evaluated results show a fraction of (4.45 ± 0.73) % of neutrons above the vectorial velocity filter's slit height. These results are also published in [Chi+14], where furthermore a comparison with simulation results is given.

For the recorded measurements it was achieved to keep systematic effects within good range. For the transport measurements, the uncertainty of the slit height inside the measurement parts was below 1.72 µm for all measurements, the gap between the two parts of the experimental setup was evaluated to be smaller 150 µm and the step between the parts was $-0.34 \leq z_{step} \leq 0.35$ µm.

To further reduce the measurement uncertainties, several proposals for the setup can be made: First of all, to reduce the uncertainty on the measurement parts slit height a position control for the coarse adjustment device could be used. The drift of the device could then be readjusted by the nanopositioning stage, reducing the error on the slit height tremendously. Furthermore, the step between the setup's parts could be monitored during measurement. For this, a system already used within the qBounce collaboration could be used. The system consists of capacitive sensors mounted on a movable construction above the experimental setup. In order to use the system, the neutron mirrors used as lower mirrors have a larger width than their respective upper mirrors/scatterers. The capacitive sensors are then moved back and forth over the step and the mirrors are aligned accordingly by a nanopositioning stage.

Finally, in this thesis measurements of the scatterers' rough surfaces were presented and evaluated. The detailed evaluation was performed to enable a better interpretation of the experimental results. However, the surface measurements were shown to be insufficient in statistics by means of surface area measured. Large scale AFM or SEM measurements are therefore proposed to increase knowledge about the surface disorder. AFM measurements

would have the additional advantage of being able to measure the coated as well as the uncoated measurements and therefore to obtain information about the changes introduced by the coating process.

Bibliography

[BH92]   Horst Bodschwinna and Walter Hillmann. *Oberflächenmeßtechnik mit Tastschnittgeräten in der industriellen Paxis*. Beuth-Kommentare. Berlin: Beuth, 1992.

[Chi+14]   L. A. Chizhova et al. "Vectorial velocity filter for ultracold neutrons based on a surface-disordered mirror system". In: *Phys. Rev. E* 89 (3 2014), p. 032907.

[Cro15]   Gunther Cronenberg. "Using frequency measurements to test Newton's Gravity Law". PhD thesis. Vienna University of Technology, 2015.

[Dav10]   J.P. Davim. *Surface Integrity in Machining*. SpringerLink : Bücher. London: Springer, 2010. ISBN: 9781848828742.

[Dop+14]   J Doppler et al. "Reflection resonances in surface-disordered waveguides: strong higher-order effects of the disorder". In: *New Journal of Physics* 16.5 (May 2014), p. 053026.

[Fei+06]   J. Feist et al. "Nanowires with Surface Disorder: Giant Localization Lengths and Quantum-to-Classical Crossover". In: *Physical Review Letters* 97.11 (Sept. 2006).

[Fei+09]   J. Feist et al. "Nanowires with surface disorder: Giant localization length and dynamical tunneling in the presence of directed chaos". In: *Physical Review B* 80.24 (Dec. 2009).

[GP79]   R. Golub and J. M. Pendlebury. "Ultra-cold neutrons". In: *Reports on Progress in Physics* 42.3 (1979), p. 439.

[HS02]   Rüdiger A. Heinzel G. and R. Schilling. *Spectrum and spectral density esimationby the Discete Fourier transform (DFT), including a comprehensice list of window functions and some new flat-top windows*. Feb. 15, 2002. URL: `http://holometer.fnal.gov/GH_FFT.pdf` (visited on 05/22/2014).

[Jen+11]   Tobias Jenke et al. "Realization of a gravity-resonance-spectroscopy technique". In: *Nature Physics* 7.6 (June 2011), pp. 468–472.

[Jen+13]   Tobias Jenke et al. "Ultracold neutron detectors based on 10B converters used in the qBounce experiments". In: *Nuclear Instruments and Methods in Physics Research Section A: Accelerators, Spectrometers, Detectors and Associated Equipment* 732 (Dec. 2013), pp. 1–8.

[Jen11]   Tobias Jenke. "qBounce - vom Quantum Bounder zur Gravitationresonanzspektroskopie". PhD thesis. Vienna University of Technology, 2011.

[Kra06]   Claude Kranz. "Quantum States of Neutrons in the Gravitational Field". Diploma thesis. University of Heidelberg, 2006.

[LC12]   Dong-Hyeok Lee and Nahm-Gyoo Cho. "Assessment of surface profile data acquired by a stylus profilometer". In: *Measurement Science and Technology* 23.10 (Oct. 1, 2012), p. 105601.

[LF78]   V. I. Luschikov and A. I. Frank. "Quantum effects ocurring when ultracold neutrons are stored on a plane". In: *Joint Institute for Nuclear Research* 28.9 (1978), p. 559.

[Nes+00]   V.V Nesvizhevsky et al. "Search for quantum states of the neutron in a gravitational field: gravitational levels". In: *Nuclear Instruments and Methods in Physics Research Section A: Accelerators, Spectrometers, Detectors and Associated Equipment* 440.3 (Feb. 2000), pp. 754–759.

[Nes+02]   V. V. Nesvizhevsky et al. "Quantum states of neutrons in the Earth's gravitational field". In: *Nature* 415.6869 (2002), pp. 297–299.

[Nes+03]   V. V. Nesvizhevsky et al. "Measurement of quantum states of neutrons in the Earth's gravitational field". In: *Physical Review D* 67.10 (May 13, 2003).

[Nes+05]   V. V. Nesvizhevsky et al. "Study of the neutron quantum states in the gravity field". In: *The European Physical Journal C* 40.4 (2005), pp. 479–491.

[PB95]   Chin Y. Poon and Bharat Bhushan. "Comparison of surface roughness measurements by stylus profiler, AFM and non-contact optical profiler". In: *Wear* 190.1 (Nov. 1995), pp. 76–88.

[Pf2]   *Description PF2*. Sept. 28, 2012. URL: http : / / www . ill . eu / instruments - support / instruments - groups / instruments / pf2 / description / instrument - layout/ (visited on 08/20/2015).

[RSS09]   Rafael Reiter, Bernhard Schlederer, and David Seppi. "Quantenmechanisches Verhalten eines ultrakalten Neutrons im Gravitationsfeld". Project thesis. Vienna University of Technology, 2009.

[Rad70]   V. Radhakrishnan. "Effect of stylus radius on the roughness values measured with tracing stylus instruments". In: *Wear* 16.5 (Nov. 1970), pp. 325–335.

[Sau11]   Heiko Saul. "Weiterentwicklung des Detektor- und Auslesekonzepts für das Gravitationsexperiment qBounce". Diploma thesis. Vienna University of Technology, 2011.

[Tha13]   Martin Thalhammer. "Optimierung der Detektorsignalverarbeitung des Gravitationsexperiments qBounce". Master thesis. Vienna University of Technology, 2013.

[Tho99]   Tom R. Thomas. *Rough surfaces*. 2nd ed. London: Imperial College Pr., 1999. ISBN: 1-86094-100-1.

[Wes+07]   A. Westphal et al. "A quantum mechanical description of the experiment on the observation of gravitationally bound states". In: *The European Physical Journal C* 51.2 (June 12, 2007), pp. 367–375.

[Wes02]   Alexander Westphal. "Quantum Mechanics and Gravitation". Diploma thesis. University of Heidelberg, 2002.

[Whi10]   D.J. Whitehouse. *Handbook of Surface and Nanometrology, Second Edition*. Taylor & Francis, 2010. ISBN: 9781420082029.

Acknowledgements